NANYANG
TECHNOLOGICAL
UNIVERSITY

# DUAL PHASE $TiO_2$ NANOTUBES FOR HIGH POWER ELECTROCHEMICAL ENERGY STORAGE DEVICES

**DENG JIYANG**

**SCHOOL OF MATERIALS SCIENCE AND ENGINEERING**

**2016**

# DUAL PHASE $TiO_2$ NANOTUBES FOR HIGH POWER ELECTROCHEMICAL ENERGY STORAGE DEVICES

**DENG JIYANG**

SCHOOL OF MATERIALS SCIENCE AND
ENGINEERING

A thesis submitted to the Nanyang Technological University
in partial fulfilment of the requirement for the degree of
Doctor of Philosophy

**2016**

# Abstract

The development of ultrafast charging electrochemical energy storage (EES) devices with long cycle life is of great importance to the advancement of modern society with sustainable energy generation and consumption. Lithium-ion based EES devices offer high power, high energy and exceptional lifetime and are consistently pursued for such applications. In particular, $TiO_2$ (B) material is promising anode candidate owing to its fast lithium diffusion kinetics and open channel structure. However, the high rate performance of $TiO_2$ (B) is hindered by its poor electrical conductivity originated from large band gap (> 3.0 eV), therefore a large amount of conductive additives (> 15 wt%) are required to unleash the high power capabilities, which decreases the overall energy of the electrode since these additives are electro inactive within the operation window (1-3 V) of $TiO_2$ (B). To address such issues, this thesis aims to improve the high rate performances of $TiO_2$ (B) electrode while maximizing the total contents of active materials through integration of anatase phase. The ultimate scope is to develop fast charging $TiO_2$ electrodes with maximum loading amount of active materials for high power and long life EES devices.

To achieve such goal, the properties of $TiO_2$ materials are investigated first in half cells with lithium metal as counter electrode. Applying the additive-free all $TiO_2$ nanotube electrodes as platform, a systematic investigation of the electrodes conduction behavior via *in situ* electrochemical impedance study (EIS) indicates that much higher lithiation-induced conductivity is achieved in dual phase $TiO_2$ nanotubes than pure phase $TiO_2$ (B) at early stage of reaction, owing to the high conductivity of lithiated anatase. The resultant dual phase $TiO_2$ nanotubes feature superior rate performances: a specific capacity of 112.1 mAh $g^{-1}$ can be delivered at 24 A $g^{-1}$ (~72 C), and higher capacity of 131.1 mAh $g^{-1}$ can be achieved after 10,000 cycles at 30 C. Furthermore, even mechanical mixture of anatase particles to $TiO_2$ (B) nanotubes exhibits much higher rate performances at 24 A $g^{-1}$ (91.2 mAh $g^{-1}$) than pure phase $TiO_2$ (B) nanotubes (13.7 mAh $g^{-1}$). Followed by the discovery of high lithiation-induced conductivity in dual phase $TiO_2$ materials, a pre-lithiation process is carried out to improve the electrical conductivity and first cycle Columbic efficiency of the pristine $TiO_2$ materials for applications in high power lithium-ion hybrid capacitor (LIC). The LIC cells with pre-lithiated $TiO_2$ anode could achieve high energy density of 50.77 Wh $kg^{-1}$ and high power density of 8.98 kW $kg^{-1}$ at 20.7 Wh $kg^{-1}$, compared to only 10.9 Wh $kg^{-1}$ delivered by pristine $TiO_2$ electrode at power density of 4550 W $kg^{-1}$. Furthermore, the cycling stability of the pre-lithiated $TiO_2$ materials is also improved with 73% capacity retention after 10,000 cycles. Finally, a water soluble sericin binder is developed for the first time to assist in formation of stable passivation layer in high voltage $LiNi_{0.5}Mn_{1.5}O_4$ cathode to fabricate high energy and high power battery cells with $TiO_2$ anode. The highest energy density of the full cell formulated with sericin binder can reach 687.6 Wh $kg^{-1}$ (based on $TiO_2$ mass). At higher power of 18.26 kW $kg^{-1}$, the energy density can still reach 233.4 Wh $kg^{-1}$, much higher than that of the PVDF binder (89.7 Wh $kg^{-1}$). Furthermore, the full cell could be cycled at 10 C for 1,000 cycles with 80% capacity retention, further indicating the long-term stability of $TiO_2$ and the sericin binder.

In conclusion, this thesis unravels the importance of dual phase $TiO_2$ electrode for ultrafast charging EES devices with ultralong cycle life. The lithiation-induced conductivity plays important roles in the utilization of $TiO_2$-based electrode materials with fast charging capabilities. These findings provide guidance towards commercial adoption of $TiO_2$-based electrode, in fact, large scale prismatic and cylindrical cells have already been fabricated for commercialization evaluation.

# Acknowledgements

The author would like to express his gratitude and appreciation to the following people for their guidance and assistance towards completion of the thesis:

First of all, I would like to express my sincere gratitude to my project supervisor, Professor Chen Xiaodong for providing me with the opportunity and privilege to expose to the cutting-edge research on lithium-ion battery. Thanks to his patience, continuous guidance and precious advice along the way, without such invaluable supervision, I would not advance so far in my PhD study.

Secondly, I would like to give grateful thanks to Dr. Ma Bing for granting me the access to work and study in NEW-CREATE program. I benefit a lot from her training on carrying out administrative work and time management as well as her suggestions and recommendations in carrying out all the projects.

Thirdly, I am grateful to all seniors and peers who have assisted me in designing research projects, carrying out experiment and presenting the scientific data. Special thanks are given to Dr. Yin Shengyan, Dr. Zhang Yanyan and Dr. Tang Yuxin who trained me on the assembly of batteries and characterization of materials. My gratitude also goes to other group members, especially to Dr. Lang Xianjun, Dr. Ding Bo, Mr. Zhou Hua and Mr. Lv Zhisheng for their inspiration, share of knowledge and encouragement. Furthermore, thank the undergraduate students, Mr. Li Wenlong, Mr. Wei Jiaqi and Ms. Zhou Xinran who assisted me in drawing the schematics for better illustration of scientific ideas.

Following on, I sincerely thank the thesis advisory committee member; special gratitude goes to Professor Christian Kloc for his critical comments and invaluable advice on improving the overall thesis and presentation. I would like to acknowledge the financial support from the National Research Foundation (NRF) of Singapore under the CREATE program on “Nanomaterials for Energy and Water Management” (NEW-CREATE) and the technical support from FCATS (Facilities for Characterization, Analysis and Tests) and other technical staff.

Last but not least, I would like to take this opportunity to thank my family members for their support along the way. The deepest thanks go to my beautiful wife, who constantly motivates me for the discovery of new knowledge during my ups and downs. Her continuous support and encouragement shines like a lighthouse in my life, pointing out the way forward to a bright dawn.

# Table of Contents

# Table Captions

# Figure Captions

## Abbreviations

| | |
|---|---|
| AC | Activated Carbon |
| BET | Brunauer–Emmett–Teller |
| CE | Columbic Efficiency |
| CNT | Carbon Nanotube |
| cP | Centipoise |
| CPE | Constant Phase Element |
| CV | Cyclic Voltammetry |
| DEC | Diethyl Carbonate |
| $D_{Li}$ | Chemical Diffusion Coefficient |
| EC | Ethylene Carbonate |
| EDLC | Electrochemical Double Layer Capacitor |
| EES | Electrochemical Energy Storage |
| EIS | Electrochemical Impedance Spectroscopy |
| EM | Electron Microscopy |
| EV | Electric Vehicle |
| FESEM | Field Emission Scanning Electron Microscopy |
| FRA | Frequency Response Analyzer |
| HEV | Hybrid Electric Vehicle |
| HRTEM | High Resolution Transmission Electron Microscopy |
| HTNT | Hydrogen Titanate Nanotube |
| LIB | Lithium-ion Battery |
| LIC | Lithium-ion Hybrid Capacitor |
| MM | Mechanically Mixed |
| OCV | Open-circuit Voltage Hydrogen Titanate Nanotube |
| PVDF | Polyvinylidene Fluoride |
| $R_{ct}$ | Charge Transfer Resistance |
| RGO | Reduced Graphene Oxide |
| SEI | Solid Electrolyte Interphase |

| | |
|---|---|
| SHE | Standard Hydrogen Electrode |
| SEM | Scanning Electron Microscopy |
| TEM | Transmission Electron Microscopy |
| UV | Ultraviolet |
| XRD | X-ray Diffraction |

# Chapter 1

# Introduction

*This chapter presents the hypothesis, objectives and overview of the dissertation and summarizes the key contributions and outcomes originated from this thesis. Firstly the application of* $TiO_2$ *(B) materials as promising anode candidate of high power electrochemical energy storage (EES) devices will be introduced, followed by the hypothesis to improve the electrical conductivity of* $TiO_2$ *(B) by integration of anatase phase. Next the objective and scope of the dissertation, which is to develop* $TiO_2$ *materials for high power and long life EES devices, will be illustrated in detail. Then the outline of this dissertation will be summarized in the overview section and the novelty and outcomes are finally presented.*

## 1.1 Hypothesis/Problem Statement

The development of sustainable city requires the adoption of sustainable energy resources as substitutes to conventional fossil fuels. However, due to the intermittency problem encountered by common renewable energy resources like solar and wind, fast charging and long life electrochemical energy storage (EES) devices are needed for load balancing and smart distribution of the generated electricity.[1] In particular, fast charging lithium-ion batteries (LIBs) and lithium-ion hybrid capacitors (LICs) are being studied extensively in recently years.[2-4] To achieve fast charging performances with long cycle life, these systems require different materials selection and design strategy compared to conventional LIBs for portable electronics. In such regards, $TiO_2$ (B) has been considered as one of the most promising fast charging electrode materials owing to its open structure and pseudocapacitive bulk storage behavior.[5-7] In addition, the high lithiation voltage (~ 1.5 V) falls inside the stability window of common organic electrolyte, which improves the cycling performances and safety characteristics.[8] However, fast charging capabilities require a well balance between ionic and electronic conduction, while $TiO_2$ (B) materials feature excellent lithium ion diffusion properties, the intrinsic low electrical conductivity (~ $10^{-10}$ S $cm^{-1}$)[9] originating from the large band gap (> 3.0 eV)[10] hinders its practical adoption.[11, 12] Conventional strategies to improve the electrical conductivity including mixing with conductive carbon,[6, 13, 14] surface bonding with graphene[15-17] or doping with aliovalent atoms,[9, 18] while these strategies are effective to improve the high rate performances, a massive amount of inactive conductive additives (> 15 wt%) is introduced to maintain the electrical percolation pathways, which decreases the overall energy of the devices significantly. Therefore, it is highly imperative to develop novel approaches which maximize the total amount of active materials to improve the electrical conductivity $TiO_2$ (B).

The lithiation reaction of $TiO_2$ (B) takes place at voltage around 1.0-3.0 V (vs. $Li^+/Li$), where conventional carbon additives contributes negligible capacity. To maximize the overall electrode energy density, the conductive additives should store lithium ions reversibly in similar voltage range as $TiO_2$ (B), while providing higher electrical conductivity before the onset of its major lithiation reaction between 1.4-1.6 V. Taking these requirements into consideration, anatase $TiO_2$ serves as promising candidate. Firstly, it has a similar lithiation voltage range (1.0-3.0 V) as $TiO_2$ (B) with main working potential around 1.75 V during lithiation.[19-22] Secondly, although pristine anatase is a poor conductor, recent studies show that the electrical conductivity of anatase phase improves significantly during the lithiation reaction due to the formation of a highly conductive solid solution of lithium with tetragonal anatase.[23] As the solid solution is formed at potential higher than 1.75 V during lithiation, we expect that the *in situ* formed conduction pathways could enhance electrical conductivity and boost the high rate capacities in $TiO_2$ (B), while still maintain relatively high energy densities at low rate since all $TiO_2$ materials are active.

### 1.1.1 Hypothesis 1: Dual Phase $TiO_2$ Materials Feature High Rate Performances Compared to Pure Phase $TiO_2$ (B)

Although $TiO_2$ (B) materials are poor electron conductor with large band gap of ~ 3.0 eV, the integration with anatase polymorph is expected to improve its electrical conductivity during the lithiation process since the main reaction of anatase phase occurs in high voltage potential around 1.75 V. In presence of good percolation pathways, the *in situ* formed conductives (lithiated anatase) will lead to high rate performances of $TiO_2$ (B) whose lithiation reaction lies in a lower range of 1.4-1.6 V with fast diffusion kinetics. It is foreseen that the dual phase $TiO_2$ materials with $TiO_2$ (B) as backbone and anatase as conductives additives will have much better high rate capacities even without any conductive carbon additives.

### 1.1.2 Hypothesis 2: Pre-lithiation Process Can Improve the Performances of $TiO_2$ Nanotubes for High Power LIC

Followed by the hypothesis that the lithiation could improve the electrical conductivity of the pristine $TiO_2$ materials, it is foreseen that pre-lithiation process will significantly boost the performance of the LICs bade on $TiO_2$ anode owing to better electrical and ionic conduction. Compared to conventional process of blending with large amount of additives, the introduction of lithium ions is advantageous: firstly, the mass of lithium compared to $TiO_2$ is negligible especially at low concentration; secondly, the slow pre-lithiation process will transform not just the surface of $TiO_2$ materials, but also the bulk of it potentially into highly conductive domains. Lastly, the process can improve the first cycle Columbic efficiency of the system and preserve the active materials contents. By testing this hypothesis, the first hypothesis about lithiation-induced conductivity in $TiO_2$ will be further strengthened; such findings serve as guideline for the practical adoption of $TiO_2$ materials in fabricating high power, long life EES devices.

### 1.1.3 Hypothesis 3: It is Plausible to Fabricate High Energy LIBs Based on $TiO_2$ Anode and High Voltage Cathode Formulated by Water Soluble Sericin Binder

Although $TiO_2$ materials features high rate performances, the operation voltage (~ 1.5 V) is very high as anode materials, thus the overall energy density is very limited coupled with commercial cathode operated below 4.5 V. Since the total energy is proportional to both capacity and voltage, increasing the operation voltage will result in enhancement of total energy, thus high voltage cathode materials such as $LiNi_{0.5}Mn_{1.5}O_4$ (~ 4.75 V) are highly desirable. However, at potential above 4.5 V, the commercial carbonate-based electrolyte will be oxidized and the carbon black additives are subjected to solvent co-intercalation, therefore a stable passivation layer for both carbon black additives and active materials is needed for high rate cycling of the cathode. In such regards, auxiliary binders with better surface coverage and interaction with active materials become important. The water soluble sericin binder with abundant surface hydroxyl and carboxyl groups is expected to form better passivation layer and thus enables high rate performances with high voltage LNMO cathodes. Consequently, high energy LIB cells based on $TiO_2$ anode and sericin formulated LNMO cathode can be achieved.

## 1.2 Objectives and Scope

The objective of this thesis is to develop $TiO_2$ based materials for high power, long life EES devices. The ultimate goal is to achieve a charging time of 6 min and cycle life of 20 years (that translates to more than 7300 cycles assuming one charge per day). In order to achieve the goal, the scope of the thesis is divided into the following part:

1. Establishing a method to improve the electrical conductivity of the $TiO_2$ (B) electrode while maximizing the total amount of active components. This is to ensure that the total energy of the battery cells is optimized.
2. Establishing a method to increase the energy and power performance of $TiO_2$ materials in LICs for the practical adoption. In this regards, a pre-lithiation process in $TiO_2$ is proposed for the first time.
3. Develop water soluble binder materials to form stable passivation layer on high voltage cathode for fabrication of high energy LIBs based on $TiO_2$ anode.

### 1.3 Dissertation Overview

The thesis addresses the low electrical conductivity problems associated with $TiO_2$ anode materials for fast charging electrochemical energy storage (EES) devices. The structure of this thesis is illustrated below:

*Chapter 1* outlines the rationale behind the project and provides the research goals, scope and hypothesis of this thesis.

*Chapter 2* reviews the literature concerning the development of fast charging EES devices with $TiO_2$ (B) anode candidate. The challenges and proposed solutions studied in this thesis will be presented in detail.

*Chapter 3* discusses the rationale behind the selection of the $TiO_2$ nanotubes platform and the principles underlying characterization techniques and methods of data analysis.

*Chapter 4* elaborates that the dual phase $TiO_2$ nanotubes feature much higher lithiation induced conductivity and high rate capacities compared to its pure phase $TiO_2$ (B) counterpart.

*Chapter 5* elaborates that the electrical conductivity of dual phase $TiO_2$ nanotubes can be significantly improved via the pre-lithiation approach. The overall energy and power densities of the LICs based on pre-lithiated $TiO_2$ nanotube anode can be enhanced greatly.

*Chapter 6* elaborates that the high energy LIBs based on $TiO_2$ nanotube anode could be achieved with high voltage cathode materials formulated by water soluble sericin binder.

*Chapter 7* concludes the thesis by drawing together the threads of each section and provides recommendations for the future work.

## 1.4 Findings and Outcomes

This research leads to several novel outcomes by:

1. Establishing an additive-free $TiO_2$ nanotube platform to probe the change of electrical and ionic conductivity during the lithiation process.
2. Demonstrating that dual phase $TiO_2$ nanotubes have better high rate electrochemical performances than pure phase $TiO_2$ (B) nanotubes owing to the high conductivity induced in the early stage of lithiation.
3. Demonstrating for the first time, that electrochemical pre-lithiation could significantly enhance the high rate performances of the lithium-ion hybrid capacitors (LICs) based on $TiO_2$ nanotube anode.
4. Discovering that the activated carbon cathode could feature dual ion adsorption mechanism in single cell of LIC with pre-lithiated $TiO_2$ nanotube anode, which could reduce the amount of carbon cathode and improve the overall energy density of the system.
5. Developing a new protein-based water soluble binder which could provide a stable passivation layer on the high voltage cathode materials for high energy LIBs.

## References

[1] B. Dunn, H. Kamath, J.-M. Tarascon, *Science* **2011**, *334*, 928.

[2] P. G. Bruce, B. Scrosati, J. M. Tarascon, *Angew. Chem. Int. Ed.* **2008**, *47*, 2930.

[3] L. Ji, Z. Lin, M. Alcoutlabi, X. Zhang, *Energy Environ. Sci.* **2011**, *4*, 2682.

[4] K. Naoi, W. Naoi, S. Aoyagi, J.-i. Miyamoto, T. Kamino, *Acc. Chem. Res.* **2013**, *46*, 1075.

[5] M. Zukalová, M. Kalbáč, L. Kavan, I. Exnar, M. Graetzel, *Chem. Mater.* **2005**, *17*, 1248.

[6] Y. Ren, Z. Liu, F. Pourpoint, A. R. Armstrong, C. P. Grey, P. G. Bruce, *Angew. Chem. Int. Ed.* **2012**, *51*, 2164.

[7] A. G. Dylla, G. Henkelman, K. J. Stevenson, *Acc. Chem. Res.* **2013**, *46*, 1104.

[8] N. Takami, Y. Harada, T. Iwasaki, K. Hoshina, Y. Yoshida, *J. Power Sources* **2015**, *273*, 923.

[9] Y. Zhang, Q. Fu, Q. Xu, X. Yan, R. Zhang, Z. Guo, F. Du, Y. Wei, D. Zhang, G. Chen, *Nanoscale* **2015**, *7*, 12215.

[10] D. Yang, H. Liu, Z. Zheng, Y. Yuan, J.-c. Zhao, E. R. Waclawik, X. Ke, H. Zhu, *J. Am. Chem. Soc.* **2009**, *131*, 17885.

[11] V. Aravindan, J. Gnanaraj, Y.-S. Lee, S. Madhavi, *Chem. Rev.* **2014**, *114*, 11619.

[12] M. Fehse, E. Ventosa, *ChemPlusChem* **2015**, *80*, 785.

[13] H. Liu, Z. Bi, X. G. Sun, R. R. Unocic, M. P. Paranthaman, S. Dai, G. M. Brown, *Adv. Mater.* **2011**, *23*, 3450.

[14] S. Liu, H. Jia, L. Han, J. Wang, P. Gao, D. Xu, J. Yang, S. Che, *Adv. Mater.* **2012**, *24*, 3201.

[15] C. Chen, X. Hu, Y. Jiang, Z. Yang, P. Hu, Y. Huang, *Chemistry – A European Journal* **2014**, *20*, 1383.

[16] V. Etacheri, J. E. Yourey, B. M. Bartlett, *ACS Nano* **2014**, *8*, 1491.

[17] X. Yan, Y. Li, M. Li, Y. Jin, F. Du, G. Chen, Y. Wei, *J. Mater. Chem. A* **2015**, *3*, 4180.

[18] S. Goriparti, E. Miele, M. Prato, A. Scarpellini, S. Marras, S. Monaco, A. Toma, G. C. Messina, A. Alabastri, F. D. Angelis, L. Manna, C. Capiglia, R. P. Zaccaria, *ACS Appl. Mater. Interfaces* **2015**, *7*, 25139.

[19] K. Saravanan, K. Ananthanarayanan, P. Balaya, *Energy Environ. Sci.* **2010**, *3*, 939.

[20] G. Zhang, H. B. Wu, T. Song, U. Paik, X. W. Lou, *Angew. Chem. Int. Ed.* **2014**, *126*, 12798.

[21] W. Li, F. Wang, Y. Liu, J. Wang, J. Yang, L. Zhang, A. A. Elzatahry, D. Al-Dahyan, Y. Xia, D. Zhao, *Nano Lett.* **2015**, *15*, 2186.

[22] Y. Tang, Y. Zhang, X. Rui, D. Qi, Y. Luo, W. R. Leow, S. Chen, J. Guo, J. Wei, W. Li, J. Deng, Y. Lai, B. Ma, X. Chen, *Adv. Mater.* **2016**, *28*, 1567.

[23] C. Kim, R. Buonsanti, R. Yaylian, D. J. Milliron, J. Cabana, *Adv. Energy Mater.* **2013**, *3*, 1286.

# Chapter 2

## Literature Review

*In this chapter, the importance and requirement for electrochemical energy storage devices will be reviewed first, followed by the detail illustration of the fast charging lithium-ion batteries and lithium-ion hybrid capacitors. The materials challenges for both kinds of devices are listed out. Then a comprehensive review on the role of* $TiO_2$ *(B) as promising fast charging and long life anode materials will be presented with special focus on the approaches to improve the electrical conductivity. Finally, the dissertation in context of literature will be discussed.*

## 2.1 Overview of Electrochemical Energy Storage System

The proliferation of human society requires uninterruptable energy supplies. Conventional fossil fuels have been the primary energy of choice for the past centuries. However, the depletion of fossil fuel and climate changes stimulated from pollution of burning such materials has boosted a shift towards sustainable energy resources.[1] However, unlike conventional energy sources of fossil fuels stored in form of chemical energy which can be withdrew conveniently, the sustainable energy sources such like solar or wind suffer from the intermittency problems, which requires proper energy storage systems for load leveling and electricity consumption management. In addition, to build up more sustainable city, transportation is another important area where the penetration of electric vehicles is expected to grow rapidly to reduce the overall pollution inside the city (Figure 2.1). To tailor the needs of renewable energy and future city development, the electrochemical chemical energy storage (EES) systems[2] are highly demanded since they offers many desirable features, including environmental benignness, high efficiency, long cycle lifetime with low maintenance cost, and flexible format to tailor the needs of different functions for electricity distribution.

**Figure 2.1** Schematics on the role of EES devices for the storage of electricity generated from the renewable resources and the distribution of electrical energy for living and transportation.

A summary on the energy and power densities of common EES systems for energy storage is shown in Figure 2.2. These systems can be classified into two categories, the rechargeable batteries and capacitors. Rechargeable batteries in general offer high energy density than supercapacitors, however, the lifetime and power density is inferior to that of the capacitors. Lead-acid batteries are the earliest rechargeable batteries, due to its low cost and easiness of fabrication, the first electric cars back in the late nineteen century is equipped with lead-acid batteries and could reach a speed of 30 m/s;[1] However, the energy density is below 50 Wh $kg^{-1}$, and cycle life is limited as the reaction consumed electrolyte and causes structural changes in the active electrode materials. Later nickel based chemistries were developed for secondary batteries, in particular the Ni-Cd and Ni-Metal hydride (Ni-MH) batteries. They show improvement on the overall energy and power density as well as cycling life but suffer from memory effects. In 1991, Sony Corporation commercialized the lithium-ion batteries (LIBs)[3] to be used in mobile electronics, which yields significant improvement on the overall energy densities and cycling life by maximizing the following factors: first of all, high output voltage is achieved due to large chemical potential difference between the cathode and anode materials. The standard redox potential of $Li^+/Li$ is the lowest (-3.05 V vs. SHE), the graphite materials has a lithiation voltage only 0.1 V higher than that of lithium metal. Therefore, typically the commercial graphite-based LIBs with $LiCoO_2$ cathode operates at voltage ~ 3.7-3.8 V. Secondly, the specific capacity of the reactants is high, typically the graphite anode shows high theoretical specific capacity of 372 mAh $g^{-1}$ and practically 350 mAh $g^{-1}$ can be reached. Thirdly, the operation of the LIB cells is based on the insertion and extraction of lithium ions between anode and cathode, the electrolyte is not consumed during the reaction; In addition, the shuttle effect of lithium ion between anode and cathode does not alter the host structure significantly, the preservation of active materials structure is beneficial for the long term cycling of LIBs. Apart from LIBs, lithium-ion hybrid capacitors (LICs) are also attractive with high power and ultralong cycle life.[4, 5] Although the cost of supercapacitors per energy is much higher than that of LIBs, advantages can be realized with the lifetime cost considering the exceptional long cycle life. The long-lasting, high power, environmentally friendly EES systems would greatly advance the process for the development of future sustainable city.

In the following part, fast charging LIBs and hybrid capacitors will be reviewed in detail.

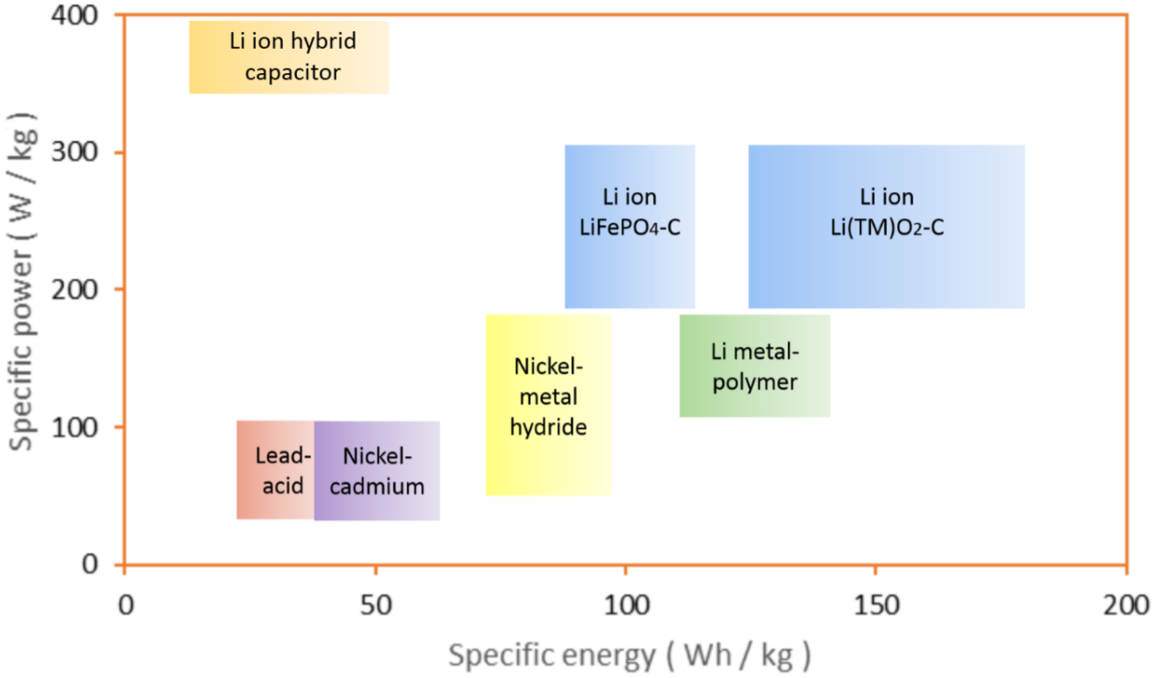

**Figure 2.2** Gravimetric power and energy densities for different electrochemical energy storage (EES) systems.

## 2.2 Fast Charging Lithium-ion Batteries

Rechargeable batteries of different chemistries have been developed for more than 150 years for various applications. In the past 20 years, the proliferation of mobile electronics and communication devices have increased the demand for rechargeable lithium-ion batteries (LIBs) because of their high energy density, long cycle life and long term stability.[6, 7] Conventional LIB cells are built from graphite anode and $LiCoO_2$ cathode with a porous membrane separator immersed in electrolytes. This combination of battery cells has reached an energy density five times higher than the lead-acid batteries and revolutionized the portable electronics industry. During charging/discharging cycle, lithium ions are shuttled between electrodes and electrons are circulated among external loads. Such topotactic reaction (without destruction of the core structure of active materials) has enabled LIB systems better stability and longer cycle life.[8, 9] Nowadays, apart from the portable electronics, LIBs have also shown great potential for the large-scale applications like electric vehicles (EVs) and grids energy storage[10] (Figure 2.3).

**Figure 2.3** Application of lithium-ion batteries (LIBs) in a variety of different fields ranging from small scale portable electronics and large scale energy storage systems.

The battery requirements of those large storage systems differ from that of the small scale electronics. Specifically, the power of the battery in such systems is critical merit for loading balancing or acceleration of the vehicles. In addition, safety of battery cells is of great concern as hundreds of cells are packed in order to deliver the required outputs. Finally, prolonged lifetime of batteries is expected in such applications to minimize the lifetime maintenance and replacement cost. To meet the requirement of power, cycle life and safety, graphite materials are insufficient to satisfy the needs of electric vehicles because of inherent safety problems of the electrode materials.[11] In particular, the lithiation potential of graphite is around 0.1 V vs. $Li^+/Li$, which is close to the lithium deposition voltage. Upon fast charging, the lithium metal dendrites will likely to form due to slow lithium intercalation kinetics into graphite, which causes short circuit of battery. Apart from the safety concerns, graphite based anode has a specific galvanic capacity of only 372 mAh $g^{-1}$ (based on the product of $LiC_6$), which is not sufficient to meet the energy density for battery of small portable electronics.

Different anode materials as alternatives to graphite have been studies for the past decades and the general mechanism towards lithiation can be classified into three categories, including insertion, alloying and convention-based mechanisms (Figure 2.4).[12] Insertion mechanism is already commercialized with limited capacity per mass. While alloying and conversion mechanism offers potentially very high capacity; the significant volumetric expansion (> 100 %) induced during the reaction limits the cycle life. For example, alloying-type silicon based anode materials have the highest specific capacity of 4200 mAh/g; however the large volume expansion of nearly 400% upon full lithiation results in severe pulverization problems, which hinders the practical application of silicon anodes.[13] For the conversion mechanism, it is limited to transition metal oxides in form of nanomaterials. Typically such reaction is even more destructive in altering the structure of the materials compared to alloying-based mechanism.[14, 15] In searching for the proper anode materials with high power density and long cycle life, the combination of capacitor-like rate capacities and battery-like energy density are highly desirable. Until now, the widely used fast charging anode material is spinel lithium titanate $Li_4Ti_5O_{12}$ (LTO). LTO is a zero-strain lithiation material, with almost no volumetric change during the lithiation process. Thus the lithiation reaction is kinetically fast, highly stable and reversible.[16] In addition, LTO has a high lithium-insertion voltage (ca. 1.55 V vs $Li^+/Li$), which prevents reduction of electrolyte on the electrode surface, suppressing the formation of solid electrolyte interphase (SEI) layer. The absence of SEI layer results in much enhanced safety. Therefore, the LTO-based LIBs have long cycle life, high power density and improved safety.[17, 18] Although much effort have been devoted to improve the rate performances of LTO, the low specific capacity 175 mAh $g^{-1}$ is only half that of graphite (372 mAh $g^{-1}$), therefore enhancement of the specific capacity while retaining the high rate capacity is highly desirable. In such regards, $TiO_2$ anode materials with a theoretical capacity of 335 mAh $g^{-1}$ serves as one promising candidate.[19, 20] Similar to LTO, $TiO_2$ operates in voltage range of 1-3 V, which avoids the formation of SEI layer and improves the safety of the cell. The volumetric expansion for $TiO_2$ is small (< 4 %) upon lithiation, thus enabling long term stability and long cycle life. Furthermore, the open channel structure in $TiO_2$ (B) has stimulated pseudocapacitive storage behavior, with very fast diffusion kinetics.[21] Finally, the cost of $TiO_2$ materials is lower and is promising for massive industrial adoption.

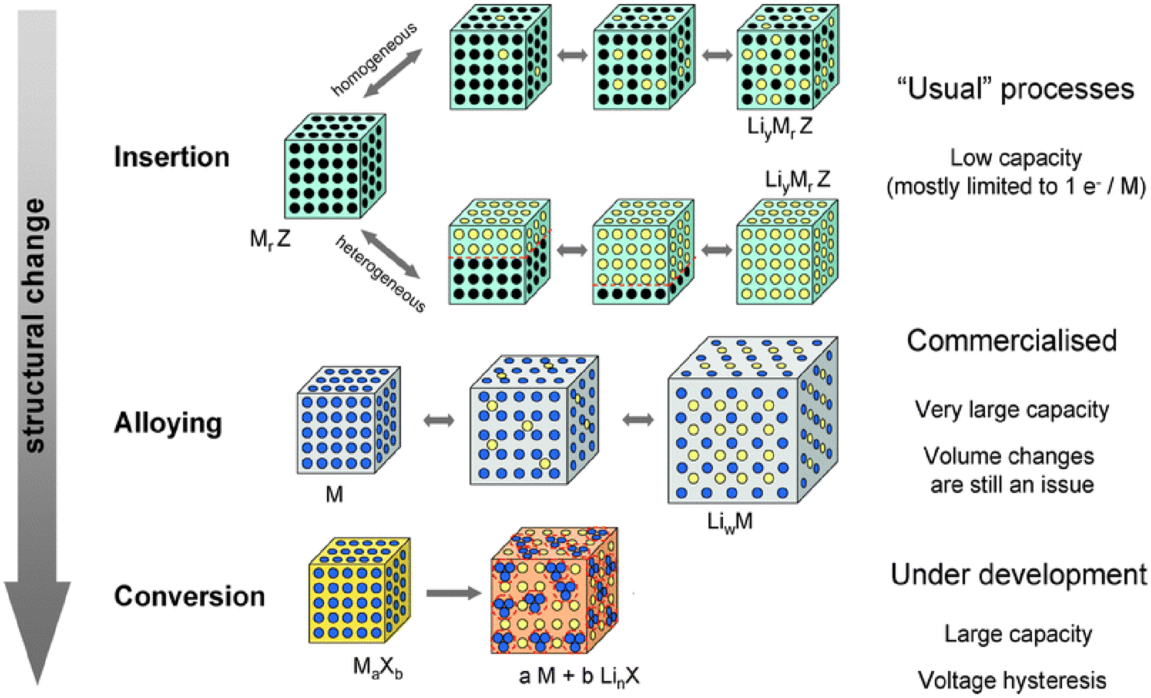

**Figure 2.4** Schematic representations of the different reaction mechanisms of common anode materials for lithium batteries. Reproduced with permission from Reference 12. Copyright 2009, Royal Society of Chemistry.

## 2.3 High Power Lithium-ion Hybrid Capacitor

Although Lithium-ion batteries (LIBs) feature high voltage with high energy density, the cycle life, operation temperature, and power density is hindered by the sluggish faradic reactions. Typically for portable electronics, the LIB cycle life is only 300-500 cycles, whereas power oriented LIBs achieve cycle life larger than 1000 cycles at cost of lower energy density.[6, 22, 23] Potential safety hazard may arise and is always a concern in LIBs due to the inherent instability of the solid electrolyte interphase (SEI) and high voltage cathode.[24] To alleviate such problem and provide exceptional long cycle life, the lithium-ion hybrid capacitors (LICs) is an attractive alternative to LIBs. LIC utilizes both Faradic and non-Faradic processes to achieve high energy density than conventional electrochemical double layer capacitor (EDLC) and high power density than LIBs without sacrificing the cyclability and compromising the safety.[4, 25] The schematics on the operating mechanism of LICs are shown in Figure 2.5. In typical LICs, the battery-like anode is based on Faradic intercalation of lithium ions which provides the energy source, and the capacitor-like cathode is based on non-Faradic adsorption of anions which improves the power output.

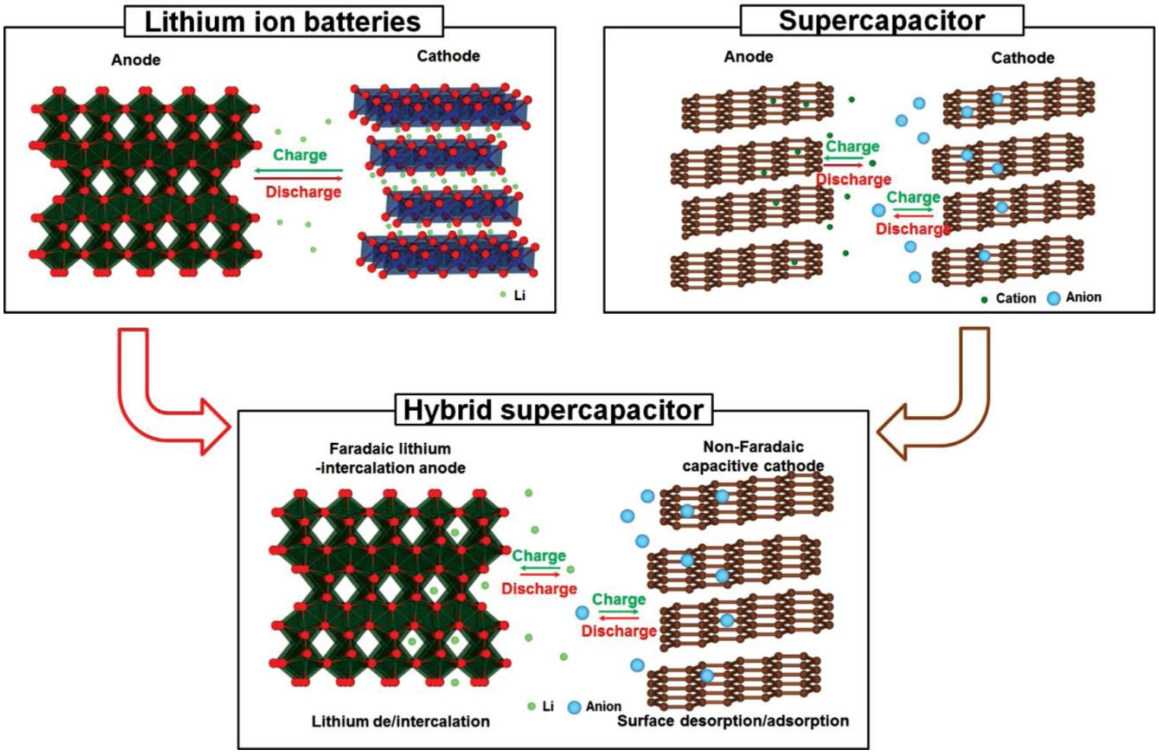

**Figure 2.5** Illustration on the operation mechanism of typical LIC, the hybrid systems uses capacitive-cathode and lithium intercalation anode. Reproduced with permission from Reference 25. Copyright 2013, Wiley.

To achieve high power density and long cycle life, highly stable intercalation anode materials are necessary, the materials need to be structurally robust and operate safely over the potential range. In general, the following points[26] must be considered:

(i) The stability range of the conventional electrolyte $LiPF_6$ in carbonate solvent is between 1-4.5 V, the electrolyte will be reduced to form the so-called SEI which degrades the power densities and reduces the overall cycle life. Above the 4.5 V, oxidation of electrolyte occurs and gases will be released causing the explosion hazards. Therefore, the intercalation anode materials need to operate in this voltage range.

(ii) The cycle life of conventional EDLC can easily go beyond 500,000 deep cycles. To achieve such long cycle life in LICs, the insertion anode is expected to have highly robust structure to sustain long term cycling; in particular, the volumetric expansion upon lithiation should be minimized.

(iii) To facilitate the transport of lithium ions, nanostructured materials are desirable. However, the conductivity of such materials is relatively poor, thus requiring large amount of conductive additives for fast electron transport. These additives are typically electro inactive; therefore a reduction in overall energy and power densities of the LIC packs is expected. To further improve the overall energy density, an effective approach should be developed to minimize the usage of conductives during electrode formulation.

Considering the above requirements, it is not surprising that the first LIC was assembled by G.G. Amatucci with the $Li_4Ti_5O_{12}$ (LTO) as the anode and activated carbon as the cathode.[4] The energy density of a packed cell is above 10 Wh $kg^{-1}$ at power density of 1000 W $kg^{-1}$, with an ultralong cycle life of 450,000 cycles achieved at 40 C. LTO is very robust material towards lithium intercalation, with stable voltage around 1.55 V and there is almost no volumetric change during the reaction. Compared to LTO, $TiO_2$ is also attractive materials with larger specific capacity. In particular, the open channel structure in $TiO_2$ (B) enables pseudocapacitive charge storage mechanism with very fast lithium ion diffusion kinetics.[27] Furthermore, the small volumetric expansion and excellent structure robustness enables long term cycling. In the following section, the application of $TiO_2$ (B) as fast lithium-ion storage materials will be reviewed in detail.

## 2.4 $TiO_2$ (B) as Attractive Fast Charging Anode Material

From the above literature, it is observed that titanium dioxide has been considered as one of the most promising anode materials for high power applications in LIBs and LICs. $TiO_2$ has low volume expansion upon lithiation (< 4%) and the high lithiation potential around 1.4-1.8 V suppresses the formation of SEI layer and lithium dendrites. Compared with graphite, the absence of SEI and little structural changes upon lithiation favors long cycle life and fast reaction kinetics. The lithium intercalation reaction of $TiO_2$ can be commonly expressed by the following equation:

$$xLi + TiO_2 + xe^- \leftrightarrow Li_xTiO_2 \tag{2.1}$$

Based on the amount of Lithium ions that can be inserted, the theoretical specific capacities of different $TiO_2$ polymorphs[28] are shown in Figure 2.6. Among the common polymorphs, anatase and $TiO_2$ (B) favor larger amount of lithium ion insertion and have been investigated extensively. In particular, the 6 nm anatase nanoparticles[29] could deliver a stable capacity of 125 mAh $g^{-1}$ at discharging rate of 12 A $g^{-1}$(with conductive carbon content of 45 wt%), similar results can be achieved with mesoporous ordered 3D anatase structures with less conductive carbons (15 wt %).[30] In recent years, $TiO_2$ (B) has raised up more attention because it has the highest theoretical specific galvanic capacity (335 mAh $g^{-1}$), [31, 32] which is comparable to that of the graphite (372 mAh $g^{-1}$) and much higher than that of the LTO (175 mAh $g^{-1}$). In addition, the unique open channel structure of the $TiO_2$ (B) polymorph enables pseudocapacitive lithium ion storage, which accounts for high rate capacities upon fast charging and discharging, making it more desirable for high power LIB applications such as hybrid electric vehicles (HEVs). In the following section, the synthesis methods and electrochemical performances of $TiO_2$ (B) based electrode will be reviewed in detail.

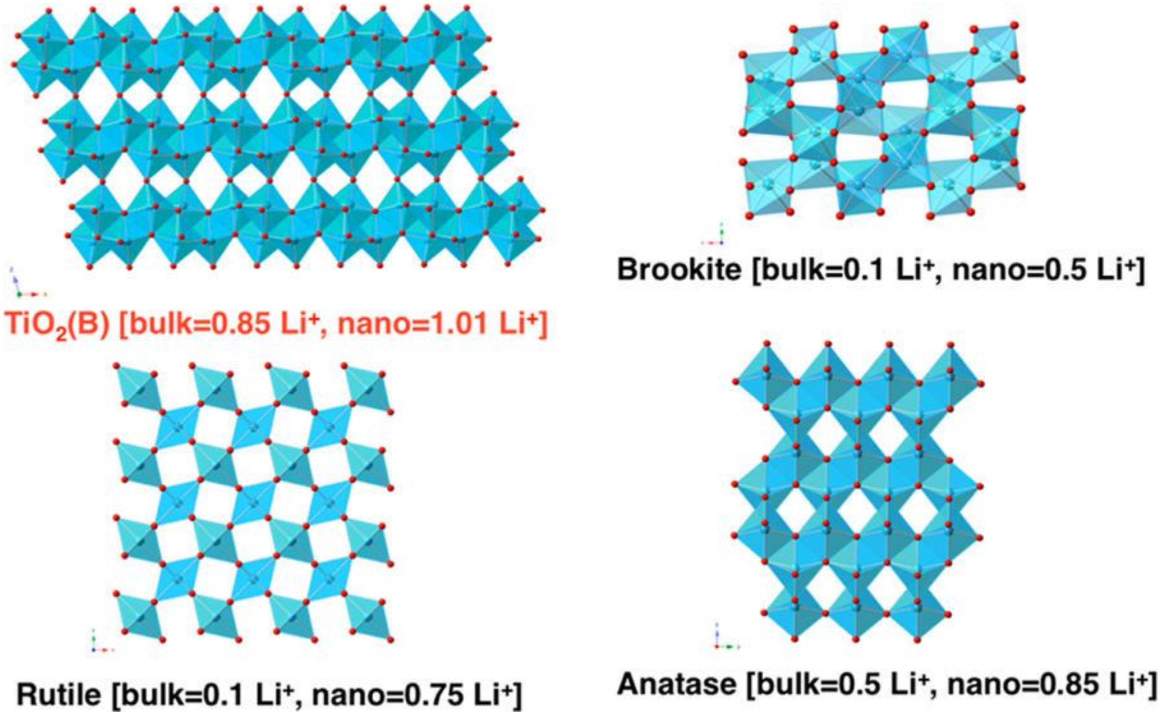

**Figure 2.6** Illustration on the crystal structure and lithium storage properties in different $TiO_2$ polymorphs. Reproduced with permission from Reference 28. Copyright 2013, American Chemical Society.

### 2.4.1 Synthesis of $TiO_2$ (B) Materials

#### 2.4.1.1 Solid State Synthesis

$TiO_2$ (B) was first synthesized via solid state method by Marchand et al. in the 1980s with layered $K_2Ti_4O_9$ as precursors followed by ion exchange and calcination.[33] It has monoclinic unit cell (space group $C2/m$) with $a$ =1.21787 nm, $b$=0.37412 nm, $c$ = 0.65249 nm, and $\beta$= 107.054°. The crystal structure of $TiO_2$ (B) is characterized by corrugated sheets of edge-and corner-sharing $TiO_6$ octahedra, while the parallel infinite open channels of $TiO_2$ (B) lattice facilitate proton and $Li^+$ ion insertion. The diameter of such $TiO_2$ (B) materials can go above 100 nm and the length is in range of several micrometers, therefore, it is considered as bulk $TiO_2$ (B).

#### 2.4.1.2 Hydrothermal Synthesis

Nanosized $TiO_2$ (B) materials can be obtained by hydrothermal method which was first developed by Kasuga's group to synthesize titanate nanotubes and nanowires.[34] Upon further heat treatment, the titanate structure will be transformed to either $TiO_2$ (B) or anatase depending on the annealing condition.[35, 36] In 2005, Peter Bruce et al. first investigated the lithium ion storage properties of $TiO_2$ (B) nanowires synthesized via such hydrothermal method with sodium hydroxide and $TiO_2$ anatase as starting precursors.[31, 32, 37] A higher charge-storage capacity of 305 mAh $g^{-1}$ (corresponding to $Li_{0.91}TiO_2$) and superior rate capacity (85 mAh $g^{-1}$ at 3 A $g^{-1}$) is observed for $TiO_2$ (B) nanowires. Furthermore, the same group also investigated the performances of $TiO_2$ (B) nanotubes [38-40] and $TiO_2$ (B) nanoparticulate [41, 42] as anode materials for LIB.

### 2.4.2 Lithium Storage Performances of $TiO_2$ (B) Materials

The lithium ion storage performance of bulk $TiO_2$ (B) materials was first investigated in 1980s. A maximum lithium uptake around 0.5 moles can be achieved with 1M $LiAsF_6$ in PC as the electrolyte.[43] The detail electrochemical performances of bulk $TiO_2$ (B) was studied by Toshiba Corporation in Japan.[44, 45] Pouch cell (2.8 Ah) fabricated by secondary spherical $TiO_2$ (B) particles coupled with $LiNi_{0.8}Co_{0.1}Mn_{0.1}O_2$ cathode could deliver high energy density of 100 Wh $kg^{-1}$, with capacity retention of 80% after 3,000 cycles at 1 C (1 C = 335 mA $g^{-1}$).[46] As for the nanosized $TiO_2$ (B), extensive performance evaluation is carried by Peter Bruce's group. A summary on the electrochemical performances of various morphologies of $TiO_2$ (B) are displayed in Figure 2.7.[41] All forms of $TiO_2$ (B) show a pair of peaks in the range of 1.45-1.65 V, corresponding to the intercalation of $Li^+$ into the A1 and A2 sites of $TiO_2$ (B) crystal structure. $TiO_2$ (B) nanotubes and nanoparticles demonstrate enhanced lithium storage capacity at low rate due to the free energy changes caused by strain-induced structural distortions, which helps to accommodate more lithium ions in the lattice.[28] Compared to anatase, The 3 nm $TiO_2$ (B) nanoparticles mixed with 15 wt% carbon additives could deliver high capacity of 125 mAh $g^{-1}$ at current rate of 18 A $g^{-1}$.

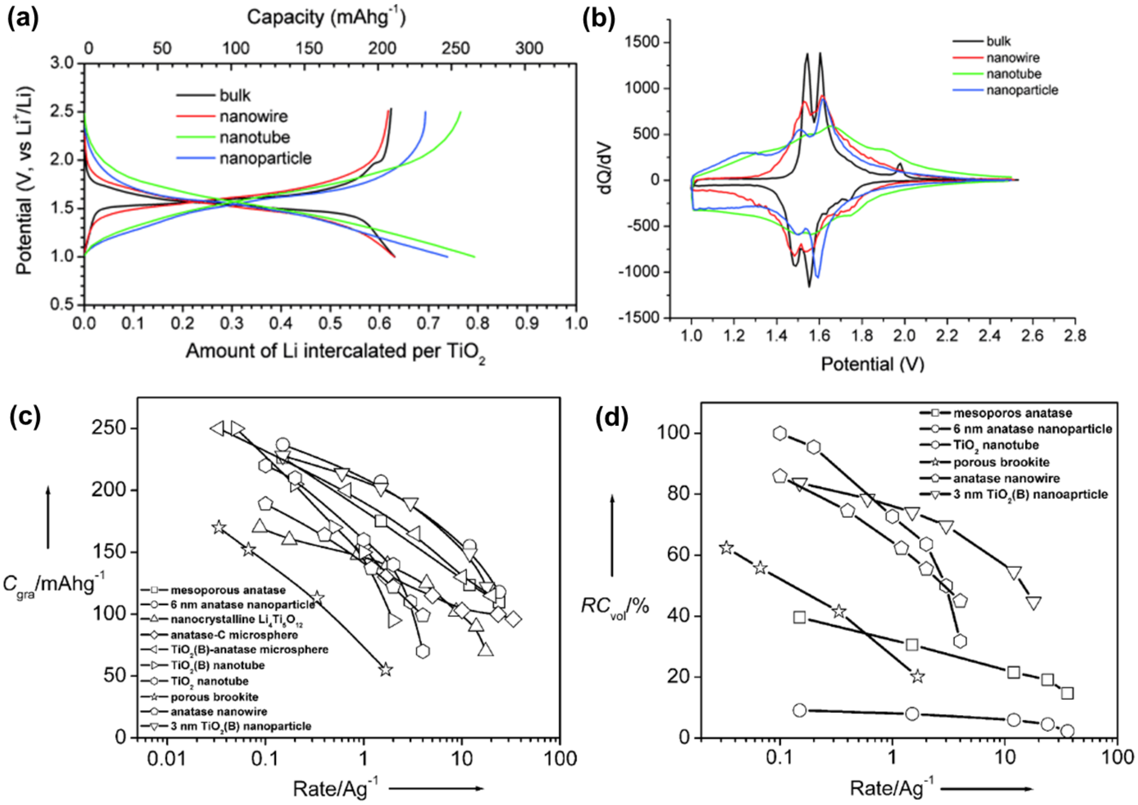

**Figure 2.7** a) Cyclic voltammograms (CVs) of different $TiO_2$ (B) electrodes b) Gravimetric capacity of different $TiO_2$ polymorphs as a function of rate. Reproduced with permission from Reference 41. Copyright 2012, Wiley.

### 2.4.3 Methodology to Improve Electrical Conductivity of $TiO_2$ (B) Electrode

Although $TiO_2$ (B) features pseudocapacitive charge storage mechanism with very fast diffusion kinetics, the intrinsic low electric conductivity (~ $10^{-10}$ S $cm^{-1}$) coming from the large band gap of (3.0 eV) hinders its practical applications.[47] Therefore various strategies have been employed to improve the electrical conductivity of $TiO_2$ (B) electrode. In general, these methods can be divided into three categories, including mixing with conductive additives, bonding with conductives and aliovalent ion doping; each strategy will be discussed in detail below.

#### 2.4.3.1 Mixing with Conductives

A straightforward strategy to improve the electrical conductivity is to mix $TiO_2$ (B) with conductives. In such regards, mesoporous $TiO_2$ (B) microspheres were synthesized in 2011 using silica as sacrificial template.[48] With a conductive carbon (Super P) content of 15 wt%, the material exhibits a superior capacity of 116 mAh $g^{-1}$ at high discharging rate of 60 C. Followed by this work, a hierarchical nanosheet-constructed porous $TiO_2$ (B) was developed and yields high capacity of 216 mAh $g^{-1}$ at a discharging rate of 10 C; However, the carbon contents increases to 20 wt%.[49] Generally for nanomaterials, more conductives are required to build up the electron percolation pathways. For example, the 3 nm $TiO_2$ (B) nanoparticles requires 15 wt% carbon additives to deliver high capacity of 125 mAh $g^{-1}$ at discharging rate of 18 A $g^{-1}$ (~54 C).[41] Very recently, $TiO_2$ (B) nanosheets were anchored on carbon nanofibers to form a flexible electrode; such flexible electrode could deliver a capacity of 97 mAh $g^{-1}$ at high rate of 30 C, but it contains enormous amount (85%) of conductive carbon fibers.[50]

#### 2.4.3.2 Bonding with Conductives

Direct mixing of the conductives with the $TiO_2$ (B) materials may result in poor interfacial reaction; in addition, agglomeration of the conductive particles further reduces the contact area with nanostructure $TiO_2$ (B) materials. One effective method to improve the interfacial bonding is by the formation of covalent bonds. Etacheri et al. first demonstrated the formation of Ti-C bond in the hybrid $TiO_2$ (B) / RGO system obtained through UV illumination of graphene oxide and $TiO_2$ (B) nanosheets.[51] The RGO contents in the hybrid structure is 20 wt%, while a capacity of 200 mAh $g^{-1}$ is obtained at high rate of 40 C. Inspired from this work, Huang and co-workers uses microwave assisted synthesis routes followed by pulse annealing for the reduction of graphene oxide with $TiO_2$ (B) nanosheets,[52] a capacity of 154 mAh $g^{-1}$ can be achieved at current rate of 12 A $g^{-1}$, however, apart from the 10 wt% graphene, another 10 wt% of super P is used during the electrode formation process. Similar methods was also used to bond $TiO_2$ (B) nanowires to nitrogen-doped graphene,[53] although exceptional high capacity of 101.6 mAh $g^{-1}$ is achieved at rate of 30 A $g^{-1}$, TGA analysis shows that the content of nitrogen-doped graphene is around 11 wt% and the electrode contains another 15 wt% of conductive Super P, such large amount of conductive additives renders the system unrealistic for practical adoption.

### 2.4.3.3 Doping with Aliovalent Atoms

To improve the bulk conductivity of $TiO_2$ (B) materials, aliovalent atom doping is generally required. Nitrogen doped $TiO_2$ (B) achieved a capacity of 153 mAh $g^{-1}$ at high rate of 20 C by addition of 20 wt% carbon additives.[54] Carbon-doped $TiO_2$ (B) nanowires can be synthesized using TiC as the precursor followed by the hydrothermal reaction in strong alkali solution, a stable capacity of 160 mAh $g^{-1}$ is delivered after 1,000 cycles with Columbic efficiency ~ 100%.[55] However, the carbon additives constitute as high as 20 wt% of the total electrode weight. In general, the doping of $TiO_2$ (B) fails to improve the electrical conductivity significantly, as the reduction on band gap is limited. For instance, the conductivity for pure $TiO_2$ (B) nanowires lies in order of $10^{-11}$ S $cm^{-1}$, while for nitrogen-doped sample, the conductivity increases 3 orders to $10^{-8}$ S $cm^{-1}$, which is still far below the value for graphite (~ $10^{5}$ S $cm^{-1}$). Therefore, large amount of carbon additives are required to achieve high rate performances.

The electrochemical performances of $TiO_2$ (B) materials with different electrode compositions are summarized in table 2.1.

**Table 2.1** Summary on the electrochemical performances of $TiO_2$ (B)-based electrodes with different approaches to improve the electrical conductivity

| Electrode materials | Specific capacity (mAh/g)/Current rate | Electrode composition | Reference (year) |
|---|---|---|---|
| Mesoporous $TiO_2$(B) microspheres | 165 (10 C[a])<br>116 (60 C) | 70:15:15[b] | [48] (2011) |
| Nanosheet constructed porous $TiO_2$ (B) | 216 (10 C)<br>150 (30 C) | 70:20:10 | [49] (2012) |
| $TiO_2$ (B) nanoparticles | 125 (18 A $g^{-1}$) | 70:15:15 | [41] (2012) |
| $TiO_2$ (B) nanosheet on carbon cloth | 160 (10 C)<br>97 (30 C) | 15:85:0 | [50] (2013) |
| $TiO_2$ (B) / RGO bonding | 200 (40 C) | 70:20:10 | [51] (2014) |
| $TiO_2$ (B) nanosheet / RGO bonding | 160 (6 A $g^{-1}$)<br>154 (12 A $g^{-1}$) | 72:18:10 | [52] (2014) |
| $TiO_2$ (B) nanowires / N-doped RGO | 220.7 (3 A $g^{-1}$)<br>101.6 (30 A $g^{-1}$) | 70:15:15 | [53] (2015) |
| Nitrogen doped $TiO_2$ (B) | 153 (20 C)<br>100 (100 C) | 70:15:15 | [54] (2015) |
| Carbon doped $TiO_2$ (B) | 160 (10 C) | 70:20:10 | [55] (2015) |

[a]: 1 C = 335 mA $g^{-1}$

[b]: the weight percentage of active materials, conductive carbon and binder

## 2.5 Questions Arising from How to Improve Electrical Conductivity of $TiO_2$ (B) while Maximizing the Active Materials Contents

Although different strategies have been implemented to enhance the electrical conductivity and high rate capacity of $TiO_2$ (B) electrode, these methods often requires complicated procedures such as microwave-assistance, UV illumination and heat treatment under inert gas environment. In addition, these approaches rely on the massive usage of conductive additives for fast charging, (e.g. more than 15 wt% conductive are used). The large amount of inactive carbon additives decreases the overall energy density of the battery cells significantly. The questions arise whether a simple method could be developed and utilized to improve the electrical conductivity of $TiO_2$ (B) electrode while maximizing the total amount of active materials.

The lithiation reaction of $TiO_2$ (B) takes place at voltage around 1.0-3.0 V (vs. $Li^+$/Li), while conventional carbon additives contributes negligible capacity between such voltage range. To maximize the overall electrode energy density, the conductive additives should store lithium ions reversibly in similar voltage range as $TiO_2$ (B), while providing higher electrical conductivity before the onset of its major lithiation reaction between 1.4-1.6 V. Taking these requirements into consideration, we foreseen that anatase $TiO_2$ serves as a promising candidate. Firstly, it has a similar lithiation voltage range (1.0-3.0 V) as $TiO_2$ (B) with main working potential around 1.75 V during lithiation, which is above the major lithiation reaction of $TiO_2$ (B). Secondly, although pristine anatase is a poor conductor with band gap larger than 3.0 eV, recent studies show that the electrical conductivity of anatase phase improves significantly during the lithiation reaction due to the formation of a highly conductive solid solution of lithium with tetragonal anatase,[56] thus the integration of anatase phase is expected to increase the electrical conductivity of $TiO_2$ (B) and improve the overall energy density.

## 2.6 PhD in Context of Literature

This thesis aims at fabricating high power electrochemical energy storage (EES) devices with dual phase $TiO_2$ nanotubes as the anode. In this thesis, an additive-free nanotube platform is used to investigate the performance of the $TiO_2$ (B) materials with anatase phase impurities. Such platform eliminates the usage of conductive carbons and polymeric binders and could accommodate the volumetric expansion of $TiO_2$ materials (~ 4 %) during lithiation, thus enables study on the change of conductivity during the lithiation process via the *in situ* electrochemical impedance spectroscopy (EIS). We first probe such conductivity change and conclude that the anatase phase serves as active conductive additives formed *in situ* prior to the main lithiation reaction of $TiO_2$ (B) which will improve high rate capacities while minimizing the loss in total energy. Followed by the above discovery, pre-lithiation technique is employed to improve the conductivity of dual phase $TiO_2$ nanotubes for high power lithium-ion hybrid capacitors (LICs). With pre-lithiated $TiO_2$ nanotubes, dual ion adsorption functions are discovered in activated carbon cathode in single LIC cell which could improve the overall energy density. Finally, to improve the energy density of high voltage $TiO_2$ based LIB cells, water soluble binder is used to passivate the high voltage cathode and achieve both high energy and high power. This dissertation unravels the importance of lithiation-induced conductivity in achieving high power density LIBs while optimizing the amount of active materials. Furthermore, the demonstration of pre-lithiated $TiO_2$ nanotubes as high power LIC and discovery of the dual ion adsorption mechanism of activated carbon in single cell is the first time in literature. Together with the discovery of new water-soluble sericin binder for the passivation of high voltage cathode, these findings provide guidance towards future design of high power $TiO_2$ materials for commercial adoption.

## References

[1] M. Armand, J. M. Tarascon, *Nature* **2008**, *451*, 652.

[2] B. Dunn, H. Kamath, J.-M. Tarascon, *Science* **2011**, *334*, 928.

[3] A. Yoshino, *Angew. Chem. Int. Ed.* **2012**, *51*, 5798.

[4] I. Plitz, A. DuPasquier, F. Badway, J. Gural, N. Pereira, A. Gmitter, G. G. Amatucci, *Appl. Phys. A* **2006**, *82*, 615.

[5] K. Naoi, S. Ishimoto, J.-i. Miyamoto, W. Naoi, *Energy Environ. Sci.* **2012**, *5*, 9363.

[6] J. M. Tarascon, M. Armand, *Nature* **2001**, *414*, 359.

[7] P. G. Bruce, B. Scrosati, J. M. Tarascon, *Angew. Chem. Int. Ed.* **2008**, *47*, 2930.

[8] J. B. Goodenough, *Acc. Chem. Res.* **2012**, *46*, 1053.

[9] J. B. Goodenough, K. S. Park, *J. Am. Chem. Soc.* **2013**, *135*, 1167.

[10] T.-H. Kim, J.-S. Park, S. K. Chang, S. Choi, J. H. Ryu, H.-K. Song, *Adv. Energy Mater.* **2012**, *2*, 860.

[11] C. M. Hayner, X. Zhao, H. H. Kung, *Annu. Rev. Chem. Biomol. Eng.* **2012**, *3*, 445.

[12] M. R. Palacin, *Chem. Soc. Rev.* **2009**, *38*, 2565.

[13] X. Su, Q. Wu, J. Li, X. Xiao, A. Lott, W. Lu, B. W. Sheldon, J. Wu, *Adv. Energy Mater.* **2014**, *4*, 1300882.

[14] Y. Idota, *Science* **1997**, *276*, 1395.

[15] J. Y. Huang, L. Zhong, C. M. Wang, J. P. Sullivan, W. Xu, L. Q. Zhang, S. X. Mao, N. S. Hudak, X. H. Liu, A. Subramanian, H. Fan, L. Qi, A. Kushima, J. Li, *Science* **2010**, *330*, 1515.

[16] K.-S. Park, A. Benayad, D.-J. Kang, S.-G. Doo, *J. Am. Chem. Soc.* **2008**, *130*, 14930.

[17] H.-G. Jung, M. W. Jang, J. Hassoun, Y.-K. Sun, B. Scrosati, *Nat Commun* **2011**, *2*, 516.

[18] Y. Q. Wang, L. Gu, Y. G. Guo, H. Li, X. Q. He, S. Tsukimoto, Y. Ikuhara, L. J. Wan, *J. Am. Chem. Soc.* **2012**, *134*, 7874.

[19] S.-T. Myung, N. Takahashi, S. Komaba, C. S. Yoon, Y.-K. Sun, K. Amine, H. Yashiro, *Adv. Funct. Mater.* **2011**, *21*, 3231.

[20] J. S. Chen, X. W. Lou, *Mater. Today* **2012**, *15*, 246.

[21] M. Zukalová, M. Kalbáč, L. Kavan, I. Exnar, M. Graetzel, *Chem. Mater.* **2005**, *17*, 1248.

[22] J. M. Tarascon, *Philos. Trans. R. Soc., A* **2010**, *368*, 3227.

[23] V. Etacheri, R. Marom, R. Elazari, G. Salitra, D. Aurbach, *Energy Environ. Sci.* **2011**, *4*, 3243.

[24] K. Xu, *Chem. Rev.* **2014**, *114*, 11503.

[25] H. Kim, M.-Y. Cho, M.-H. Kim, K.-Y. Park, H. Gwon, Y. Lee, K. C. Roh, K. Kang, *Adv. Energy Mater.* **2013**, *3*, 1500.

[26] V. Aravindan, J. Gnanaraj, Y.-S. Lee, S. Madhavi, *Chem. Rev.* **2014**, *114*, 11619.

[27] T. Brousse, R. Marchand, P.-L. Taberna, P. Simon, *J. Power Sources* **2006**, *158*, 571.

[28] A. G. Dylla, G. Henkelman, K. J. Stevenson, *Acc. Chem. Res.* **2013**, *46*, 1104.

[29] C. Jiang, M. Wei, Z. Qi, T. Kudo, I. Honma, H. Zhou, *J. Power Sources* **2007**, *166*, 239.

[30] Y. Ren, L. J. Hardwick, P. G. Bruce, *Angew. Chem. Int. Ed.* **2010**, *122*, 2624.

[31] A. R. Armstrong, G. Armstrong, J. Canales, P. G. Bruce, *J. Power Sources* **2005**, *146*, 501.

[32] A. R. Armstrong, G. Armstrong, J. Canales, R. García, P. G. Bruce, *Adv. Mater.* **2005**, *17*, 862.

[33] R. Marchand, L. Brohan, M. Tournoux, *Mater. Res. Bull.* **1980**, *15*, 1129.

[34] T. Kasuga, M. Hiramatsu, A. Hoson, T. Sekino, K. Niihara, *Langmuir* **1998**, *14*, 3160.

[35] D. V. Bavykin, J. M. Friedrich, F. C. Walsh, *Adv. Mater.* **2006**, *18*, 2807.

[36] T. P. Feist, P. K. Davies, *J. Solid State Chem.* **1992**, *101*, 275.

[37] G. Armstrong, A. R. Armstrong, P. G. Bruce, P. Reale, B. Scrosati, *Adv. Mater.* **2006**, *18*, 2597.

[38] G. Armstrong, A. R. Armstrong, J. Canales, P. G. Bruce, *Chem. Commun.* **2005**, 2454.

[39] G. Armstrong, A. R. Armstrong, J. s. Canales, P. G. Bruce, *Electrochem. Solid-State Lett.* **2006**, *9*, A139.

[40] S. Brutti, V. Gentili, H. Menard, B. Scrosati, P. G. Bruce, *Adv. Energy Mater.* **2012**, *2*, 322.

[41] Y. Ren, Z. Liu, F. Pourpoint, A. R. Armstrong, C. P. Grey, P. G. Bruce, *Angew. Chem. Int. Ed.* **2012**, *51*, 2164.

[42] Y. G. Andreev, P. M. Panchmatia, Z. Liu, S. C. Parker, M. S. Islam, P. G. Bruce, *J. Am. Chem. Soc.* **2014**, *136*, 6306.

[43] B. Zachau-Christiansen, K. West, T. Jacobsen, S. Atlung, *Solid State Ionics* **1988**, *28–30, Part 2*, 1176.

[44] Y. Harada, K. Hoshina, H. Inagaki, N. Takami, *Electrochim. Acta* **2013**, *112*, 310.

[45] M. Fehse, M. Ben Yahia, L. Monconduit, F. Lemoigno, M.-L. Doublet, F. Fischer, C. Tessier, L. Stievano, *J. Phys. Chem. C* **2014**, *118*, 27210.

[46] N. Takami, Y. Harada, T. Iwasaki, K. Hoshina, Y. Yoshida, *J. Power Sources* **2015**, *273*, 923.

[47] M. Fehse, E. Ventosa, *ChemPlusChem* **2015**, *80*, 785.

[48] H. Liu, Z. Bi, X. G. Sun, R. R. Unocic, M. P. Paranthaman, S. Dai, G. M. Brown, *Adv. Mater.* **2011**, *23*, 3450.

[49] S. Liu, H. Jia, L. Han, J. Wang, P. Gao, D. Xu, J. Yang, S. Che, *Adv. Mater.* **2012**, *24*, 3201.

[50] S. Liu, Z. Wang, C. Yu, H. B. Wu, G. Wang, Q. Dong, J. Qiu, A. Eychmuller, X. W. David Lou, *Adv. Mater.* **2013**, *25*, 3462.

[51] V. Etacheri, J. E. Yourey, B. M. Bartlett, *ACS Nano* **2014**, *8*, 1491.

[52] C. Chen, X. Hu, Y. Jiang, Z. Yang, P. Hu, Y. Huang, *Chem. - Eur. J.* **2014**, *20*, 1383.

[53] X. Yan, Y. Li, M. Li, Y. Jin, F. Du, G. Chen, Y. Wei, *J. Mater. Chem. A* **2015**, *3*, 4180.

[54] Y. Zhang, Q. Fu, Q. Xu, X. Yan, R. Zhang, Z. Guo, F. Du, Y. Wei, D. Zhang, G. Chen, *Nanoscale* **2015**, *7*, 12215.

[55] S. Goriparti, E. Miele, M. Prato, A. Scarpellini, S. Marras, S. Monaco, A. Toma, G. C. Messina, A. Alabastri, F. D. Angelis, L. Manna, C. Capiglia, R. P. Zaccaria, *ACS Appl. Mater. Interfaces* **2015**, *7*, 25139.

[56] C. Kim, R. Buonsanti, R. Yaylian, D. J. Milliron, J. Cabana, *Adv. Energy Mater.* **2013**, *3*, 1286.

# Chapter 3

# Experimental Methodology

*This chapter describes the principles underlying the synthesis/characterization techniques and the method of data analysis. First of all, the rationale for the selection of* $TiO_2$ *nanotube platform is elaborated. Secondly, the method for the synthesis of active materials is presented. Thirdly, the characterization techniques and working principles will be discussed. Lastly, special focus will be on the details of the electrochemical characterization techniques and the data collection method from the Solartron electrochemical work station.*

## 3.1 Rationale for Selection of Materials and Methods

### 3.1.1 Rationale for Selection of Nanotube Platforms

The hypothesis of the thesis is that the *in situ* formed conductive pathways of lithiated anatase will improve the high rate performances of the $TiO_2$ (B) phase, whose working potential is below that of the anatase phase. To probe the lithiation-induced conductivity, electrochemical impedance spectroscopy (EIS) is commonly used because it could distinguish between electrical and ionic conduction. Since EIS technique measures the overall electrode response to external bias, proper electrode design is important for investigation of the materials. As shown in Figure 3.1a, conventional electrode is composed of active materials, polymeric binder and conductive carbon, owing to the shielding effect of highly conductive carbon additives, the overall conductivity remains high throughout the reaction, which fails to manifest the change of conductivity in active materials. Therefore, eliminating the conductive carbon is essential for such study as illustrated in Figure 3.1b. However, the volume expansion (~ 4 % for $TiO_2$) upon lithiation could lead to loss of inter-particle contacts after de-lithiation with repeated cycling. The changes in local particle conductivity cannot be accurately reflected on the electrode scale, thus the materials should be able to accommodate the volume change and maintain contacts throughout reaction. Previously our group has developed a novel stirring hydrothermal technology to produce ultralong high aspect-ratio $TiO_2$ nanotubes electrode,[1, 2] which serves as great platform (Figure 3.1c) to probe the conductivity change during the lithiation process benefited from following merits: firstly, the 3D cross-linked nanotubular networks promote interactions of the suspended nanotubes in ethanol solution, thus enabling fabrication of additive-free electrode to eliminate the side effect of binders and conductive agents, making the system more reliable for EIS study. Secondly, the long range interconnected nanotubes helps to ensure intimate interfacial contacts among nanotubes and the hollow space can buffer volumetric expansion upon cycling to maintain such contacts. Thirdly, the phase of the $TiO_2$ materials can be tailored easily via different annealing temperature [3, 4] based on the same precursor hydrogen titanate nanotube, make it possible for systematic study of the phase effect on performances. The additive-free $TiO_2$ nanotube electrode is used throughout this thesis for both half-cell and full-cell lithium-ion based EES devices.

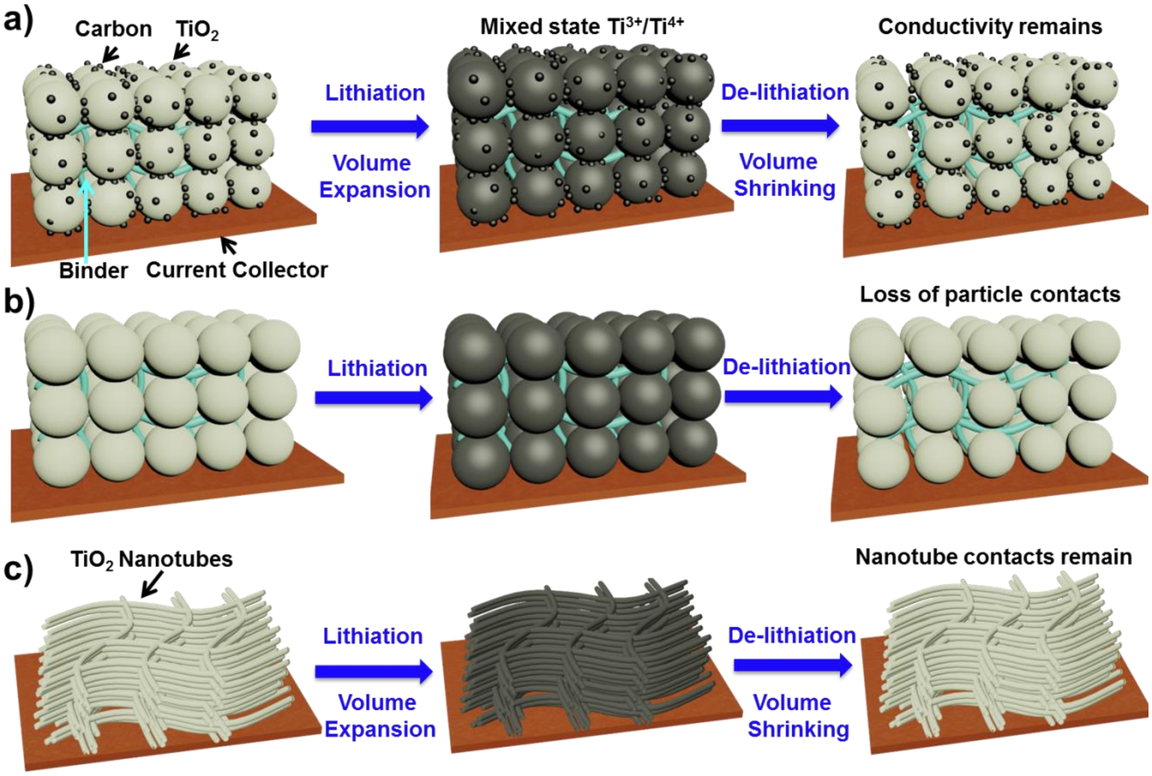

**Figure 3.1** Schematic on the change of electrode during charge-discharge process: (a) Conventional electrode with conductive carbon, the overall conductivity remains high during lithiation reaction; (b) Electrode without conductive carbon, the volumetric expansion during lithiation process will result in loss of inter-particle contacts after de-lithiation, therefore the change of conductivity in local particles cannot be accurately reflected on electrode scale. (c) Additive-free nanotube electrode, the hollow space can buffer the volumetric change and the long range cross-linked structure helps to ensure intimate contacts of the nanotubes, thus the change of local nanotube conductivity is accurately reflected on electrode scale.

### 3.1.2 Rationale for Heat Treatment Method

The additive-free $TiO_2$ nanotube-based electrode is essential to investigate the change of the electrical and ionic conductivity inside the active materials via the *in situ* EIS technique. In order to fabricate the additive-free electrode, highly viscous solution is required. In our previous study, the viscosity of the pristine hydrogen titanate nanotubes obtained from stirring hydrothermal method (Figure 3.2a) dispersed in ethanol solution are given by:[1]

$$\eta_0 \propto (L/D)^2 \tag{3.1}$$

*Where* $L$ and $D$ refer to the length and diameter of the nanotubes, respectively. The ratio of length and diameter is termed as aspect ratio. In order to obtain the additive-free $TiO_2$ electrode on copper current collector, the heat treatment process shall preserve the nanotubular morphology and prevent oxidation of copper. During phase transformations, violent structure changes are expected, any gaseous environment is likely to destroy the nanotubular structure, and therefore the heat treatment process is done in the vacuum furnace with vacuum level of $10^{-5}$ mbar (Figure 3.2b). With such vacuum annealing process, the phase contents of anatase and $TiO_2$ (B) can be conveniently controlled via different annealing temperature and the resulting additive-free $TiO_2$ nanotube electrodes can be fabricated as shown in Figure 3.2c.

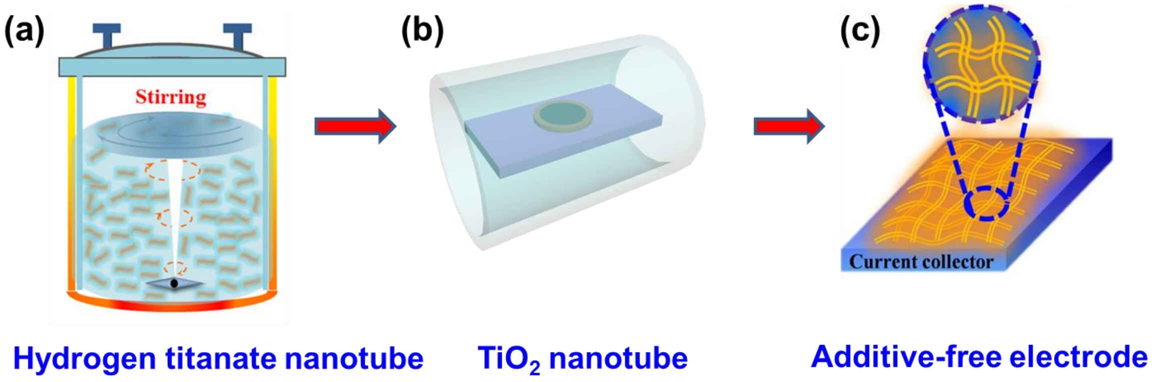

**Figure 3.2** Experiment procedures for the synthesis of $TiO_2$ nanotubes with different phase contents: (a) the pristine hydrogen titanate nanotubes obtained by stirring hydrothermal method; (b) vacuum annealing of the hydrogen titanate nanotube to obtain $TiO_2$ nanotubes, the phase composition can be tailored via the annealing temperature; (c) the final additive-free electrode on copper current collector.

## 3.2 Characterization Techniques

Various characterization techniques were employed in order to probe the electrode materials properties, the major techniques employed are discussed in following section.

### 3.2.1 Electron Microscopy

The $TiO_2$ nanotubes feature small size in the radial direction, the diameter is typically in the range of 1-100 nm, which is beyond the resolution limit of conventional optical microscope, therefore electron microscopy (EM) is required to probe the morphology of the samples. In current study, two commonly used EM are used for the morphology study: namely scanning electron microscopy (SEM) and transmission electron microscopy (TEM).

Scanning electron microscopy (SEM) is commonly used to probe the surface morphology of the materials in nanometer range. The nanotubes surface morphology can be obtained via the secondary electron imaging mode, where the topography of the surface features influence the local variation of electron density.

Transmission electron microscopy (TEM) can provide the structural information of the materials (e.g nanotubes, nanoparticles) and evaluate the tube thickness and diameters. In addition, it can provide high resolution (HRTEM) imaging where the different lattice distance and angles will be dissolved to map the different crystal phases.

### 3.2.2 Powder X-ray Diffraction

Powder X-ray diffraction (XRD) technique is commonly used to determine the crystal structure of materials. When the incident X-ray interacts with the host materials, depending on the crystal structure, peaks will appear on the spectra obtained reflecting the lattice parameters. In current study, XRD is used to determine the presence of anatase and $TiO_2$ (B) phase upon different annealing temperature.

### 3.2.3 Electrochemical Techniques

The electrochemical performances of the cells are evaluated by various electrochemical techniques, including galvanic discharging/charging, cyclic voltammetry (CV), and electrochemical impedance spectroscopy (EIS).

Galvanic cycling performances of the batteries and capacitors can be evaluated by the galvanic discharging/charging test at particular current rates. Information obtained from such test includes:

(a) Capacity: capacity is defined as the total amount of charges the electrode materials are able to store. In the galvanic cycling experiment, the current is usually fixed at constant value; therefore the capacity can be calculated by multiplying the current with the total time. Specific capacity can be obtained by normalizing with the actual mass of the active electrode material; the specific capacity is an intrinsic property of the active materials and serves as performance indicator. The galvanic cells may be cycled at different current rates; a rate of *n* C corresponds to full discharge in 1/*n* h. Since the theoretical specific capacity of $TiO_2$ materials is 335 mAh $g^{-1}$, therefore 1 C = 335 mA $g^{-1}$, which corresponds to full discharge in 1 hour.

(b) Voltage profile: the voltage profile as a function of capacity gives useful information on the actual operation window of the electrode materials and provides indication on the polarization with respect to different current densities. The energy density (ED) of the system is given by:[5]

$$ED = E \times Q \tag{3.2}$$

$$E = -\frac{\Delta G}{nF} \tag{3.3}$$

$$Q = \frac{nF}{3.6M_w} \tag{3.4}$$

Where $E$ is the electromotive force (potential or voltage is commonly used in electrochemical cells), and $Q$ is the gravimetric specific capacity (mAh $g^{-1}$), $\Delta G$ is the Gibbs free energy change, $n$ is the total number of electrons involved in reaction, $F$ is Faraday constant and $M_w$ is the molecular weight of the materials. By integration of the voltage profile over capacity, the specific energy of the electrochemical cells can be obtained.

(c) Differential capacity: dQ/dV is the derivative of the specific capacity versus voltage curve, which indicates the amount of charge added or removed with respect to the cell voltage, with the loop of the curve showing one charge-discharge cycle.[6] The peak value of such plot indicates excessive storage of lithium ions reflecting the redox reaction potential. [7, 8]

Compared to galvanic cycling test, cyclic voltammetry (CV) is more accurate method in determining the electrochemical properties of the active materials. During CV test, the applied voltage increases linearly at specific scan rate, and the corresponding current value is recorded and plotted against the voltage.[9] The CV technique is very useful in determining the redox potential of the active materials, since different materials or even different polymorphs of same material exhibit different redox potential towards lithium; therefore, the CV technique can be used to differentiate $TiO_2$ materials with different phases.

Electrochemical impedance spectroscopy (EIS) is used to study the reaction kinetics of $TiO_2$ materials. In particular, the charge transfer resistance and the chemical diffusion coefficient[10] can be obtained from EIS at different reaction potential for the systematically study of the lithiation-induced conductivity change in $TiO_2$ nanotubes.

## 3.3 Principles behind Characterization Techniques

### 3.3.1 Scanning Electron Microscopy (SEM)

The SEM is used to probe surface topography of materials with resolution beyond the limit of conventional microscope.[11] Resolution is defined as the smallest distance at which two objects can be distinguished as individual ones, according to Abbes's equation, the minimum resolvable distance *d* is calculated by:

$$d = \frac{0.61\lambda}{NA} \tag{3.5}$$

Where $\lambda$ is the wavelength of energy source and NA refers to numerical aperture, which is a constant given the setup of the microscope. The large wavelength of visible light (~ 400 nm) hinders the resolution of optical microscope. For the electrons under certain accelerating voltage, the wavelength is given by:

$$\lambda = \frac{h}{\sqrt{2meV}} \tag{3.6}$$

Where *h* is the Planck's constant, *m* is electron mass, *e* is electron charge, under accelerating of 5 kV, and the wavelength of the electron is around 0.173 Å, yielding much smaller *d* value than conventional optical microscope, therefore providing resolution in nanometer range for imaging of nanomaterials.

When the electron beams interact with the specimen, there will be elastic scattering events and inelastic scattering events (Figure 3.3). In elastic interactions, only the trajectories of the electron beam is affected by the atom while the kinetic energy remains the same, if such electrons deflected back out of the specimen, then it is termed as backscattered electrons. As for the inelastic scattering event, the energy from the incident electrons will be transferred to the atoms of specimen, which will lead to a potential expulsion of an electron from that atom as secondary electrons. The topography of the surface features affects the number of secondary electrons reaching the detector; therefore the local variation of the electron density can be used to reveal the surface morphology.

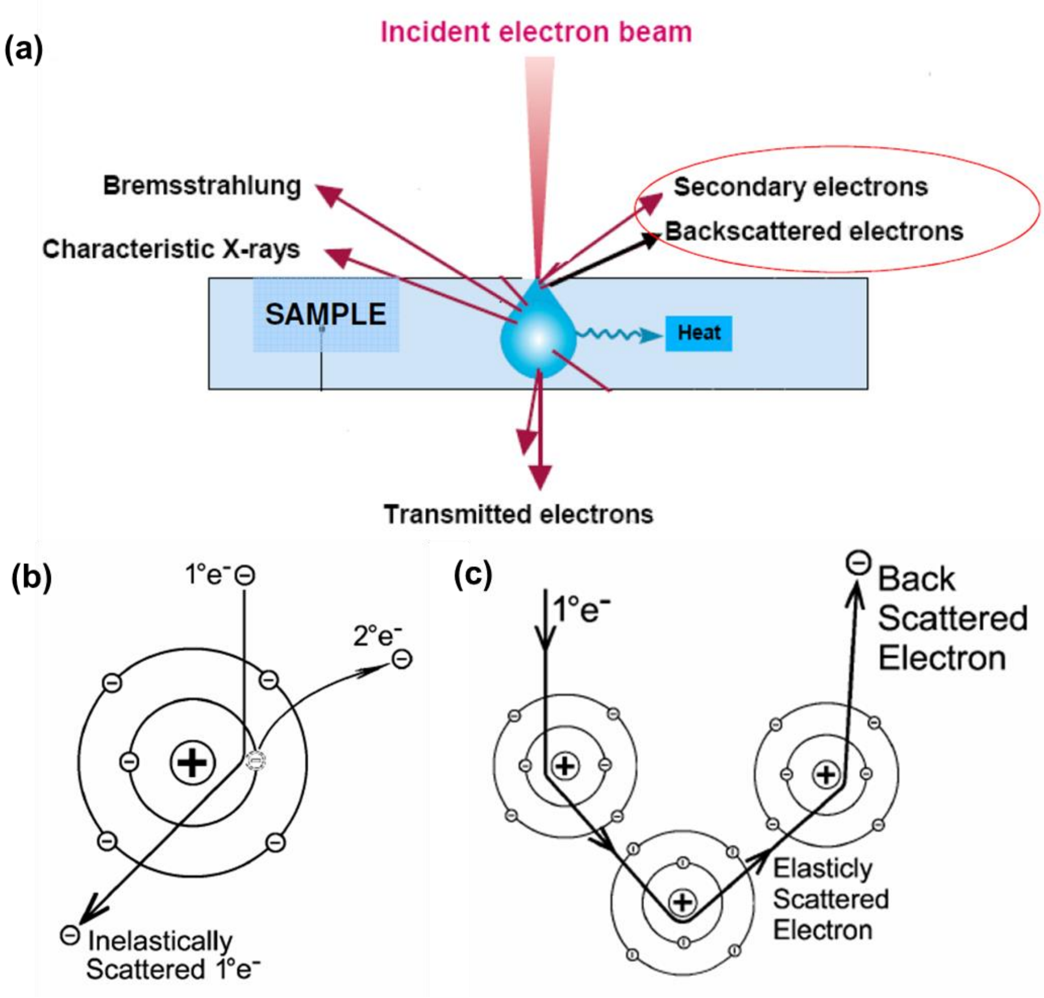

**Figure 3.3** Interaction of electron beam with specimen: (a) the general interaction scheme, (b) production of secondary electrons (c) production of back scattered electrons.

In current study, the secondary electrons are collected by the detector to get the topography information of the $TiO_2$ materials. In particular, the surface morphology of additive-free $TiO_2$ nanotubes are probed and analyzed with SEM.

### 3.3.2 Transmission Electron Microscopy (TEM)

Similarly to SEM**,** TEM uses even higher accelerating voltages to produce even smaller electron wavelength to get higher resolution.[12] There are different modes in terms of operation, such as the imaging mode and the diffraction mode (Figure 3.4). In the imaging mode, bright field images are generated by the transmitted beam with small objective aperture; while dark field image is formed when the aperture is placed around diffracted beam. The diffraction mode is obtained by removing the objective aperture and inserts the selected area diffraction (SAD) aperture, giving the diffraction pattern of the materials with diffracted beams.

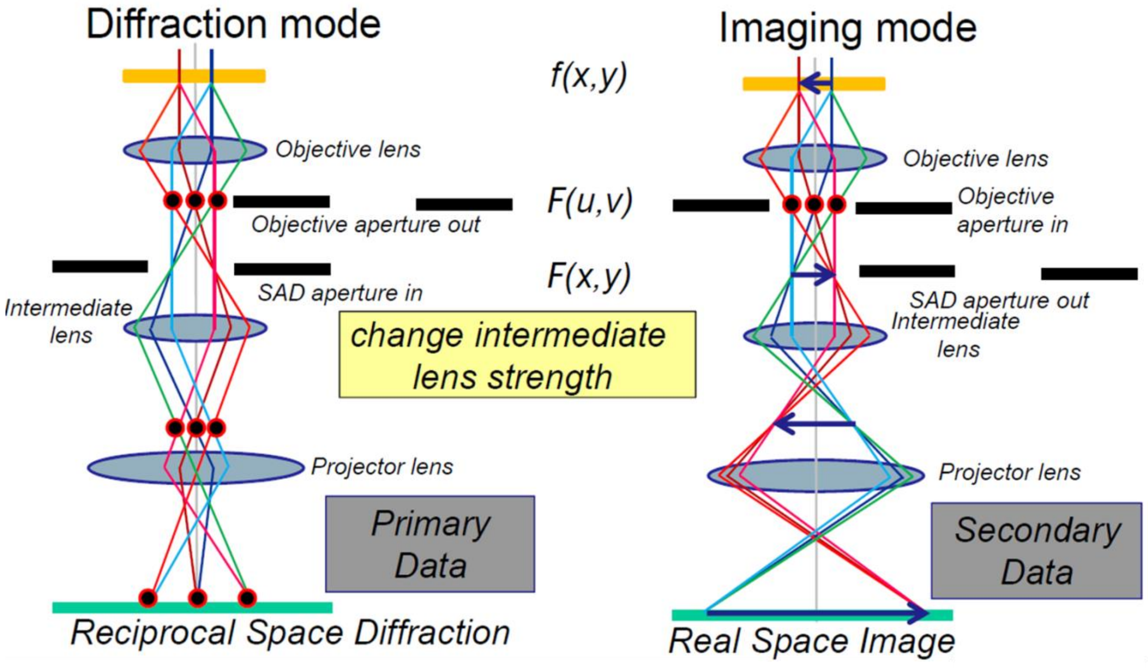

**Figure 3.4** Schematics on the diffraction and imaging modes of transmission electron microscope.

High resolution images (HRTEM) is obtained by using a large objective aperture to select many beams, inducing both transmitted and diffracted beams and reconstructed to yield contrast related to atomic structure of materials. In the HRTEM mode, both the images and diffraction patterns can be obtained in order to determine the crystal lattice spaces and phases. In current study, the nanotubular nature of $TiO_2$ materials are confirmed by TEM images and the HRTEM images are collected to study lattice distance and crystal phases.

### 3.3.3 Powder X-ray Diffraction

X-rays are classified as electromagnetic waves with wavelength in the range of 0.1 nm to 10 nm, which fall in the similar range as that of the interatomic spacing in materials. Therefore powder X-ray diffraction (XRD) technique is widely used to determine the crystal structure and lattice information of the materials. As shown in Figure 3.5, in materials with crystallinity, periodical regular arrangement of atoms with a constant spacing will cause the diffraction of the incident beams and the reflected beams with constructive patterns are described by Bragg's law:

$$2d\sin\theta = n\lambda \tag{3.7}$$

Where $d$ is the distance of crystal planes and $\lambda$ is the wavelength of incident X-ray source. With this equation, any constructive patterns at certain diffraction angle $\theta$ are reflected as diffraction peaks and can be used to calculate the crystal lattice plane distance.

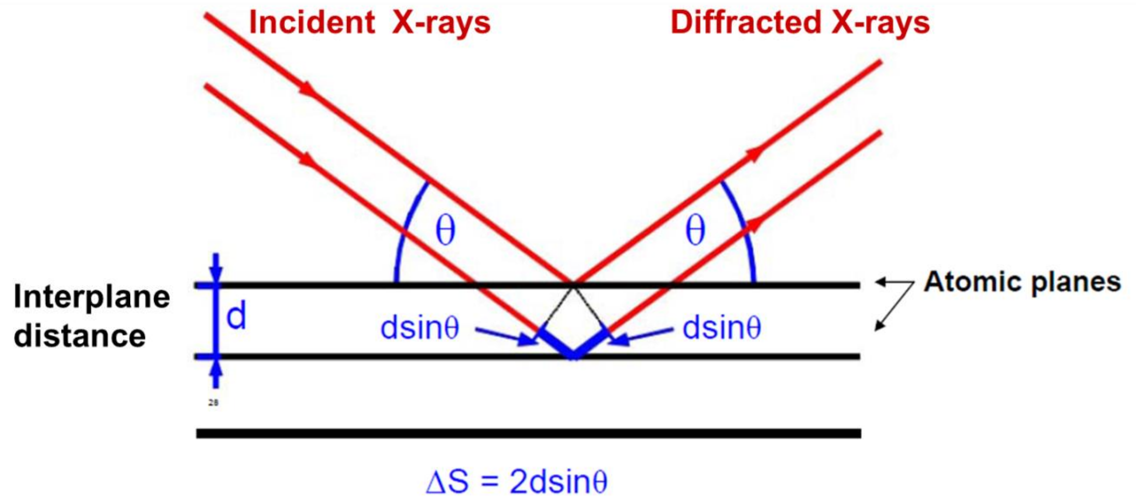

**Figure 3.5** Schematics showing the Bragg's diffraction model in the crystal plane.

In the powder XRD setup, θ-2θ configuration is adopted. The operation scheme is shown in figure 3.6 below. Briefly, the incident X-rays produced inside the X-ray tube will pass through the primary optics to minimize the divergence. After interaction with the specimen, the reflected X-rays pass through secondary optics to reduce air scattering and divergence and finally collected by the detector. In real measurement, the X-ray tube is fixed, while the samples are rotated by an angle θ, the detector needs to move simultaneously with an angle of 2θ to collect the diffracted beams. Therefore, in the powder XRD patterns obtained, the x-axis is usually 2θ.

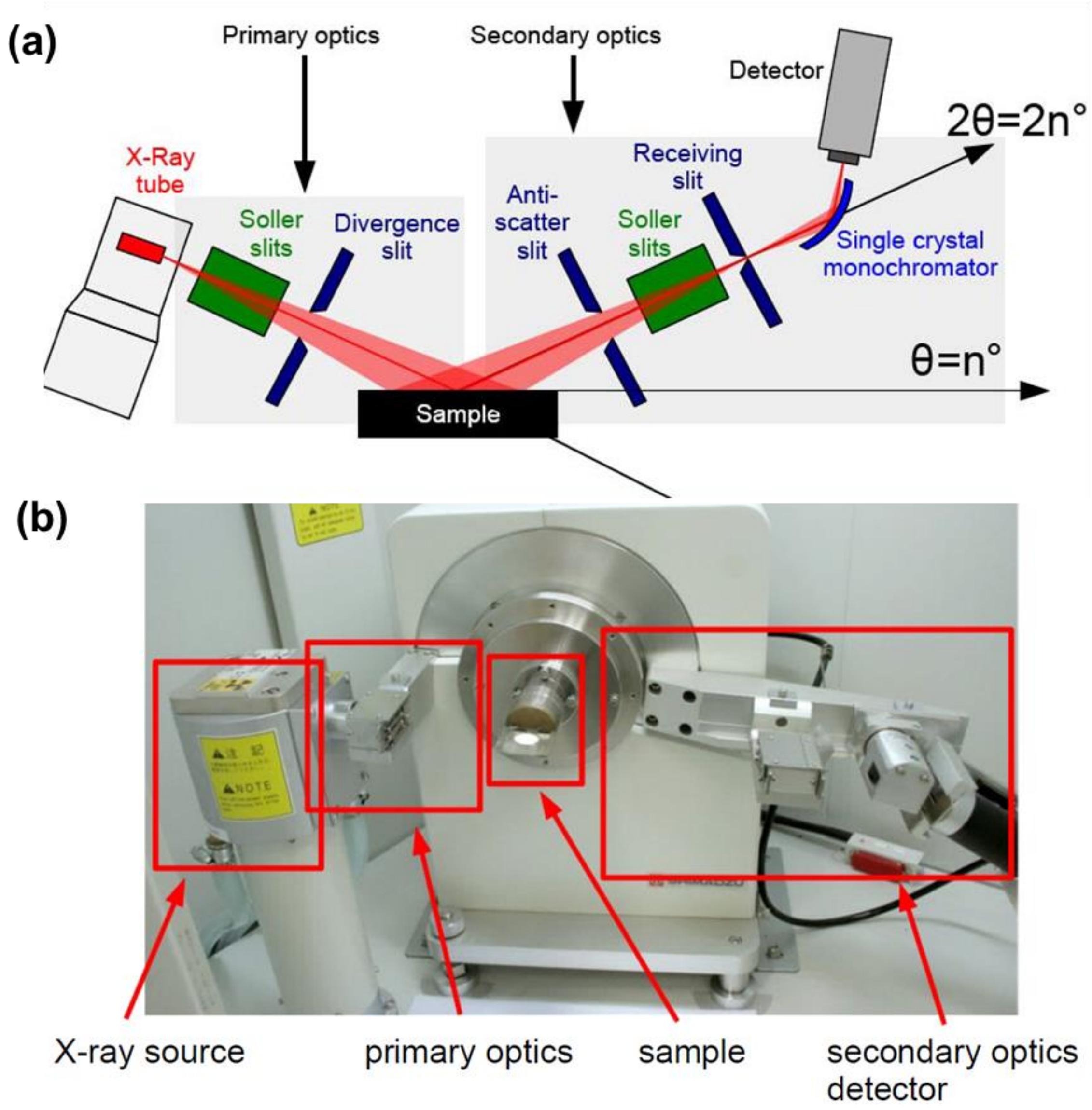

**Figure 3.6** Powder XRD setup: (a) schematics showing the setup of different components inside the apparatus; (b) the actual components inside the system.

### 3.3.4 Cyclic Voltammetry

Cyclic voltammetry (CV) are commonly used potential sweep techniques to probe the electrochemical reaction kinetics. In normal CV experiment (Figure 3.7), potential is swept linearly at scan rate of υ (V/s), so that the potential at any time (*t*) is given by:

$$E_t = E_i + \upsilon t \tag{3.8}$$

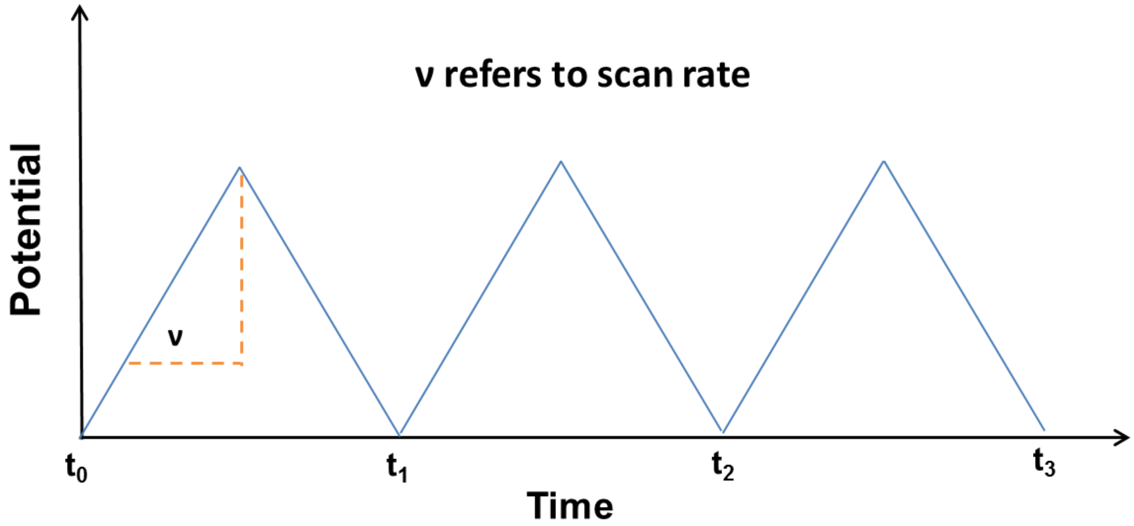

**Figure 3.7** Schematics showing the linear relationship of sweep potential with time during the CV scan.

When the potential value reaches the pre-determined maximum, it is ramped in the opposite direction to return to its original value. In this process, both oxidation and reduction potential of the active species can be determined.[13] There are three basic parameters that are important in CV; the following section will discuss them in detail.

(a) Peak location: if the electrode product is stable over the time scale of interest during potential scan, the formal redox potential of the redox couple is determined by averaging the two peak potentials:

$$E^0 = \frac{E_{pa} + E_{pc}}{2} \tag{3.9}$$

The peak separation $\Delta E_p$ is a diagnostic parameter of the Nernstian reaction, in a fully reversible system, there is no shift of the peak voltage, and therefore the separation is constant at different scan rates. The separation between the peaks potential at ambient temperature (25 °C) is given by:

$$\Delta E_p = 2.3RT / nF = 0.059 / n \tag{3.10}$$

Deviation of it as a function of the scan rates indicated that the irreversibility of the system. For quasi-reversible and irreversible system, the peak separation is larger than 0.059/$n$ V.

(b) Peak current ratio: if the electrochemical system is stable and reversible in the potential scan period, then the peak current ratio is equal to unity,

$$\frac{i_{pa}}{i_{pc}} = 1.0 \tag{3.11}$$

For reversible and quasi-reversible system, this value is equal to 1. Deviation of the value from unity indicates an irreversible system. The measurement of peak current can be complicated due to the difficulty in obtaining the proper "baseline" from which the magnitude of the peak current is defined. Under single peak condition, the baseline is generally obtained by extrapolating the zero current portions, or switching potential, as shown in Figure 3.8a. In complex systems where the baseline is difficult to locate, then ratio can be calculated by from the uncorrected anodic peak current $(i_{pa})_0$ with respect to zero current baselines and the current $i_\lambda$ (Figure 3.8b), as suggested by Nicholson:

$$\frac{i_{pa}}{i_{pc}} = \frac{(i_{pa})_0}{i_{pc}} + \frac{0.485(i_\lambda)}{i_{pc}} + 0.086 \tag{3.12}$$

Due to the uncertainty in peak current correction, in general, CV is not ideal for quantitative evaluation of properties that comes from the peak current height.

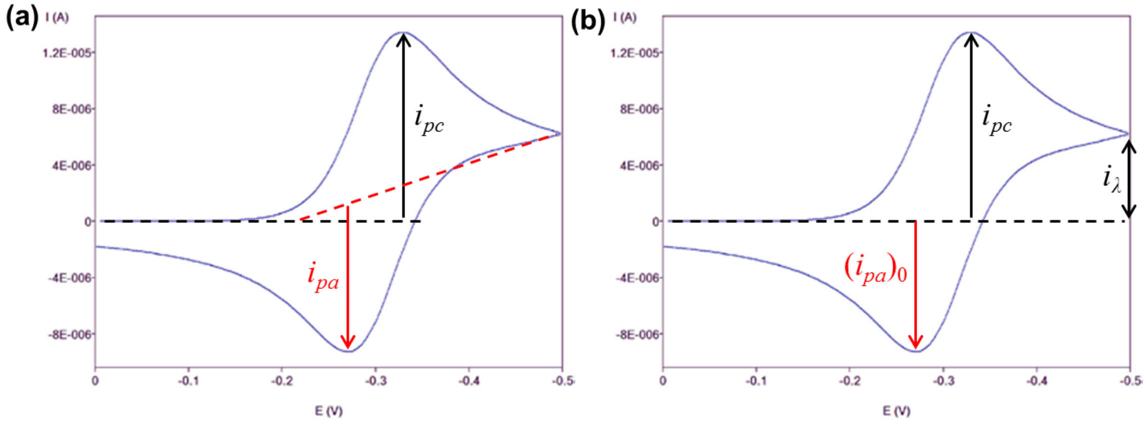

**Figure 3.8** Methods to determine the peak current in different CV curves: (a) baseline is easy to locate; (b) baseline is difficult to locate.

(c) Scan rate dependence of peak current: Assuming that electron transfer is rapid at the electrode surface, so that the system is diffusion controlled, the current can be obtained by the following expression:

$$i = nFAC^{*}(\pi D\sigma)^{1/2}\chi(\sigma t) \tag{3.13}$$

Where $\sigma = (nF / RT)\upsilon$, $n$ is the number of electrons involved in the reaction, $F$ is Faraday constant, $A$ is the surface area of electrode materials, $C^{*}$ is the concentration of redox species on electrode surface, $D$ refers to the chemical diffusion coefficient, $R$ is the ideal gas constant, $T$ is absolute temperature, and the scan rate is represented as $\nu$. At any given time, the factor $\chi(\sigma t)$ is a pure number, representing the normalized current. Therefore, the current $i$ vary linearly with the square root of the scan rate. For a reversible system, the function parameter $\pi^{1/2}\chi(\sigma t)$ reaches a maximum value of 0.4463, so the peak current is given by the formula below:

$$i_p = (2.69\times10^{5})n^{3/2}AC_o^{*}\upsilon^{1/2}D_o^{1/2} \tag{3.14}$$

If the system is dominated by the surface redox process, then diffusion is no longer the rate determining factor, in this case, the current should vary linearly with the scan rate according to:

$$i = \nu C_d A \tag{3.15}$$

Where $C_d$ refers to the capacitance of the material. Such system is usually observed in electrochemical double layer capacitors and pseudocapacitors.

When the electrochemical system involves both diffusion and surface reaction controlled mechanism, according to the work by Bruce Dunn, [14, 15] the relationship of current with scan rate is given by:

$$i = a\nu^{b} \tag{3.16}$$

Where $a$ and $b$ are the free variables. Plot such equation in logarithm scale leads to:

$$\log(i) = \log(a) + b\log(\nu) \tag{3.17}$$

The slope of such curve corresponds to b-value. A b-value equals to 0.5 indicates diffusion controlled system and b = 1 corresponds to surface controlled charge transfer controlled system. In general, mixed controlled systems are usually obtained with b value ranging from 0.5 to 1.0.

### 3.3.5 Electrochemical Impedance Spectroscopy

In an ideal resistor based electrical circuit, the resistance is a measure of the ability of resistor to resist the flow of current (movement of electrons). However in most real application system, the circuit is more complex that involves the motion of both electrons and changed ions. Impedance is a measure of the ability of circuit to resist the flow of electric current. In an electrochemical system, the impedance is affected by many factors, including the solution resistance, charge transfer resistance at electrode surface and ion diffusion. One approach to probe the impedance is through electrochemical impedance spectroscopy (EIS). During the EIS measurement, a small sinusoidal potential is applied to the cell and the response is recorded at each frequency. In such system, similar to Ohm's law, impedance is calculated by the following equation:

$$Z_\omega = \frac{E_\omega}{I_\omega} \tag{3.18}$$

Where $E_\omega$ and $I_\omega$ are frequency-dependent potential and current, respectively. EIS is theoretically much complex system, it is able to distinguish multiple electrochemical reactions takes place inside the cell, identify diffusion-limited reactions, like diffusion through a passivating film, and provide the electron transfer rate of the reaction, termed charge transfer resistance ($R_{ct}$).

In real setup, the excitation signal is a pure sinusoidal voltage, which can be expressed as

$$E_t = E_0 \sin(\omega t) \tag{3.19}$$

$E_t$ is the potential at time t, and $E_0$ is the amplitude of the signal. The amplitude is usually between 5-10 mV to ensure that the linear response of the current with respect to applied voltage is maintained. $\omega$ is the radial frequency (rad/s), it can be calculated from the frequency (expressed in Hz)

$$\omega = 2\pi f \tag{3.20}$$

As shown in Figure 3.9a, the response signal $I_t$ is still a sinusoidal curve but with phase shift $\phi$,

$$I_t = I_0 \sin(\omega t + \phi) \tag{3.21}$$

Since the impedance is defined as the ratio of time dependent potential and the current, so the expression analogous to Ohm's law gives us:

$$Z_{\omega} = \frac{E_t}{I_t} = \frac{E_0 \sin(\omega t)}{I_0 \sin(\omega t + \phi)} = Z_0 \frac{\sin(\omega t)}{\sin(\omega t + \phi)} \tag{3.22}$$

With Euler's formula, where potential and current are described in exponential form with an imaginary unit $j$, the impedance can be represented by a complex number:

$$Z_{\omega} = \frac{E_t}{I_t} = Z_0 \exp(j\phi) = Z_0(\cos\phi + j\sin\phi) \tag{3.23}$$

Such system is presented in the Nyquist plot (Figure 3.9b), where the real parts and imaginary parts are plotted as the x-axis and y-axis. For a pure resistance, the phase angle $\phi$ is 0 and for pure capacitance $\phi$ is π/2.

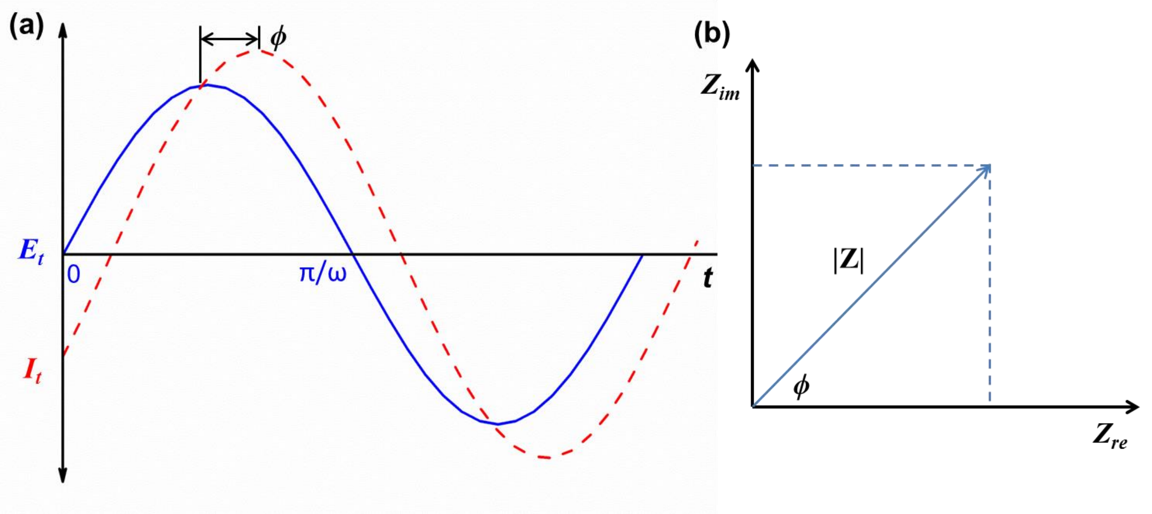

**Figure 3.9** (a) Schematics showing the change of current with respect to the applied sinusoidal potential in EIS measurement; (b) a typical Nyquist plot setup.

There are two important parameters which can be obtained from the EIS measurement, including the charge transfer resistance ($R_{ct}$), manifesting mainly the electrical conductivity, and the chemical diffusion coefficient, indicating the diffusion kinetics of active reaction species.

(a) Charge transfer resistance ($R_{ct}$), in a simple redox reaction, the relation between potential and current is given by: [16]

$$i = i_0 \left[ \frac{C_o}{C_o^*} \exp(\frac{\alpha n F \eta}{RT}) - \frac{C_R}{C_R^*} \exp(\frac{-(1-\alpha) n F \eta}{RT}) \right] \tag{3.24}$$

Where $i_0$ is the exchange current density, $C_o$ and $C_o^*$ is the concentration of oxidant at electrode surface and in the bulk, $C_R$ and $C_R^*$ is the concentration of reductants at electrode surface and in the bulk. α is the transfer coefficient of the reaction, η is overpotential, *F* is Faraday constant, *R* is ideal gas constant, *T* is temperature, and *n* is number of electrons involved in reaction.

In cases where diffusion layer thickness and the concentration polarization is minimized, the equation can be simplified, because the concentration in the electrode surface is the same as that in the bulk, $C_o^* = C_o$ and $C_R^* = C_R$. Therefore

$$i = i_0 \left[ \exp(\frac{\alpha nF\eta}{RT}) - \exp(\frac{-(1-\alpha)nF\eta}{RT}) \right] \tag{3.25}$$

This is the so-called Butler-Volmer equation, which is applicable when the polarization depends only on charge-transfer kinetics. When the overpotential η is sufficiently small and the electrochemical system stay at equilibrium condition, the above expression can be further simplified to:

$$R_{ct} = \frac{RT}{nFi_0} \tag{3.26}$$

The charge transfer resistance $R_{ct}$ is defined by the ratio of overpotential η and the current *i*. In this case, the exchange current density $i_0$ can be calculated based on the value of $R_{ct.}$ Smaller charge transfer resistance indicates large exchange current density and fast reaction kinetics.

(b) Chemical diffusion coefficient, at low frequency during the EIS measurement, the Warburg factor contributes to the overall diffusion by the following equation: [17, 18]

$$\sigma = \frac{RT}{\sqrt{2D_{Li}} n^2 F^2 SC} \tag{3.27}$$

Where σ denotes the Warburg coefficient, which can be calculated from the slope of the real part of the impedance (Z') versus ($\omega^{-1/2}$) (ω is angular frequency), *R* is ideal gas constant, *T* is absolute temperature, *F* is Faraday constant, *n* is the number of electrons involved in reaction, *C* is the concentration of active ions, *S* denoted the contact area between active materials and the electrolyte. The chemical diffusion coefficient $D_{Li}$ is a product of self-diffusion and thermodynamic factor: [19, 20]

$$D_{Li} = D_{Li(self)} \cdot \Phi \tag{3.28}$$

While self-diffusion is mainly related to the crystal structure of the materials, the thermodynamic factor Φ (also called Wagner factor) is a function of the concentration of mobile ions ($c_i$), concentration of the electronic species ($c_e$), transference number for electrons ($t_e$), and the charge valence number ($z_i$):

$$\Phi = t_e\left[1+z_i^2\left(\frac{c_i}{c_e}\right)\right] \tag{3.29}$$

The Wagner factor Φ represents an influence of electron motion on the mobile ions through the internal electrical field effect. During the electro-intercalation, the electrons move ahead of the mobile ions and generate an internal field to accelerate the motion of ions to maintain electroneutrality. Typically large thermodynamic factor can be obtained at sufficiently small electron concentrations and high electronic mobility, which is a situation commonly fulfilled by semiconductors.[21] For materials with metallic behavior, the value of Φ is close to unity.

To obtain both charge transfer resistance and chemical diffusion coefficient, the scheme for the Solartron system setup is illustrated in the figure 3.10 below:

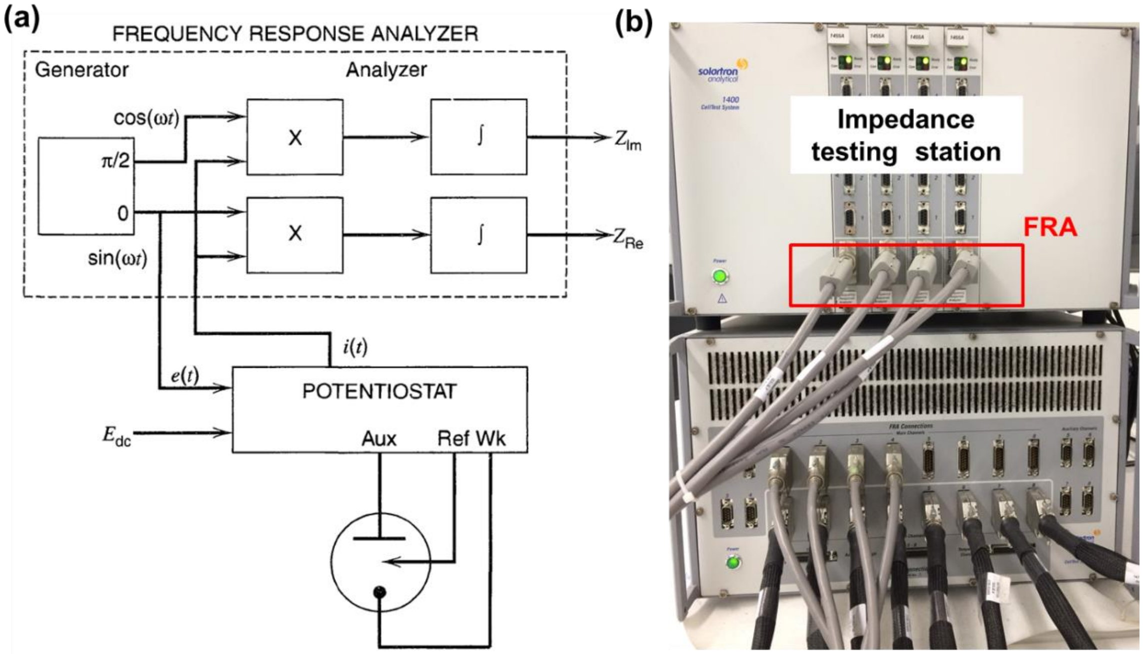

**Figure 3.10** Schematics of the Solartron electrochemical interface: (a) the draw out of the frequency response analyzer; (b) the actual impedance testing station. 2-terminal devcies is used in current study.

The impedance measurement in Solartron workstation is based on the frequency response analyzer (FRA), where the sinusoidal signal generated by the generator is fed to the potentiostat, which is added to the equilibrium DC voltage and fed to the cell. The resulting current is transformed into the analyzer, mixed with input signals and perform integration by the analyzer to yield a signal proportional to the real and imaginary part of the impedance (Or the equivalent magnitude and phase angle of the impedance), the frequency range for the analyzer can go from 10 μHz to 1 MHz.

From the raw data obtained by EIS measurement, post data analysis is required to get the charge transfer resistance. Such analysis is done with the ZView software provided by Solartron workstation. First of all, a reasonable circuit equivalent to the actual electrochemical system is needed for the fitting process, and then the initial parameters of the fitting model can be obtained by instant fit. Finally, the fitting process will run over the frequency range and the results are evaluated.

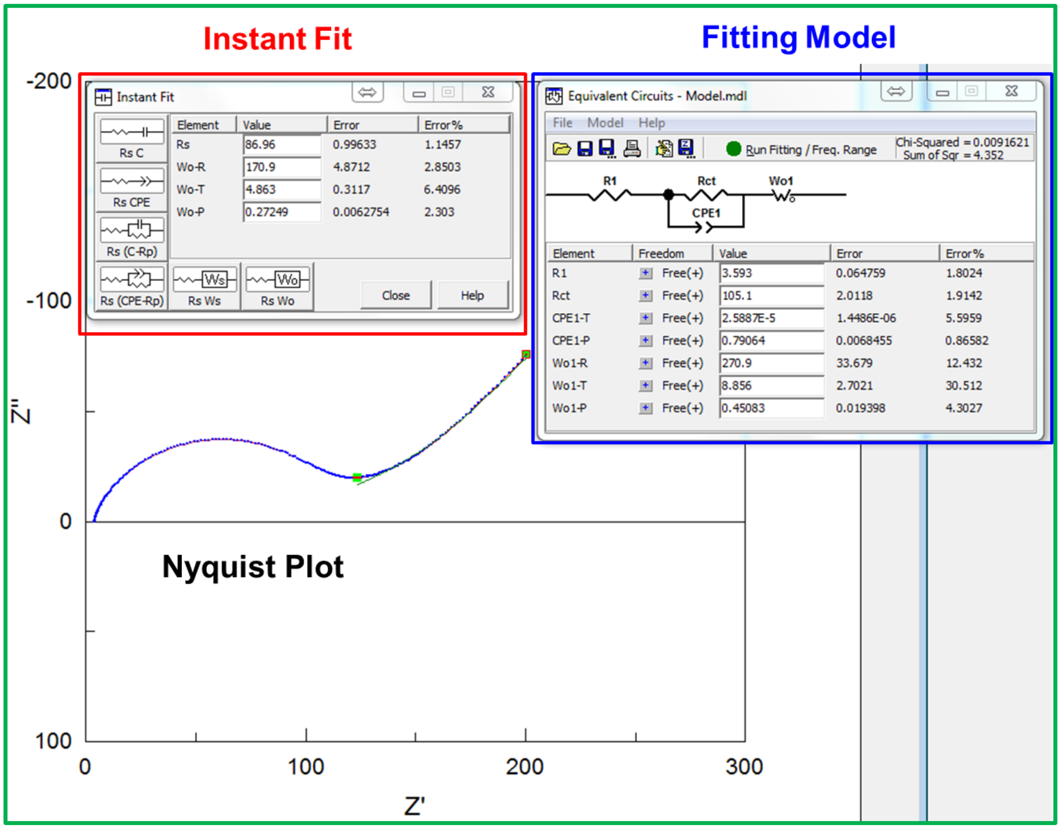

| Element | Value | Error | Error% |
|---|---|---|---|
| Rs | 86.96 | 0.99633 | 1.1457 |
| Wo-R | 170.9 | 4.8712 | 2.8503 |
| Wo-T | 4.863 | 0.3117 | 6.4096 |
| Wo-P | 0.27249 | 0.0062754 | 2.303 |

Chi-Squared = 0.0091621
Sum of Sqr = 4.352

| Element | Freedom | Value | Error | Error% |
|---|---|---|---|---|
| R1 | Free(+) | 3.593 | 0.064759 | 1.8024 |
| Rct | Free(+) | 105.1 | 2.0118 | 1.9142 |
| CPE1-T | Free(+) | 2.5887E-5 | 1.4486E-06 | 5.5959 |
| CPE1-P | Free(+) | 0.79064 | 0.0068455 | 0.86582 |
| Wo1-R | Free(+) | 270.9 | 33.679 | 12.432 |
| Wo1-T | Free(+) | 8.856 | 2.7021 | 30.512 |
| Wo1-P | Free(+) | 0.45083 | 0.019398 | 4.3027 |

**Figure 3.11** Fitting of impedance data based on appropriate fitting model for the electrochemical system.

In the *in situ* EIS measurement for $TiO_2$ nanotube electrodes during the lithiation process, the frequency range is $10^5$ Hz to 0.1 Hz, and the fitting model is the one used in Figure 3.11. The first parameter $R_1$ is the solution resistance, $R_{ct}$ is the charge transfer resistance, it is coupled with a constant phase elements (CPE), representing a non-ideal capacitor, and the diffusion at low frequency is represented by Warburg diffusion parameter.

## References

[1] Y. Tang, Y. Zhang, J. Deng, D. Qi, W. R. Leow, J. Wei, S. Yin, Z. Dong, R. Yazami, Z. Chen, X. Chen, *Angew. Chem. Int. Ed.* **2014**, *53*, 13488.

[2] Y. Tang, Y. Zhang, J. Deng, J. Wei, H. L. Tam, B. K. Chandran, Z. Dong, Z. Chen, X. Chen, *Adv. Mater.* **2014**, *26*, 6111.

[3] Y. Lei, J. Sun, H. Liu, X. Cheng, F. Chen, Z. Liu, *Nanoscale* **2014**, *6*, 14237.

[4] R. Wang, X. Xue, W. Lu, H. Liu, C. Lai, K. Xi, Y. Che, J. Liu, S. Guo, D. Yang, *Nanoscale* **2015**, *7*, 12833.

[5] K. Zhang, X. Han, Z. Hu, X. Zhang, Z. Tao, J. Chen, *Chem. Soc. Rev.* **2015**, *44*, 699.

[6] M. Dubarry, V. Svoboda, R. Hwu, B. Yann Liaw, *Electrochem. Solid-State Lett.* **2006**, *9*, A454.

[7] A. J. Smith, J. R. Dahn, *J. Electrochem. Soc.* **2012**, *159*, A290.

[8] X. Feng, J. Li, M. Ouyang, L. Lu, J. Li, X. He, *J. Power Sources* **2013**, *232*, 209.

[9] R. S. Nicholson, *Anal. Chem.* **1965**, *37*, 1351.

[10] M. Park, X. Zhang, M. Chung, G. B. Less, A. M. Sastry, *J. Power Sources* **2010**, *195*, 7904.

[11] J. Goldstein, D. E. Newbury, D. C. Joy, C. E. Lyman, P. Echlin, E. Lifshin, L. Sawyer, J. R. Michael, *Scanning Electron Microscopy and X-ray Microanalysis*, Springer US, New York 2003.

[12] C. B. C. David B. Williams, *Transmission Electron Microscopy*, Springer US, New York 2009.

[13] L. R. F. Allen J. Bard, *Electrochemical Methods: Fundamentals and Applications, 2nd Edition*, Wiley, New York 2001.

[14] V. Augustyn, J. Come, M. A. Lowe, J. W. Kim, P.-L. Taberna, S. H. Tolbert, H. D. Abruña, P. Simon, B. Dunn, *Nat Mater* **2013**, *12*, 518.

[15] V. Augustyn, P. Simon, B. Dunn, *Energy Environ. Sci.* **2014**, *7*, 1597.

[16] K. E. T.-A. John Newman, *Electrochemical Systems, 3rd Edition*, Wiley-Interscience, Hoboken, NJ 2004.

[17] N. Takami, A. Satoh, M. Hara, T. Ohsaki, *J. Electrochem. Soc.* **1995**, *142*, 371.

[18] J. Lu, C. Zhan, T. Wu, J. Wen, Y. Lei, A. J. Kropf, H. Wu, D. J. Miller, J. W. Elam, Y.-K. Sun, X. Qiu, K. Amine, *Nat Commun* **2014**, *5*.

[19] W. Weppner, R. A. Huggins, *J. Electrochem. Soc.* **1977**, *124*, 1569.

[20] Z. Li, F. Du, X. Bie, D. Zhang, Y. Cai, X. Cui, C. Wang, G. Chen, Y. Wei, *J. Phys. Chem. C* **2010**, *114*, 22751.

[21] L. A. Montoro, J. M. Rosolen, *Electrochim. Acta* **2004**, *49*, 3243.

# Chapter 4

# Dual Phase $TiO_2$ Nanotubes with High Lithiation-induced Conductivity for High Power Lithium-ion Batteries

*In this chapter, we demonstrated that conductivity of* $TiO_2$ *(B) can be enhanced by integrating with anatase and the dual phase* $TiO_2$ *nanotube electrodes exhibit much better performances at high current rates: a capacity of 131 mAh* $g^{-1}$ *after 10,000 cycles at 30 C and 124 mAh* $g^{-1}$ *after 5,000 cycles at 60 C is delivered for the optimized dual phase electrode. Even the mechanically mixed anatase particles and* $TiO_2$ *(B) nanotubes show superior rate performances than the pure phase* $TiO_2$ *(B) counterpart. Applying additive-free* $TiO_2$ *nanotube electrodes as the platform, we systematically studied the conduction behavior in these* $TiO_2$ *materials via in situ EIS technique and unravel that high-lithiation conductivity in dual phase electrodes resultant from lithiated anatase in early lithiation stage is accountable for the superior rate performances. Our present findings unravel the role of anatase phase in* $TiO_2$ *(B) structures and provide guidance for further research on* $TiO_2$ *materials for ultrafast charging LIBs. We envision that dual phase* $TiO_2$ *materials will play important roles for next-generation ultrafast charging and long lifetime LIBs and the lithiation-induced conductivity further paves a way for future exploration of potential applications in a broad field.*

## 4.1 Introduction

The development of ultrafast charging lithium-ion batteries (LIBs) with long lifetime is highly desirable in applications ranging from portable electronics, electric vehicles and grid scale energy storage systems.[1-5] $TiO_2$ (B) constitutes an attractive anode candidate for such applications owing to its merits such as low cost, long cycle life and fast lithium diffusion kinetics,[6-9] which arises from its open channel structure and intrinsic pseudocapacitive charge storage behavior.[10-12] Although these characteristics render $TiO_2$ (B) promising for high power applications, its intrinsically low electrical conductivity (~ $10^{-10}$ S $cm^{-1}$)[13] inhibits fast charging performances due to severe polarization effect.[14] To address this issue, various strategies have been employed to improve electron transport towards and within $TiO_2$ (B) structure, among which surface coating [15, 16] and bulk ionic doping[13, 17] appear to be the most efficient in boosting overall rate performances. However, these approaches involve complicated procedures with multiple steps assisted by inert gas annealing or photo illumination. In addition, the large amount of inactive carbon coatings and additives (> 15 wt %) reduces the overall energy densities significantly.[18, 19] Therefore, it is highly imperative to develop a simple approach which maximizes the total amount of active materials for the enhancement of electrical conductivity in $TiO_2$ (B).

To achieve such goal, active lithium storage materials with reaction window similar to that of $TiO_2$ (B) (1.0-3.0 V vs. $Li^+/Li$) should be targeted. Since the major lithiation reaction of $TiO_2$ (B) lies between 1.4-1.6 V,[20] the conductive additives can be formed *in situ*, providing higher electrical conductivity before the onset of massive lithium intercalation in $TiO_2$ (B). Taking these requirements into consideration, anatase $TiO_2$ serves as promising candidate. Firstly, its main working potential is around 1.75 V during lithiation,[21-23] which falls directly above that of $TiO_2$ (B). Secondly, although pristine anatase is a poor conductor, studies demonstrate that lithium intercalation into anatase structure improves its electrical conductivity significantly at voltage >1.8 V due to the formation of a highly conductive (57 S $cm^{-1}$) solid solution of lithium with tetragonal anatase.[24, 25] As the solid solution is formed at potential higher than 1.4-1.6 V during lithiation, we expect that the *in situ* formed conduction pathways could enhance electrical conductivity and boost the high rate capacities in $TiO_2$ (B), while still maintain relatively high energy densities at low rate. In addition, due to the metastable nature of $TiO_2$ (B) phase, the anatase phase can be easily formed in $TiO_2$ (B) materials synthesized via sol-gel or hydrothermal methods. These reasons strongly motivate us to design dual phase materials with both high electron conduction and fast lithium ion diffusion for ultrafast charging LIBs. However, in order to conclusively probe both electrical and ionic conduction behavior during the lithiation process, one needs to consider the additional influence stemming from auxiliary carbon additives and volumetric expansion in active materials (Detail illustration are shown in Figure 3.1).[26] To eliminate these factors, electrodes fabricated from ultrahigh aspect-ratio $TiO_2$ nanotubes [27] are utilized as a platform to enable intimate contact without the use of additives and accommodate volumetric expansion upon lithiation (~ 4%). In addition, the phase composition of $TiO_2$ nanotubes can be conveniently tailored via thermal treatment. These features are essential for systematic study of lithiation-induce conductivity in both pure phase $TiO_2$ (B) and dual phase $TiO_2$ electrodes.

## 4.2 Experimental Methods

### 4.2.1 Synthesis

The hydrogen titanate precursor was synthesized by stirring hydrothermal method followed by ion exchange. Briefly, sodium titanate was first synthesized in oil bath with stirring speed of 500 rpm as reported elsewhere.[28] Ion substitution of $Na^+$ by $H^+$ was done with $HNO_3$ solutions (0.1 M) under mild stirring. To achieve complete substitution, such process is repeated several times. The obtained hydrogen titanate (HTNT) suspension was then washed with deionized water to reach pH value around 4. To prepare the additive-free $TiO_2$ nanotube electrodes, the HTHT precursor were spray coated onto copper foil and annealed under vacuum ($10^{-5}$ mbar) at temperature ranging from 300 ℃ to 750 ℃ for 2 h with ramping speed of 3 ℃/min. The samples obtained at annealing temperature of 300 ℃, 400 ℃, 500 ℃, 600 ℃, 700 ℃ and 750 ℃ is denoted as $TiO_2$ (B), $A_{15}B_{85}$, $A_{22}B_{78}$, $A_{42}B_{58}$, $A_{78}B_{22}$ and anatase, respectively. In dual phase $TiO_2$

materials, A refers to anatase phase and B refers to $TiO_2$ (B), while the suffix represents the weight percentage of that phase. Commercial anatase particles (< 25 nm) were purchased from Sigma-Aldrich and used as received.

### 4.2.2 Characterization

The X-Ray diffraction (XRD) patterns were obtained by Rigaku SmartLab 9 kW X-ray diffractometer using a Cu Kα source. The morphologies of the as-synthesized nanotube samples were probed by field emission scanning electron microscope (FESEM, Carl Zeiss Supra 55) and transmission electron microscope (TEM, JEOL JEM-2100F). Surface area and nitrogen adsorption/desorption isotherms of the samples were measured at 77 K using Tristar apparatus from Micromeritics. The samples were degassed at 373 K for 6 h under vacuum before analysis.

### 4.2.3 Electrochemical Analysis

Electrochemical properties of $TiO_2$ materials were investigated using 2032 type coin cells assembled inside Ar-filled glove box. The $O_2$ and $H_2O$ contents are typically below 0.6 ppm. The working electrode is formulated with active $TiO_2$ materials only, without any other additives. The counter and reference electrode is lithium metal. The organic electrolyte with 1.0 M $LiPF_6$ dissolved in ethylene carbonate: diethyl carbonate (EC: DEC, 1:1 by weight) was purchased from Ferro Corp. Galvanic cycling test of the half cell batteries were performed with NEWARE battery analyzer. Cyclic voltammetry (CV) study were carried out on a Solartron electrochemical workstation over a potential range of 1-3 V. *In situ* EIS measurements during the discharging process were also conducted with the Solartron workstation; the cells are discharged at current rate of 0.3 C to desired voltage and then rest for 10 minutes before impedance measurement. During impedance measurement, a sinusoidal wave with amplitude of 10.0 mV was applied to the cell over the frequency range 100 kHz-0.1 Hz. The battery cells were stabilized after 100 discharge/charge cycles before the *in situ* EIS measurements were performed. The loading density of $TiO_2$ is around 0.2 mg $cm^{-2}$.

## 4.3 Principle Outcomes

### 4.3.1 Confirmation of Different $TiO_2$ Phases

The phase of the $TiO_2$ nanotubes is controlled via different annealing temperature. It is well known that $TiO_2$ (B) is metastable phase and will transform to the more stable anatase phase at temperature above 300 ℃.[29, 30] X-ray diffraction (XRD) data collected from different samples confirms the presence of different phases. As shown in Figure 4.1a, all peaks can be indexed to anatase and $TiO_2$ (B). The peak is broad for $TiO_2$ (B) obtained at low annealing temperature indicating its poor crystallinity. With higher annealing temperature, more anatase contents will be present and the crystallinity and peak intensity of the materials increases. However, the main diagnostic peaks of nanostructure $TiO_2$ (B) and anatase are overlapped: for instance, reflection at around 25° could be indexed as the (110) plane of $TiO_2$ (B) or (011) plane of the anatase phase. Similar case occurs for the (020) plane of $TiO_2$ (B) and (200) plane of anatase.[31] Therefore XRD data alone cannot exclude the presence of anatase in $TiO_2$ (B). To further confirm the phase purity of the $TiO_2$ (B) electrode, cyclic voltammograms (CV) and discharge/charge voltage profiles of $TiO_2$ (B) electrodes are shown in Figure 4.1b & 4.1c. Typically for $TiO_2$ (B) phase, there are two characteristic peak pairs (S-peaks) located at ~ 1.5-1.6 V versus $Li^+/Li$, corresponding to the lithiation/de-lithiation reaction into the open channels of the $TiO_2$ (B) structure. Whereas for anatase, a peak pair (A-peak) at ~ 1.75 V/1.90 V is observed during the electrochemical reaction (Figure 4.2).[32] From the CV curve at low scan rate of 0.1 mV $s^{-1}$, pure phase $TiO_2$ (B) was indeed obtained evidenced by the absence of features assignable to anatase. In addition, the discharge/charge voltage profiles further confirms the phase purity since no voltage plateau at 1.75 V is observed in $TiO_2$ (B) due to constant phase lithiation process. Whereas for dual phase samples, a voltage plateau at 1.75 V during discharge and 1.90 V during charge can be observed indicating two phase lithiation reaction process in anatase impurities. By a combined analysis of XRD pattern, electrochemical voltage profile and CV curve, the pure phase $TiO_2$ (B) and dual phase $TiO_2$ with anatase can be clearly distinguished.

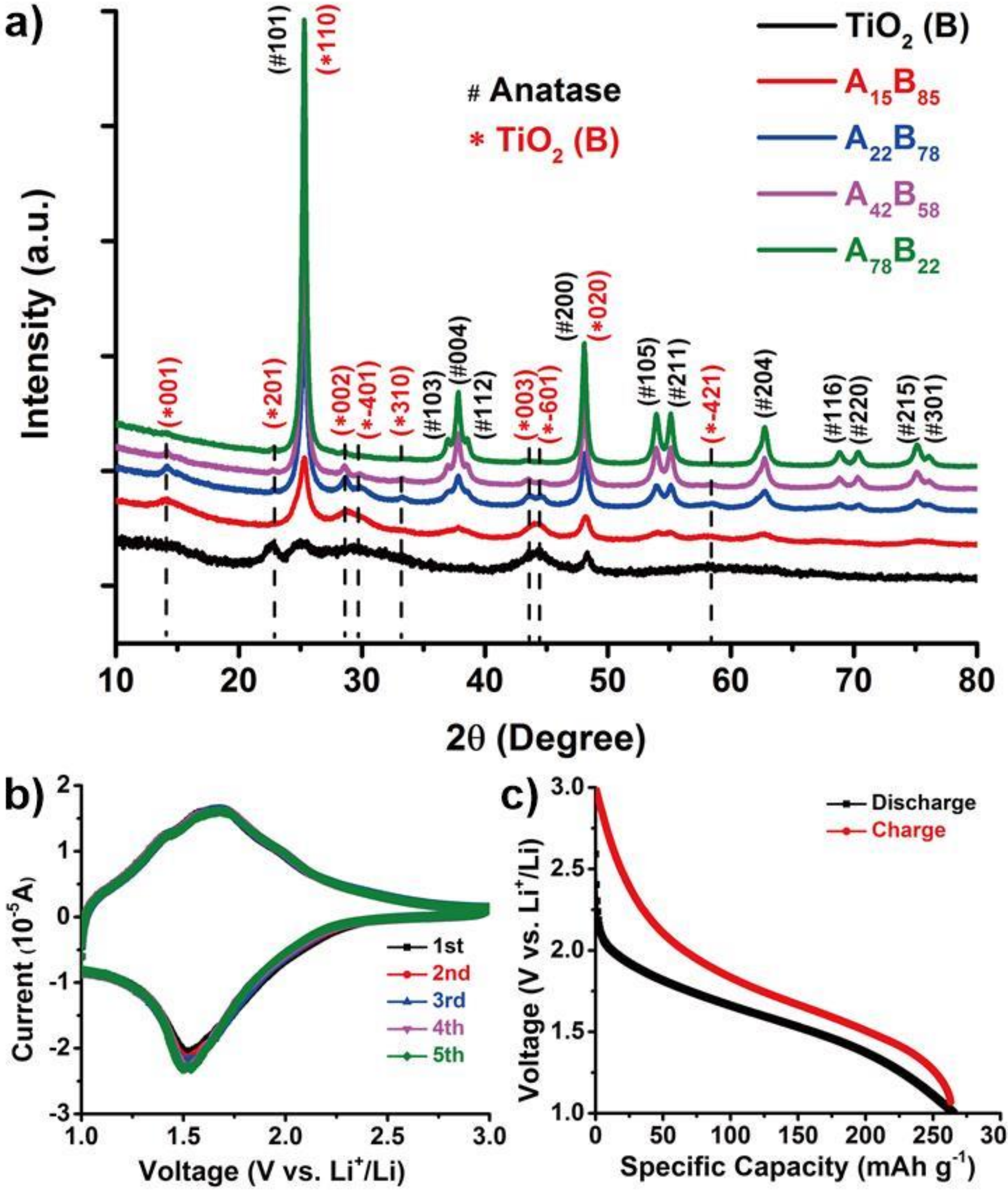

**Figure 4.1** Confirmation of $TiO_2$ phases: (a) XRD pattern; (b) Cyclic voltammograms of $TiO_2$ (B) electrode at scan rate 0.1 mV $s^{-1}$; (c) Discharge/discharge voltage profile of the $TiO_2$ (B) electrode at 0.2 A $g^{-1}$;

Figure 4.2 shows the CV curves and voltage profiles of the dual phase $TiO_2$ electrodes. As the anatase contents increases, the peak intensity for the pairs at 1.75 V/1.90 V increases and the plateau region in the voltage profile also becomes extended. Therefore, such electrochemical results could be used to quantify the relative ratio of anatase in the dual phase materials.

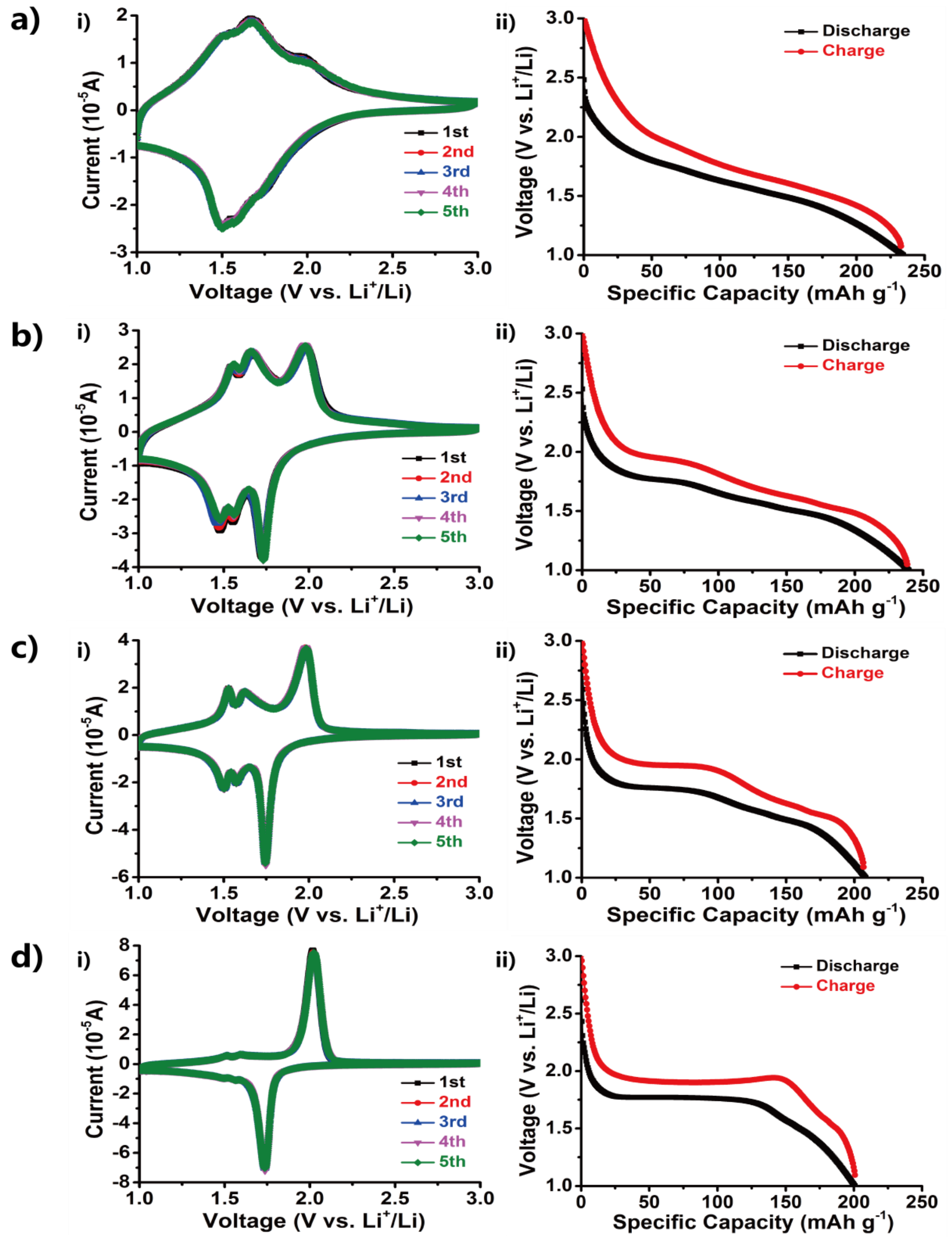

**Figure 4.2** Electrochemical characterization of the $TiO_2$ nanotube electrodes: (a-d) $A_{15}B_{85}$, $A_{22}B_{78}$, $A_{42}B_{58}$ and $A_{78}B_{22}$; i) Cyclic voltammograms at 0.1 mV $s^{-1}$, ii) discharge/charge voltage profile at 0.2 A $g^{-1}$.

The quantification on relative percentage of the anatase phase is first proposed by Brohan[33] based on area fitting from the derivatives of the galvanostatic discharge curve. The details are shown in Figure 4.3. The grey areas and grey lines refer to $TiO_2$ (B) part (area including A1, A2 and A3), while the black filled area refers to anatase part (A4). Orange line is the sum of all fitted contributions. At the current rate of 0.2 A $g^{-1}$, the specific capacity is 265.6 mAh $g^{-1}$ for $TiO_2$ (B) and 147.9 mAh $g^{-1}$ for anatase. Therefore the sensitive factor is determined to be 0.557. The absolute area under the four fitted peaks are A1 = 21.82, A2 = 229.66, A3 = 15.15 and A4 = 42.33. The area corresponds to $TiO_2$ (B) phase is A1+A2+A3 = 266.63. Therefore, the weight percentage of $TiO_2$ (B) is 78 %. Similar approaches are applied to quantify the ratio of anatase phase in other dual phase samples.

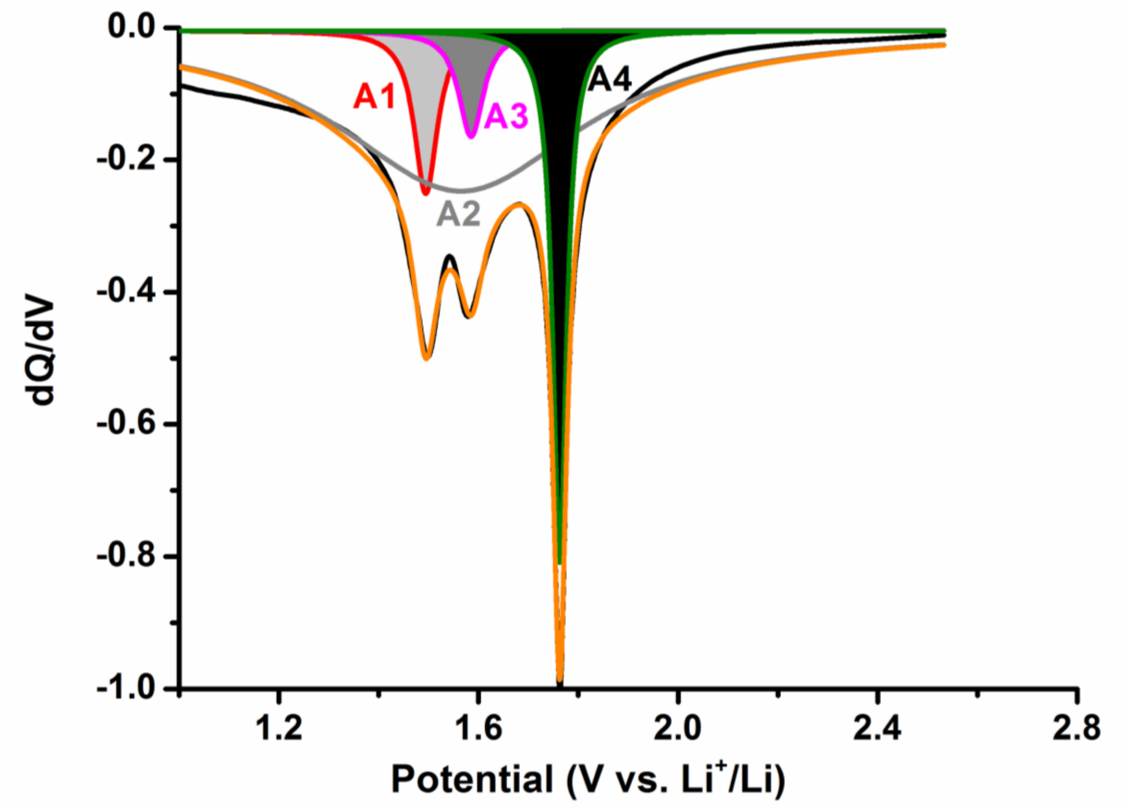

**Figure 4.3** Derivatives of the galvanostatic discharge curve ($A_{22}B_{78}$ electrode) to quantify the ratio of $TiO_2$ (B) and anatase phase

### 4.3.2 Confirmation of the Nanotube Morphology

It is essential for the preservation of nanotubular morphology for the *in situ* EIS measurement. The morphology of the $TiO_2$ materials is probed by the field emission scanning electron microscope (FESEM). After the thermal treatment, the morphology of dual phase $TiO_2$ with the highest annealing temperature was confirmed first. The FESEM images of the dual phase $A_{78}B_{22}$ materials (annealed at 700 ℃) are shown in Figure 4.4a; the elongated nanotubular morphology is well retained. These elongated nanotubes form a three-dimensional interconnected network with intimate contact among individual nanotubes, which is essential for the subsequent comparative study via *in situ* EIS technique. TEM images (Figure 4.4b) of the $A_{78}B_{22}$ materials confirm that the samples are multi-wall nanotubes, with inner diameter around 10 nm. From the HRTEM images in Figure 4.4c, the lattice distance of different crystal planes in $TiO_2$ (B) and anatase can be indexed, indicating the two phase co-existing nature of the materials.

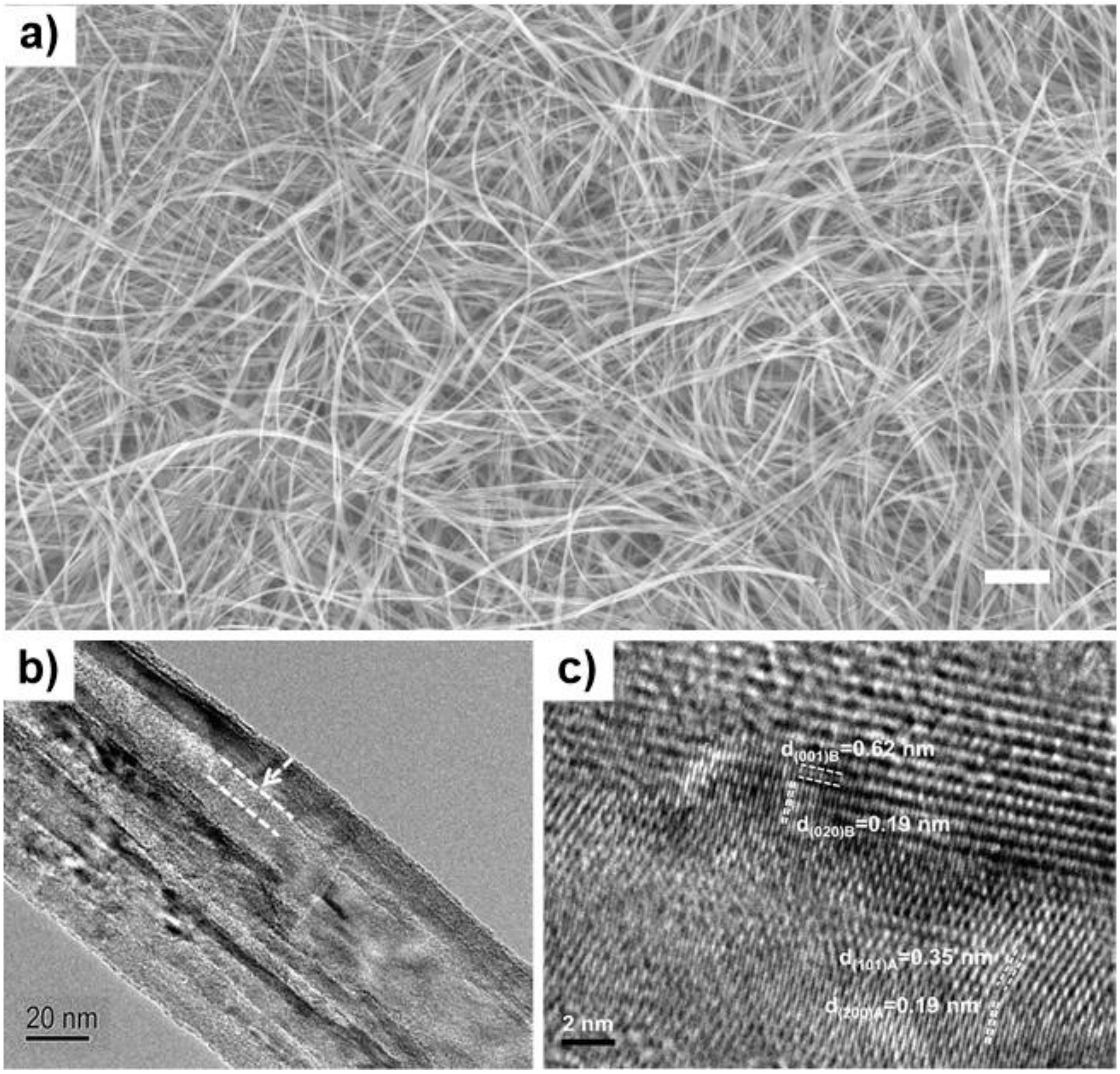

**Figure 4.4** Morphology characterizations of the dual phase $A_{78}B_{22}$ materials: (a) SEM image, scale bar is 1 μm; (b) TEM image (c) HRTEM image showing the lattice distance of the crystal planes.

The SEM images of other $TiO_2$ samples are shown in Figure 4.5. Since the nanotubes can withstand high annealing temperature of 700 ℃ without breaking into nanoparticles, therefore, the nanotubular morphologies are all retained in these samples obtained at lower annealing temperature. The length of such nanotubes can go up to tens of micrometers while the diameter is within 100 nm.

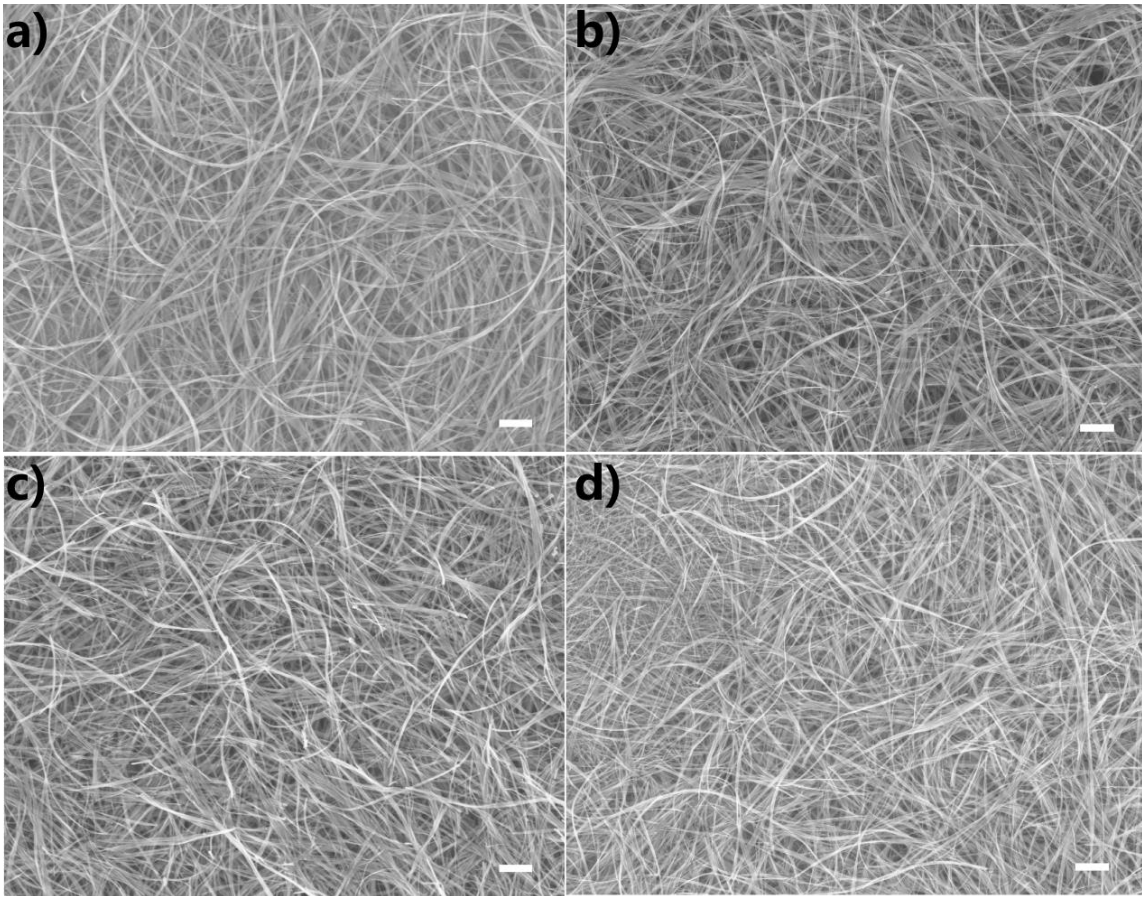

**Figure 4.5** SEM images of the $TiO_2$ nanotubular structure obtained after thermal treatment: (a-d) $TiO_2$ (B), $A_{15}B_{85}$, $A_{22}B_{78}$ and $A_{42}B_{58}$ samples. The elongated nanotubular structure is well preserved. Scale bar is 1 µm.

To further confirm the nanotubular morphology and probe the pore properties of the $TiO_2$ materials, surface area measurement was carried out and the results are shown in Figure 4.6. All samples shows similar BET surface area above 100 $m^2$ $g^{-1}$. Although slightly larger surface area (163 $m^2$ $g^{-1}$) is observed for pure phase $TiO_2$ (B), it is not the governing factor controlling the electrochemical performances since $TiO_2$ (B) exhibits pseudocapacitive charge storage behavior. Owing to the perseverance of nanotube morphology, pore volume and pore size of different samples are also quite similar. The pore size is slightly above 10 nm, which is in good accordance with the TEM results.

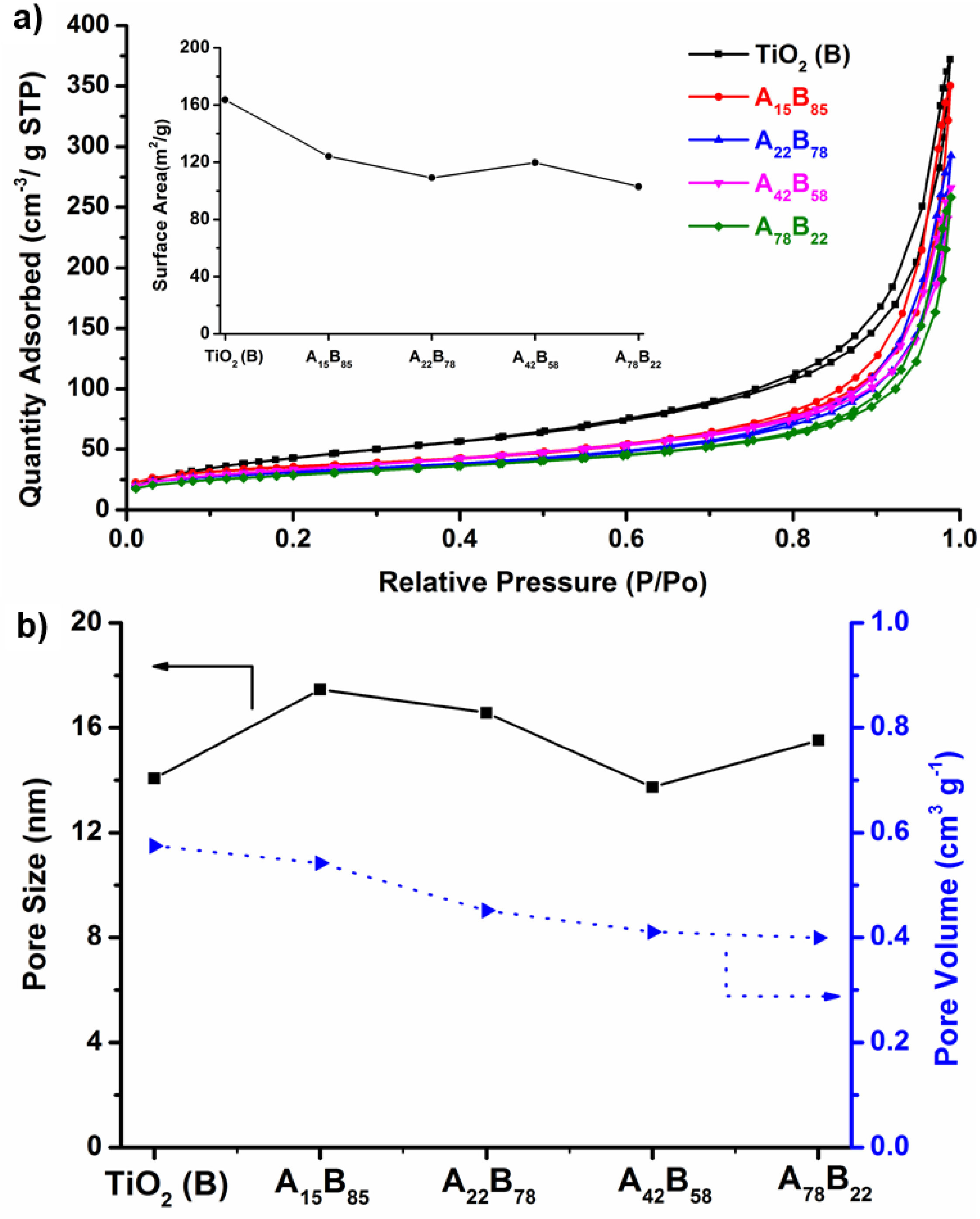

**Figure 4.6** (a) BET surface area (b) pore size and pore volume of the $TiO_2$ nanotubes obtained at different annealing temperature. Pure phase $TiO_2$ (B) features slightly higher surface area of 163 $m^2$ $g^{-1}$, all dual phase nanotubes have similar surface area above 100 $m^2$ $g^{-1}$.

### 4.3.3 Electrochemical Performance Evaluation

Next we verify the electrochemical performances of the additive-free $TiO_2$ nanotube electrodes with different phases, as presented in Figure 4.7. Figure 4.7a shows the representative discharge capacities of the $TiO_2$ electrodes at various current rates with cut-off voltage window of 1.0-3.0 V. In terms of high rate performances, dual phase electrodes are much superior to that of the pure phase $TiO_2$ (B) electrode: at current density of 24 A $g^{-1}$ (~ 72 C), pure phase $TiO_2$ (B) only delivers a capacity of 13.7 mAh $g^{-1}$, while dual phase materials can deliver capacity of 103.4, 112.1, 93.5 and 45.5 mAh $g^{-1}$ for $A_{15}B_{85}$, $A_{22}B_{78}$, $A_{42}B_{58,}$ and $A_{78}B_{22}$. Figure 4.7b shows the rate capacity as a function of anatase contents, the nanotubes with anatase contents around 20 % yields the best high rate capacities. It should be noted that at low current rate of 0.2 A $g^{-1}$, the capacity of the pure phase $TiO_2$ (B) electrode (267 mAh $g^{-1}$) is higher than that of the dual phase electrodes (244.6, 237.9, 198.3 and 179.6 mAh $g^{-1}$ for $A_{15}B_{85}$ and $A_{22}B_{78}$, $A_{42}B_{58,}$ and $A_{78}B_{22}$ electrodes), which can be attributed to the intrinsic lower capacity of the anatase phase.[34, 35] However, the capacity retention of dual phase electrodes at high rates is significantly higher (Figure 4.7c): at current density of 24 A $g^{-1}$, $TiO_2$ (B) only retains 5% capacity compared to the reference rate (0.2 A $g^{-1}$), while dual phase materials can retain up to 47 % of the capacity for $A_{22}B_{78}$ and $A_{42}B_{58}$, 42% for $A_{15}B_{85}$ and 25% for $A_{78}B_{22}$. Furthermore, dual phase electrodes also exhibit superior long term cycling performances. As shown in figure 4.7d, at current rate of 30 C (1 C= 335 mA $g^{-1}$), the dual phase electrode could deliver a capacity of 125.8, 145.5, 114.8 and 87.2 mAh $g^{-1}$ after 1000 cycles for $A_{15}B_{85}$, $A_{22}B_{78,}$ $A_{15}B_{85}$ and $A_{22}B_{78}$, respectively, while the capacity for pure $TiO_2$ (B) is only 25.1 mAh $g^{-1}$. In addition, the long-term cycling test of dual phase $A_{22}B_{78}$ electrode (Figure 4.8) yields a capacity of 131 mAh $g^{-1}$ after 10,000 cycles at 30 C, with 80% retention of the initial capacity (165 mAh $g^{-1}$); similarly, a capacity of 124 mAh $g^{-1}$ with 100% columbic efficiency can be delivered at higher rate of 60 C after 5,000 cycles. In fact, for the optimized electrode, a high capacity of 150 mAh $g^{-1}$ can be achieved even at high rate of 90 C, representing as one of the best start of the art performances for $TiO_2$-based electrodes.[9, 36]

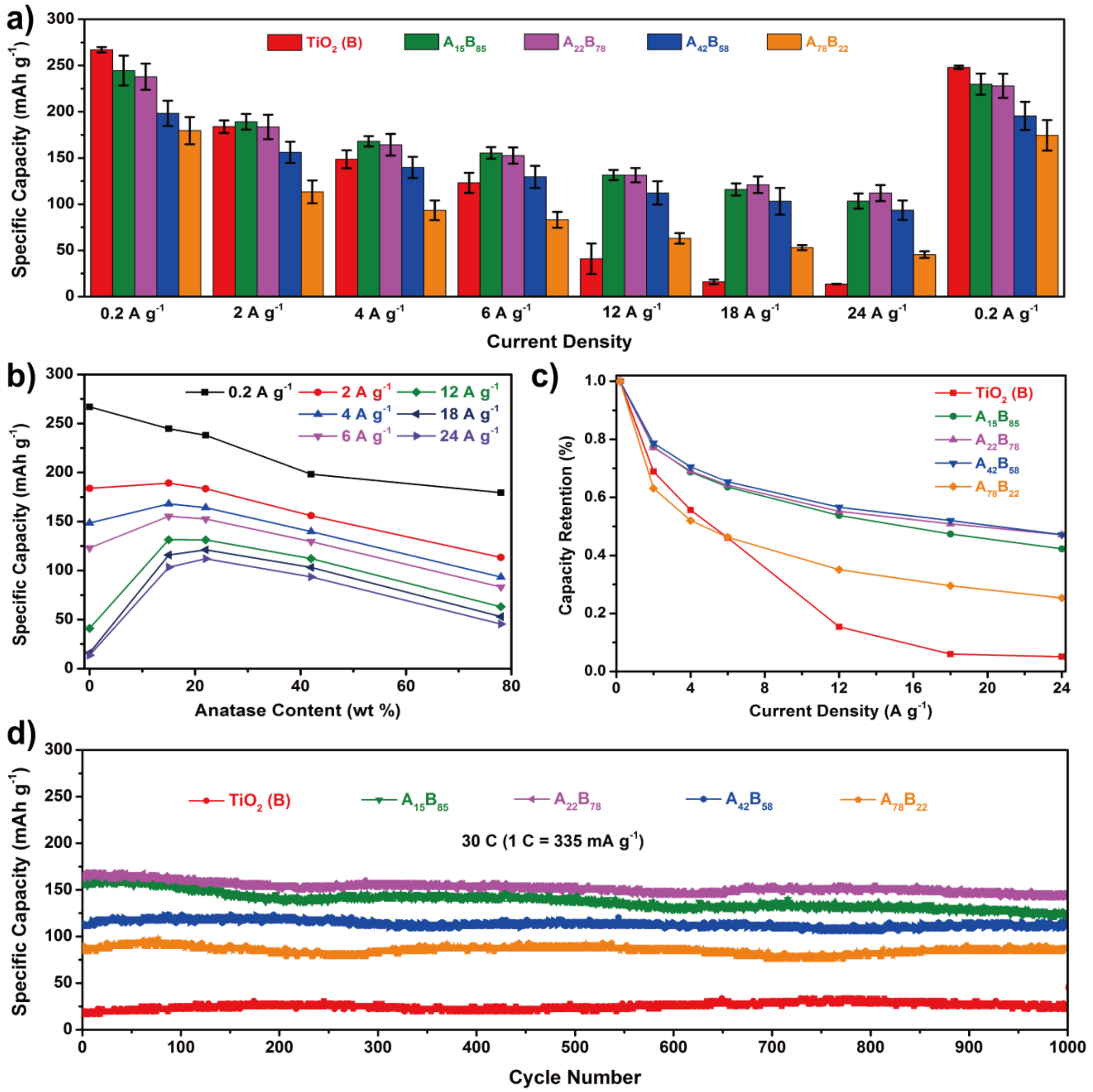

**Figure 4.7** Electrochemical performance of $TiO_2$ (B) and dual phase nanotube electrodes: (a) Rate performance conducted at each current density based on the discharge capacity of final cycle; (b) Capacity plots as a function of anatase phase contents; (c) Capacity retention at different current rates compared to the reference value at 0.2 A $g^{-1}$; (d) Long-term cycling performances of the electrodes at 30 C for 1,000 cycles.

The superior high rate performances of the dual phase $A_{22}B_{78}$ materials can be further manifested by the galvanostatic voltage profile as shown in Figure 4.8c. The materials exhibits low voltage polarization effect, therefore the discharging voltage starts at around 1.6 V even at high rate of 90 C, so that the main reaction window of $TiO_2$ (B) (1.6 V-1.4 V) is still preserved and higher capacity of 150 mAh $g^{-1}$ can be delivered.

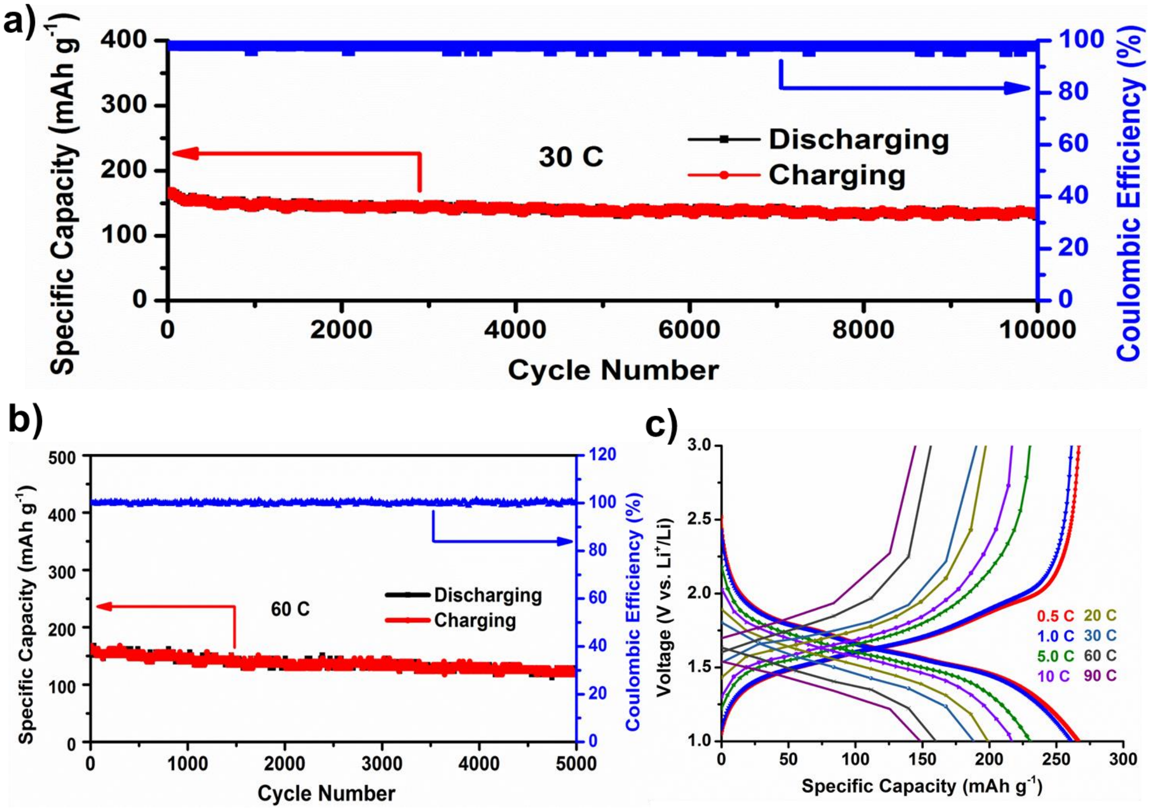

**Figure 4.8** Long-term cycling performances and columbic efficiency of the dual phase $A_{22}B_{78}$ electrodes: a) at 30 C for 10,000 cycles b) at 60 C for 5,000 cycles. c) Discharge/charge voltage profiles of the dual phase electrodes up to 180 C.

### 4.3.4 Insights on the Lithiation-induced Conductivity

To unravel the mechanism of excellent high rate performance of dual phase $TiO_2$ nanotubes and understanding the effect of anatase phase, the lithiation-induced conductivity of the additive-free electrodes is monitored through *in situ* EIS technique where the impedance of the cell was measured at open circuit voltage (OCV), 1.8 V, 1.6 V, 1.4 V, 1.2 V and 1.0 V during discharge. These voltages are selected to probe the change of conductivity before the onset of two-phase lithiation region in anatase phase (1.75 V) and during the major lithiation region of $TiO_2$ (B) (1.4-1.6 V). A typical Nyquist plot and voltage profile of the $TiO_2$ (B), anatase and dual phase $A_{22}B_{78}$ electrodes are presented in Figure 4.9. The Nyquist plot consists of a high frequency depressed semicircle and a low frequency linear Warburg region. The high-frequency semicircle is associated with the charge-transfer resistance related to lithium-ion interfacial transfer, coupled with a double-layer capacitance at the interface, while the low frequency region corresponds to the diffusion of lithium ions inside the materials.[37, 38] In $TiO_2$ electrode without the formation of solid electrolyte interphase (SEI) layer, the electrical conductivity of electrode materials is mainly manifested by the charge transfer resistance $R_{ct}$ and the diffusion kinetics are related to chemical diffusion coefficient ($D_{\mathrm{Li}}$), these values at different lithiation stage are summarized in Figure 4.9e&f. For $TiO_2$ anode materials, the lithiation reaction proceeds according to the following reaction,

$$xLi + TiO_2 + xe^- \leftrightarrow Li_xTiO_2 \tag{4.1}$$

For $TiO_2$ (B) phase, the lithiation reaction propagates through a monophasic lithiation process, with no change of the pristine monoclinic phase.[39] In the pristine state, $TiO_2$ (B) features poor electrical conductivity (Figure 4.7a&e), which hinders the movement of electrons towards the materials surface, thus the $R_{ct}$ at initial state is very large (215.8 Ω). Upon lithiation, the insulting $Ti^{4+}$ state is transformed to more conductive $Ti^{3+}/Ti^{4+}$ mixed state, therefore, the overall conductivity increases and the charge transfer resistance $R_{ct}$ decreases to 132.3 Ω at 1.4 V and 117.9 Ω at fully discharged state of 1.0 V. In contrary to the behavior of pure phase $TiO_2$ (B), $R_{ct}$ for anatase phase features different trends. As shown in Figure 4.9b, since a solid solution of lithium and anatase $TiO_2$ will form first upon reaction, the overall resistance decreases at the very early stage of reaction, which is in accordance with previous study on anatase nanorods.[25] The $R_{ct}$ for anatase electrode is 167.3 Ω at initial state and rapidly decreased to 85.5 Ω in the solid solution region. After two phase lithiation process (plateau region), $R_{ct}$ increases to 147.9 Ω at 1.6 V and gradually reaches 154.4 Ω at final discharge state (1.0 V). Such phenomenon can be attributed to the sluggish lithium diffusion behavior in the newly formed orthorhombic $Li_{0.55}TiO_2$ phase, which hinders the overall charge transfer kinetics.[40-43] Combining the advantages of both $TiO_2$ (B) and anatase phase, the $R_{ct}$ for dual phase $A_{22}B_{78}$ electrode decreases to a very small value of 55.4 Ω at very early stage of lithiation (1.8 V) and remains relatively invariant during further lithiation process. Such behavior can be attributed to the synergistic effect between the two phases during the lithiation process, first of all, at very early stage (1.8 V), the electrical conductivity enhancement of lithiated anatase phases facilitates the movement of electrons towards the surface to combine with lithium ions, thus reducing the overall charge transfer resistance. Upon further lithiation, the main reaction occurs in the $TiO_2$ (B) phase where lithium diffusion is rapid through pseudocapacitive charge storage behavior. Therefore, the overall resistance remains small.

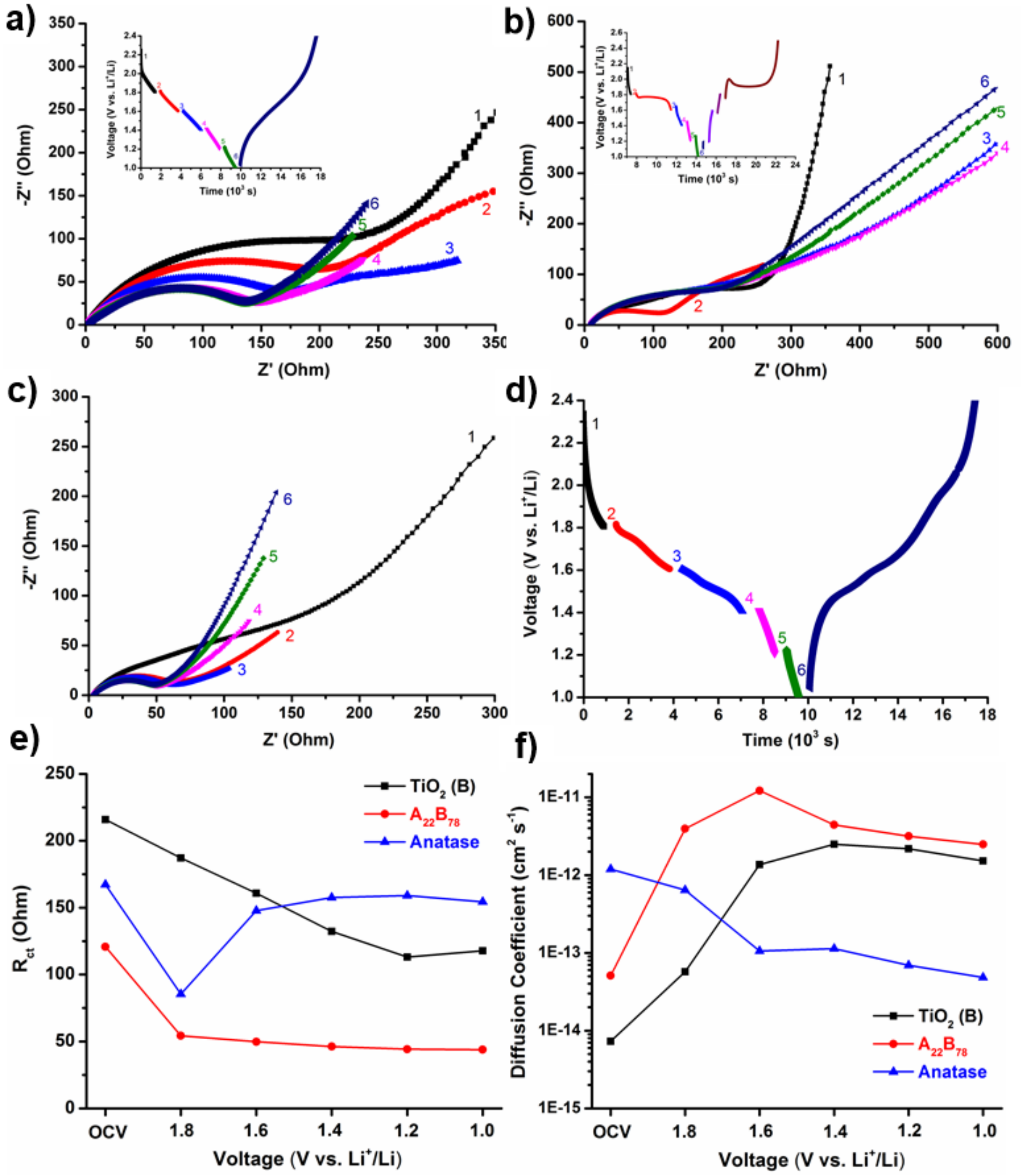

**Figure 4.9** *In situ* EIS study of the additive-free $TiO_2$ nanotube electrodes: (a-b) Nyquist plots of $TiO_2$ (B) and anatase electrode, respectively, inset is the corresponding voltage time profile; (c) Nyquist plots of dual phase $A_{22}B_{78}$ electrode at different voltages; (d) The corresponding voltage profile; (e-f) Summary of charge transfer resistance $R_{ct}$ and chemical diffusion coefficient during the lithiation (discharge) process.

In battery electrodes, high power performances can only be achieved with both high electron conduction and fast lithium ion diffusion kinetics. Diffusion kinetics is related closely to the chemical diffusion coefficient ($D_{\mathrm{Li}}$), which can be calculated from Fick's second law: [44, 45]

$$\sigma = \frac{RT}{\sqrt{2D_{Li}}n^2F^2SC} \tag{4.2}$$

Where σ denotes the Warburg coefficient, which can be calculated from the slope of the real part of the impedance (Z') versus ($\omega^{-1/2}$) (ω is angular frequency), $R$ is ideal gas constant, $T$ is absolute temperature, $F$ is Faraday constant, and $n$ is the valence number (n=1), $C$ is the concentration of lithium ions, $S$ denoted the contact area between active materials and the electrolyte, the electrode area is used in current calculation. The chemical diffusion coefficient ($D_{\mathrm{Li}}$) is a product of self-diffusion and Wagner factor: [46, 47]

$$D_{Li} = D_{Li(self)} \cdot \Phi \tag{4.3}$$

While self-diffusion is mainly related to the crystal structure of the materials, the thermodynamic factor Φ (also called Wagner factor) is a function of the concentration of mobile ions ($c_i$), concentration of the electronic species ($c_e$), transference number for electrons ($t_e$), and the charge valence number ($z_i$):

$$\Phi = t_e\left[1 + z_i^2(\frac{c_i}{c_e})\right] \tag{4.4}$$

In materials with mixing conduction behavior, there is an influence of electron motion on the mobile ions through internal electrical field effect. During the electro-intercalation, the electrons move ahead of the mobile ions and generate an internal field to accelerate the motion of ions to maintain electroneutrality. Typically large thermodynamic factor can be obtained at sufficiently small electron concentrations and high electronic mobility, which is a situation commonly fulfilled by semiconductors.[48] The chemical diffusion coefficient for the $TiO_2$ nanotube materials is shown in Figure 4.9f, an increase of the chemical diffusion coefficient is observed for all dual phase $TiO_2$ electrodes at early stage of reaction (1.8 V), indicating that the electrical conductivity can be improved at very low electron concentrations to enhance the overall diffusion kinetics. Owing to the slow enhancement in electrical conduction in $TiO_2$ (B), the chemical diffusion coefficient increases gradually from ~$10^{-15}$ cm$^2$ s$^{-1}$ at pristine state to ~$10^{-12}$ cm$^2$ s$^{-1}$ at 1.2 V. While for anatase electrodes, we observed one order decrease of the chemical diffusion coefficient from $1.2\times10^{-12}$ cm$^2$ s$^{-1}$ at initial state to $1.0\times10^{-13}$ cm$^2$ s$^{-1}$ at 1.6 V after the two phase lithiation reaction; this phenomenon can be attributed to the crystal structure changes in the newly formed lithium titanate phase which hinders the motion of lithium ions. In dual phase $A_{22}B_{78}$ electrode, benefited from high electron conduction at low concentration, the chemical diffusion coefficient increases from $5.1\times10^{-14}$ cm$^2$ s$^{-1}$ at initial state to $1.2\times10^{-11}$ cm$^2$ s$^{-1}$ at 1.6 V and then decreases slightly to $2.5\times10^{-12}$ cm$^2$ s$^{-1}$ at 1.0 V. From 1.6 V downwards, the electrical concertation dwells significantly and $R_{ct}$ remains invariant, therefore the enhancement on the migration of lithium ions through electric field is limited. The chemical diffusion coefficient is reduced mainly related to the self-diffusion properties, since most available sites have been occupied by existing intercalated lithium ions, the excessive lithium ions inside the crystal structure hinders the movement of additional lithium ions. The lithiation-induced conductivity of other dual phase electrodes is shown in Figure 4.10. They exhibit similar behavior to that of the $A_{22}B_{78}$ electrode, i.e. the $R_{ct}$ becomes smaller and invariant during the early stage (1.8 V) and the corresponding chemical diffusion coefficient increases until 1.6 V and decreases slightly afterwards.

The insights gained from *in situ* EIS measurement shed light on the mechanism behind the high rate performances of the dual phase $TiO_2$ electrodes. Upon early stage of lithiation (1.8 V), the charge transfer resistance decreases for both $TiO_2$ (B) and anatase. However, at such dilute lithium concentration, the effect is more pronounced with anatase, while the electrical conductivity of the lithiated anatase in solid solution region (voltage ~1.8) can reach around 57 S cm$^{-1}$.[24] In addition, Wagemaker et al. demonstrated that the solid solution region in anatase can be extended when the size of anatase particles are reduced.[42] The nanotube wall thickness is within 10 nm range, the actual size of the anatase domains is expected to be even smaller considering the small amount of anatase impurities, therefore the solid solution region can host more than 0.1 mole of lithium (per mole of anatase), which turns anatase region into the *in situ* formed conductives dispersed around the $TiO_2$ (B) structure. Owing to the well mixture of the two phases (TEM images in Figure 4.4c) and the cross-linked elongated structures in the additive-free nanotube electrodes, conduction enhancement of the anatase phase will also benefit the surrounding $TiO_2$ (B) phase, therefore improving the electrical conduction of the entire electrodes.

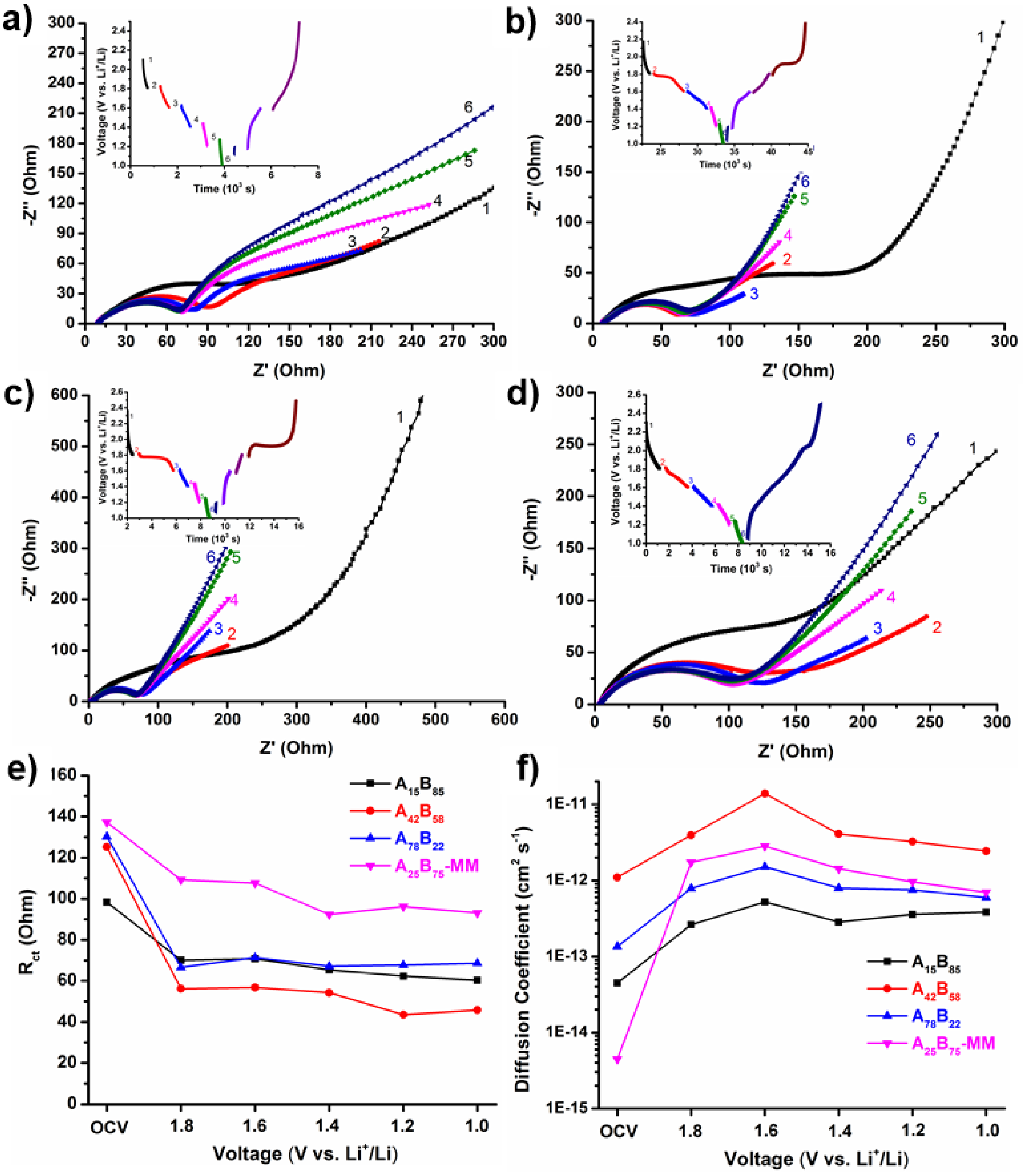

**Figure 4.10** Nyquist plots and the corresponding voltage profiles of the $TiO_2$ nanotube electrode during *In Situ* EIS study: (a-d) $A_{15}B_{85}$, $A_{42}B_{58,}$ $A_{78}B_{22}$ and $A_{25}B_{75}$-MM; (e-f) Summary of charge transfer resistance $R_{ct}$ and chemical diffusion coefficient during the lithiation (discharge) process.

Another evidence for the improved conduction in dual phase $TiO_2$ materials is the reduction of S2 peak voltage shift of $TiO_2$ (B), which lies directly after the voltage plateau of anatase (~ 1.75 V). Since anatase phase functions as the conductives formed *in situ* during the lithiation reaction, more anatase contents is expected to result in less peak shift in $TiO_2$ (B).

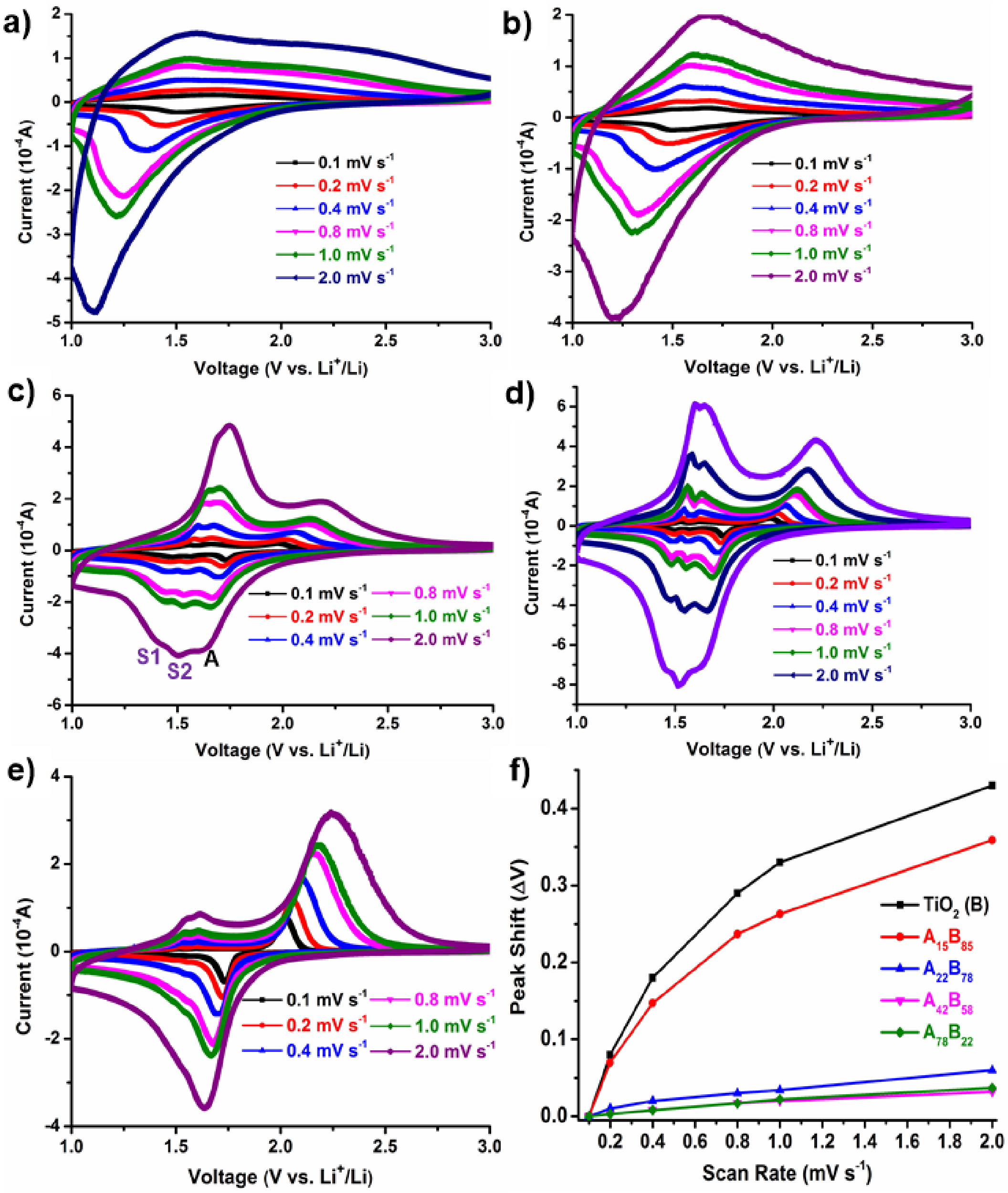

**Figure 4.11** Cyclic voltammograms of the $TiO_2$ nanotube electrodes at different scan rates: (a-e) $TiO_2$ (B), $A_{15}B_{85}$, $A_{42}B_{58,}$ and $A_{78}B_{22}$; (f) Peak shift of the $TiO_2$ (B) S2 peak at different scan rates (Reference state: 0.1 mV $s^{-1}$)

Indeed, as shown in Figure 4.11, the S2 peak shift in pure phase $TiO_2$ (B) could go as large as 0.42 V at scan rate of 2 mV $s^{-1}$compared to the reference state at 0.1 mV $s^{-1}$, while the value reduces to only 0.06 V for dual phase $A_{22}B_{78}$ electrode and further decreases to 0.04 V for $A_{78}B_{22}$ when anatase contents increases to 78 wt%. This smaller voltage shift results in low polarization effect, therefore at given voltage range of 1.0-3.0 V, the dual phase electrode delivers larger capacities at high current rates. However, although higher conductivity enhancement is observed with more anatase contents, anatase phase has inferior specific capacity and the high rate capacity is limited by sluggish diffusion in the newly formed orthorhombic lithium titanate phase after 1.75 V, thus an optimized amount of anatase at around 20 wt% yields the best overall performances in terms of both capacity and rate capacity. In such configuration, the ionic diffusion inside major $TiO_2$ (B) phase with open channel structure is not limited because a small percentage of the anatase phase is unlikely to block the lithium ion diffusion pathways. Indeed, as shown in Figure 4.9f&4.10f, the chemical diffusion coefficient in dual phase electrodes increases with the electron conduction until 1.6 V, beyond the formation of the orthorhombic $Li_{0.55}TiO_2$ phase. Given that the size of the nanotube walls are in range of tens of nanometer and the chemical diffusion coefficient in the range of ~ $10^{-12}$ $cm^2$ $s^{-1}$, according to the Fick's law, (diffusion time constant $t \approx l^2/\alpha$, $l$: diffusion length, $\alpha$: diffusion coefficient), the calculated diffusion time constant is in seconds scale, thus enabling very fast kinetics of the lithiation reaction.

To further verify the effect of anatase phase as *in situ* formed conductives during lithiation process, commercial anatase particles (< 25 nm) are mechanically mixed with the $TiO_2$ (B) nanotubes (sample denoted as $A_{25}B_{75}$-MM, weight percentage of anatase phase is 25 %). Figure 4.12 shows the SEM image and the electrochemical performances. The dual phase $A_{25}B_{75}$-MM electrodes also feature good high rate performances: a capacity of 113.4, 98.4 and 91.2 mAh $g^{-1}$ can be delivered at current rate of 12, 18 and 24 A $g^{-1}$, in compassion to 41.1,16 and 13.7 mAh $g^{-1}$ delivered by pure phase $TiO_2$ (B) nanotubes. *In situ* EIS study (Figure 4.10e&f) of the $A_{25}B_{75}$-MM electrode indicates similar trends with the $A_{22}B_{78}$ electrode: smaller charge transfer resistance is observed at early stage of 1.8 V and the diffusion coefficient also improves significantly until 1.6 V, such high electron conduction and fast lithium ion diffusion renders the materials with higher rate performances. These findings further strengthen the importance of anatase phase to form the conductive pathways during lithiation for the high rate performances of the dual phase electrodes. Overall, better lithiation-induced conductivity is observed in dual phase electrodes with the synergistic effect of anatase and $TiO_2$ (B) phase during the lithiation process, which is accountable for the excellent high rate performances of the dual phase electrodes.

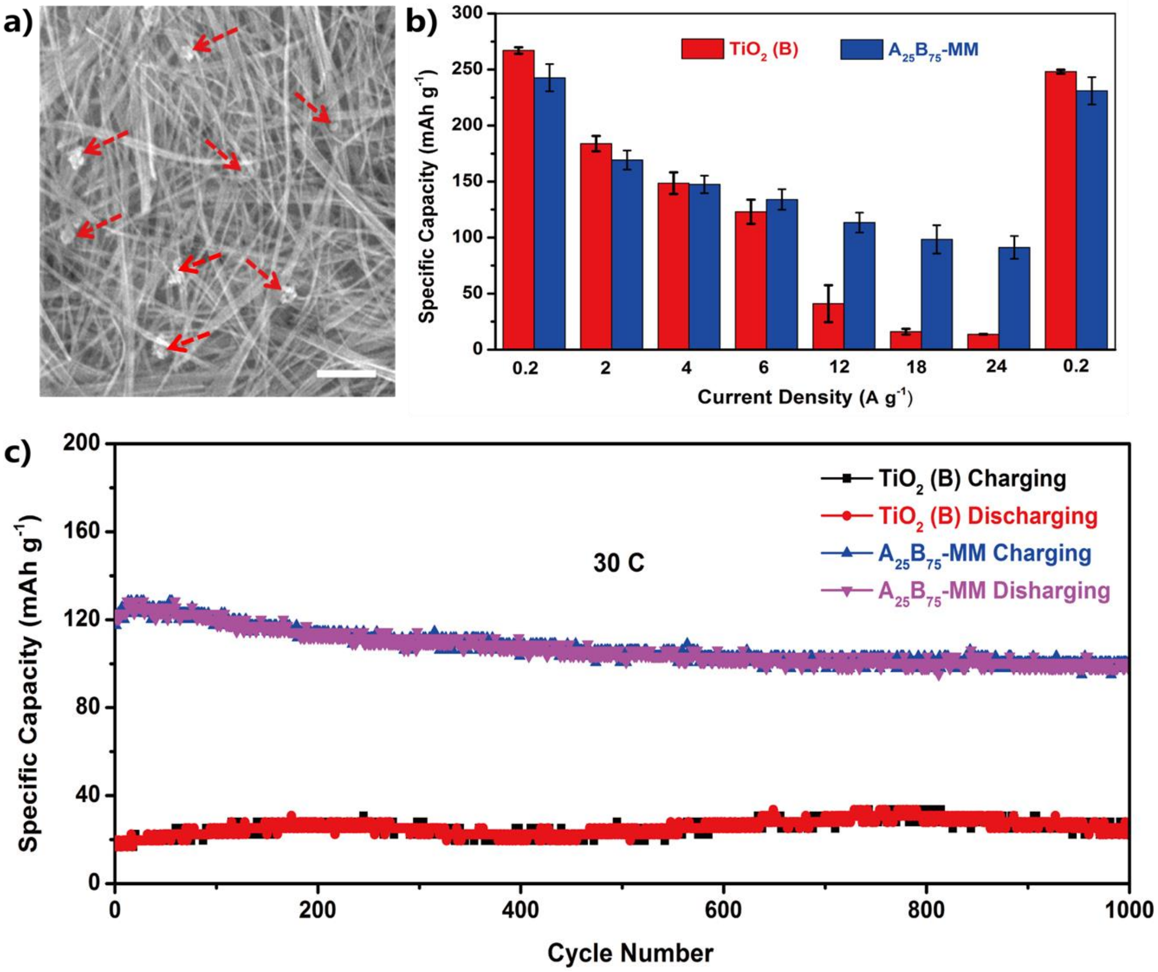

**Figure 4.12** (a) SEM image of mechanical mixed dual phase electrode $A_{25}B_{75}$-MM, scale bar is 1 µm; (b) Comparison on the battery performances of the $TiO_2$ (B) and $A_{25}B_{75}$-MM electrodes; (c) Long-term cycling performances at rate of 30 C for 1,000 cycles.

## 4.4 Conclusions

In conclusion, we have demonstrated that conductivity of $TiO_2$ (B) can be enhanced by integration with anatase and the dual phase $TiO_2$ nanotube electrodes exhibit much better performances at high current rates: a capacity of 131 mAh g$^{-1}$ after 10,000 cycles at 30 C and 124 mAh g$^{-1}$ after 5,000 cycles at 60 C is delivered for the $A_{22}B_{78}$ electrode. Applying additive-free $TiO_2$ nanotube electrodes as the platform, we systematically studied the conduction behavior in these $TiO_2$ materials via *in situ* EIS technique and unravel that the *in situ* formed conductive pathways from lithiated anatase is accountable for the superior rate performances in dual phase electrodes. Therefore, even the mechanically mixed anatase particles and $TiO_2$ (B) nanotubes show superior rate performances at 24 A $g^{-1}$ (91.2 mAh $g^{-1}$) than the pure $TiO_2$ (B) counterpart (13.4 mAh $g^{-1}$). Our present findings shed light on the importance of *in situ* formed conductives during lithiation reaction and provide design guidance for further research on $TiO_2$ materials for ultrafast charging LIBs. We envision that dual phase $TiO_2$ materials will play important roles for next-generation ultrafast charging and long lifetime LIBs and the lithiation-induced conductivity paves way for future exploration of its potential applications in a broad field.

## References

[1] M. Armand, J. M. Tarascon, *Nature* **2008**, *451*, 652.

[2] P. G. Bruce, B. Scrosati, J. M. Tarascon, *Angew. Chem. Int. Ed.* **2008**, *47*, 2930.

[3] L. Ji, Z. Lin, M. Alcoutlabi, X. Zhang, *Energy Environ. Sci.* **2011**, *4*, 2682.

[4] S.-T. Myung, N. Takahashi, S. Komaba, C. S. Yoon, Y.-K. Sun, K. Amine, H. Yashiro, *Adv. Funct. Mater.* **2011**, *21*, 3231.

[5] Y. Tang, Y. Zhang, W. Li, B. Ma, X. Chen, *Chem. Soc. Rev.* **2015**, *44*, 5926.

[6] A. R. Armstrong, G. Armstrong, J. Canales, R. García, P. G. Bruce, *Adv. Mater.* **2005**, *17*, 862.

[7] G. Armstrong, A. R. Armstrong, J. Canales, P. G. Bruce, *Chem. Commun.* **2005**, 2454.

[8] G. Armstrong, A. R. Armstrong, P. G. Bruce, P. Reale, B. Scrosati, *Adv. Mater.* **2006**, *18*, 2597.

[9] Y. Ren, Z. Liu, F. Pourpoint, A. R. Armstrong, C. P. Grey, P. G. Bruce, *Angew. Chem. Int. Ed.* **2012**, *51*, 2164.

[10] M. Zukalová, M. Kalbáč, L. Kavan, I. Exnar, M. Graetzel, *Chem. Mater.* **2005**, *17*, 1248.

[11] V. Augustyn, P. Simon, B. Dunn, *Energy Environ. Sci.* **2014**, *7*, 1597.

[12] C. Chen, Y. Wen, X. Hu, X. Ji, M. Yan, L. Mai, P. Hu, B. Shan, Y. Huang, *Nat. Commun.* **2015**, *6*, 6929.

[13] Y. Zhang, Q. Fu, Q. Xu, X. Yan, R. Zhang, Z. Guo, F. Du, Y. Wei, D. Zhang, G. Chen, *Nanoscale* **2015**, *7*, 12215.

[14] M. Fehse, E. Ventosa, *ChemPlusChem* **2015**, *80*, 785.

[15] V. Etacheri, J. E. Yourey, B. M. Bartlett, *ACS Nano* **2014**, *8*, 1491.

[16] Z. Sun, X. Huang, M. Muhler, W. Schuhmann, E. Ventosa, *Chem. Commun.* **2014**, *50*, 5506.

[17] S. Goriparti, E. Miele, M. Prato, A. Scarpellini, S. Marras, S. Monaco, A. Toma, G. C. Messina, A. Alabastri, F. D. Angelis, L. Manna, C. Capiglia, R. P. Zaccaria, *ACS Appl. Mater. Interfaces* **2015**, *7*, 25139.

[18] H. Liu, Z. Bi, X. G. Sun, R. R. Unocic, M. P. Paranthaman, S. Dai, G. M. Brown, *Adv. Mater.* **2011**, *23*, 3450.

[19] S. Liu, H. Jia, L. Han, J. Wang, P. Gao, D. Xu, J. Yang, S. Che, *Adv. Mater.* **2012**, *24*, 3201.

[20] A. G. Dylla, G. Henkelman, K. J. Stevenson, *Acc. Chem. Res.* **2013**, *46*, 1104.

[21] K. Saravanan, K. Ananthanarayanan, P. Balaya, *Energy Environ. Sci.* **2010**, *3*, 939.

[22] J.-Y. Shin, D. Samuelis, J. Maier, *Adv. Funct. Mater.* **2011**, *21*, 3464.

[23] Y. Tang, Y. Zhang, X. Rui, D. Qi, Y. Luo, W. R. Leow, S. Chen, J. Guo, J. Wei, W. Li, J. Deng, Y. Lai, B. Ma, X. Chen, *Adv. Mater.* **2016**, *28*, 1567.

[24] R. van de Krol, A. Goossens, E. A. Meulenkamp, *J. Appl. Phys.* **2001**, *90*, 2235.

[25] C. Kim, R. Buonsanti, R. Yaylian, D. J. Milliron, J. Cabana, *Adv. Energy Mater.* **2013**, *3*, 1286.

[26] C. Kim, N. S. Norberg, C. T. Alexander, R. Kostecki, J. Cabana, *Adv. Funct. Mater.* **2013**, *23*, 1214.

[27] Y. Tang, Y. Zhang, J. Deng, D. Qi, W. R. Leow, J. Wei, S. Yin, Z. Dong, R. Yazami, Z. Chen, X. Chen, *Angew. Chem. Int. Ed.* **2014**, *53*, 13488.

[28] Y. Tang, Y. Zhang, J. Deng, J. Wei, H. L. Tam, B. K. Chandran, Z. Dong, Z. Chen, X. Chen, *Adv. Mater.* **2014**, *26*, 6111.

[29] T. P. Feist, P. K. Davies, *J. Solid State Chem.* **1992**, *101*, 275.

[30] G. Armstrong, A. R. Armstrong, J. s. Canales, P. G. Bruce, *Electrochem. Solid-State Lett.* **2006**, *9*, A139.

[31] J. Li, H. Yang, Q. Li, D. Xu, *CrystEngComm* **2012**, *14*, 3019.

[32] B. Laskova, M. Zukalova, A. Zukal, M. Bousa, L. Kavan, *J. Power Sources* **2014**, *246*, 103.

[33] T. Beuvier, M. Richard-Plouet, L. Brohan, *J. Phys. Chem. C* **2009**, *113*, 13703.

[34] G. Zhang, H. B. Wu, T. Song, U. Paik, X. W. Lou, *Angew. Chem. Int. Ed.* **2014**, *126*, 12798.

[35] W. Li, F. Wang, Y. Liu, J. Wang, J. Yang, L. Zhang, A. A. Elzatahry, D. Al-Dahyan, Y. Xia, D. Zhao, *Nano Lett.* **2015**, *15*, 2186.

[36] K. Zhang, M. B. Katz, B. Li, S. J. Kim, X. Du, X. Hao, J. R. Jokisaari, S. Zhang, G. W. Graham, A. Van der Ven, B. M. Bartlett, X. Pan, *Adv. Mater.* **2014**, *26*, 7365.

[37] D. Aurbach, M. D. Levi, E. Levi, H. Teller, B. Markovsky, G. Salitra, U. Heider, L. Heider, *J. Electrochem. Soc.* **1998**, *145*, 3024.

[38] M. Park, X. Zhang, M. Chung, G. B. Less, A. M. Sastry, *J. Power Sources* **2010**, *195*, 7904.

[39] M. Fehse, M. Ben Yahia, L. Monconduit, F. Lemoigno, M.-L. Doublet, F. Fischer, C. Tessier, L. Stievano, *J. Phys. Chem. C* **2014**, *118*, 27210.

[40] M. Wagemaker, R. van de Krol, A. P. M. Kentgens, A. A. van Well, F. M. Mulder, *J. Am. Chem. Soc.* **2001**, *123*, 11454.

[41] C. Jiang, M. Wei, Z. Qi, T. Kudo, I. Honma, H. Zhou, *J. Power Sources* **2007**, *166*, 239.

[42] M. Wagemaker, W. J. H. Borghols, F. M. Mulder, *J. Am. Chem. Soc.* **2007**, *129*, 4323.

[43] W. J. H. Borghols, D. Lutzenkirchen-Hecht, U. Haake, E. R. H. van Eck, F. M. Mulder, M. Wagemaker, *PCCP* **2009**, *11*, 5742.

[44] N. Takami, A. Satoh, M. Hara, T. Ohsaki, *J. Electrochem. Soc.* **1995**, *142*, 371.

[45] J. Lu, C. Zhan, T. Wu, J. Wen, Y. Lei, A. J. Kropf, H. Wu, D. J. Miller, J. W. Elam, Y.-K. Sun, X. Qiu, K. Amine, *Nat Commun* **2014**, *5*.

[46] W. Weppner, R. A. Huggins, *J. Electrochem. Soc.* **1977**, *124*, 1569.

[47] Z. Li, F. Du, X. Bie, D. Zhang, Y. Cai, X. Cui, C. Wang, G. Chen, Y. Wei, *J. Phys. Chem. C* **2010**, *114*, 22751.

[48] L. A. Montoro, J. M. Rosolen, *Electrochim. Acta* **2004**, *49*, 3243.

# Chapter 5

## Pre-lithiated $TiO_2$ Nanotubes for High Power Lithium-ion Hybrid Capacitors

*In this chapter, we demonstrated that the electrical conductivity and the first cycle Columbic efficiency of the* $TiO_2$ *nanotube electrode can be improved by pre-lithiation. Applying a modified electrochemical lithiation method, we have successfully fabricated high energy and high power lithium-ion hybrid capacitors with additive-free* $TiO_2$ *nanotube electrode. An energy density of 50.8 Wh* $kg^{-1}$ *@ 492.6 W* $kg^{-1}$ *and power density of 8.98 kW* $kg^{-1}$ *@ 20.7 Wh* $kg^{-1}$ *can be achieved. Detail analysis of the mechanism indicates that the activated carbon based cathode materials feature dual-ion adsorption characteristics, at high voltage, the carbon cathode adsorbs anions in the electrolytes; while at low voltage, lithium ions will be shuttled between* $TiO_2$ *anode to cathode. Furthermore, such pre-lithiation process does not deteriorate the cycling performances of the* $TiO_2$ *nanotubes, at current rate of 2 A* $g^{-1}$*, 73 % of the energy is retained after 10,000 cycles. Such results further confirm the effect of lithiation in the dual phase composite electrode and paves way for the commercial adoption of* $TiO_2$ *anode materials in high power, long life lithium-ion hybrid capacitors.*

## 5.1 Introduction

Lithium-ion hybrid capacitors (LICs) with high power and long cycle life are attracting attention in recent years as promising electrochemical energy storage (EES) systems for applications ranging from energy regeneration, storage and load leveling in power grids.[1-3] The LIC is a battery supercapacitor hybrid system combing the long lifetime, high power characteristics of a supercapacitor and the high energy merits of a battery.[4, 5] In principle, the LIC devices utilize Faradic intercalation-based anode and non-Faradic adsorption-based cathode materials to provide high energy and high power capability.[6] To achieve high power characteristics with long cycle life, the intercalation anode materials should be structurally robust and operate safely within the electrolyte stability window (1-4.5 V). In such regards, $TiO_2$ (B) constitutes as an attractive anode candidate for such applications [7-9] owing to its merits of suitable lithiation potential (~ 1.5 V), fast diffusion kinetics, long cycle life and small volumetric expansion upon lithiation (< 4%), which arises from its open channel structure and intrinsic pseudocapacitive charge storage behavior.[10-13] Wang et al. reported the LIC fabricated with $TiO_2$ (B) nanowires coupled with carbon nanotubes (CNT) cathode, which delivers maximum capacity of 12.5 Wh kg$^{-1}$ at power density of 300 W kg$^{-1}$ in voltage range of 0-2.8 V.[7] Aravindan et al. reported $TiO_2$ (B) nanorods as anode for the LICs, coupled with activated carbon, this LIC delivers maximum energy densities of 23 Wh kg$^{-1}$ at 100 W kg$^{-1}$ and maximum power density of 2.8 kW kg$^{-1}$ can be achieved when the energy density falls below 10 Wh kg$^{-1}$.[9] Compared to $TiO_2$ (B), it is surprising to know that the anatase phase actually performs better for the application of LIC; a high specific energy density of 42 Wh kg$^{-1}$ can be delivered at 800 W kg$^{-1}$ over potential range of 1-3 V. However, at ultrahigh power density of 8000 W kg$^{-1}$, the energy density falls to 8.9 Wh kg$^{-1}$.[6] The quick dropping in the overall energy density at high power hinders the practical applications of the $TiO_2$ materials for LIC devices.

Generally, there are two major concerns in utilizing $TiO_2$ electrodes for high power LICs with high energy. The first issue is related to the poor electrical conductivity of the $TiO_2$ materials, which requires large amount of conductive for fast charging.[14-20] In addition, the large overpotential at high rates prevents the full utilization of the $TiO_2$ anode. The second issue is related to the poor first cycle Columbic efficiency, which results in loss of active materials and a reduction of the total energy and power density.[5, 21] Chapter 4 demonstrates that the dual phase $TiO_2$ materials exhibits superior high rate performances owing to the high lithiation conductivity at early stage with anatase phase. Therefore, in current work, pre-lithiation process is performed onto the dual phase $TiO_2$ materials to improve the electrical conductivity. Additionally, by supplying extra lithium ions, the first cycle Columbic efficiencies of the $TiO_2$ materials are also anticipated to improve. Therefore the pre-lithiated dual phase $TiO_2$ nanotubes are expected to be promising candidates for the high power, long life LICs.

## 5.2 Experimental Methods

### 5.2.1 Materials Synthesis

The $TiO_2$ nanotubes were synthesized following the methods described in chapter 4. The annealing temperature is fixed at 500 ℃ for 2 h with ramping speed of 3 ℃/min under vacuum ($10^{-5}$ mbar). Commercial activated carbon was purchased from Nanjing XFNANO Materials Tech, China (Surface area ~ 1800 $m^2$ $g^{-1}$). Single wall carbon nanotubes were purchased from BuckyUSA (Surface area ~ 788 $m^2$ $g^{-1}$). Carbon black (Super P) and PVDF were purchased from MTI Corporation, China. All materials are used without further treatment.

### 5.2.2 Pre-lithiation

The pre-lithiation process of the $TiO_2$ electrode is achieved by a modified electrochemical method as shown in Figure 5.1. Briefly, half cells with lithium metal counter electrode and additive-free $TiO_2$ working electrode were assembled inside Ar-filled glove box with $O_2$ and $H_2O$ contents below 0.6 ppm. The organic electrolyte with 1.0 M $LiPF_6$ dissolved in ethylene carbonate: diethyl carbonate (EC: DEC, 1:1 by weight) was purchased from Ferro Corp. The cell was connected to a resistor with resistance value of 20 kΩ. Owing to the potential differences between lithium meal and $TiO_2$, the cell will discharge automatically with electrons flowing through the resistor and lithium ions intercalated into the $TiO_2$ structure. The voltage of the cell is monitored with a multimeter during the discharging process. The lithiation process is terminated at pre-determined voltage indicated from the multimeter by removing the external resistor.

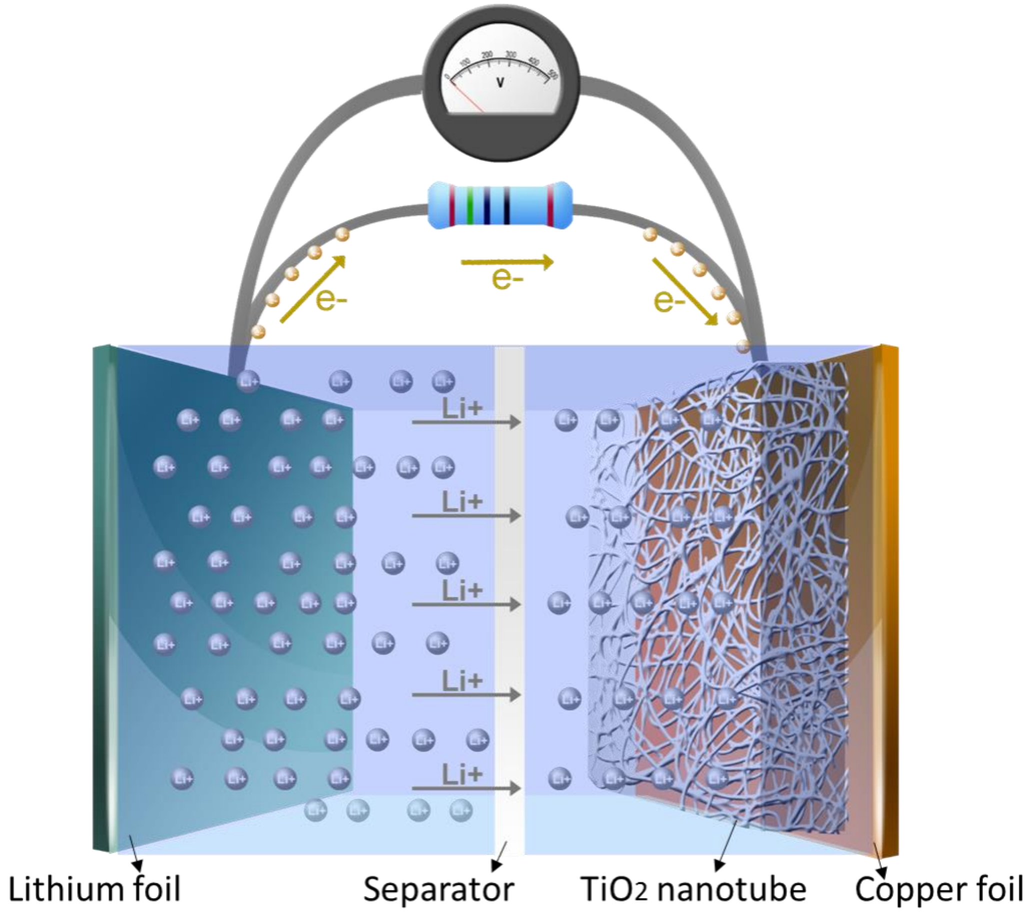

**Figure 5.1** Schematic on the pre-lithiation process for the $TiO_2$ nanotubes with lithium metal foil as the counter electrode.

### 5.2.3 Characterization

The morphologies of the as-synthesized nanotube samples were probed by field emission scanning electron microscope (FESEM, Carl Zeiss Supra 55). The acceleration voltage is 5 kV, and aperture size is 30 μm. The images are generated by the InLens detector for better resolution. Electrical conductivity of the materials was measured by the four-point probe method (Advanced Instrument Technology, CMT-SR2000N). The thickness of the measured samples is typically 20 μm.

### 5.2.4 Electrochemical Analysis

Electrochemical properties were investigated using 2032 coin cells. Half cells are used for the evaluation of materials properties with lithium metal as counter electrode and $TiO_2$ or carbon materials as active electrodes. Full cell hybrid capacitor is fabricated with $TiO_2$ nanotube anode and activated carbon/CNT composite cathode. The organic electrolyte with 1.0 M $LiPF_6$ dissolved in a mixture of ethylene carbonate and diethyl carbonate solvents (EC: DEC, 1:1 by weight) was used for all process. The galvanic cycling tests were performed on a CHI 660D electrochemical workstation (Shanghai ChenHua Instrument Company). Cyclic voltammetry (CV) study were carried out on a Solartron electrochemical workstation over a potential range of 1-3 V. *In situ* electrochemical impedance spectroscopy (EIS) measurements were also conducted with the Solartron workstation by applying a sine wave with amplitude of 10.0 mV over frequency range 100 kHz-0.1 Hz, the cell was allowed to rest 10 min before each EIS measurement. The loading density of $TiO_2$ is estimated to be ~ 1.0 mg $cm^{-2}$; mass ratio of cathode to anode is fixed at around 3:1.

## 5.3 Principal Outcomes

### 5.3.1 Effect of Pre-lithiation on the $TiO_2$ Nanotube Electrode

In chapter 4, we have demonstrated that lithiation process can improve the electrical conductivity of the $TiO_2$ materials by creation of the intermediate $Ti^{3+}$ state. In this study, since the pre-lithiation process is carried out directly after the cell is assembled, so *in situ* EIS study was performed in the first galvanostatic cycle, where the impedance of the cell was measured at open circuit voltage (OCV~2.8 V), 2.0 V, 1.8 V, 1.6 V, 1.4 V, 1.2 V and 1.0 V during discharge. The change of voltage profiles and the corresponding Nyquist plot is shown in Figure 5.2. The impedance for pristine $TiO_2$ nanotubes is enormous due to the poor electrical conductivity. Upon early lithiation to 2.0 V, the $TiO_2$ materials turn into dark color and the impedance decreases significantly, as evidenced by the reduction of charge transfer resistance ($R_{ct}$) to a small value of 63 Ω. further lithiation to 1.8 V and

1.6 V results in even lower $R_{ct}$ value around 25 Ω, which enables fast reaction kinetics for the application of hybrid capacitors.

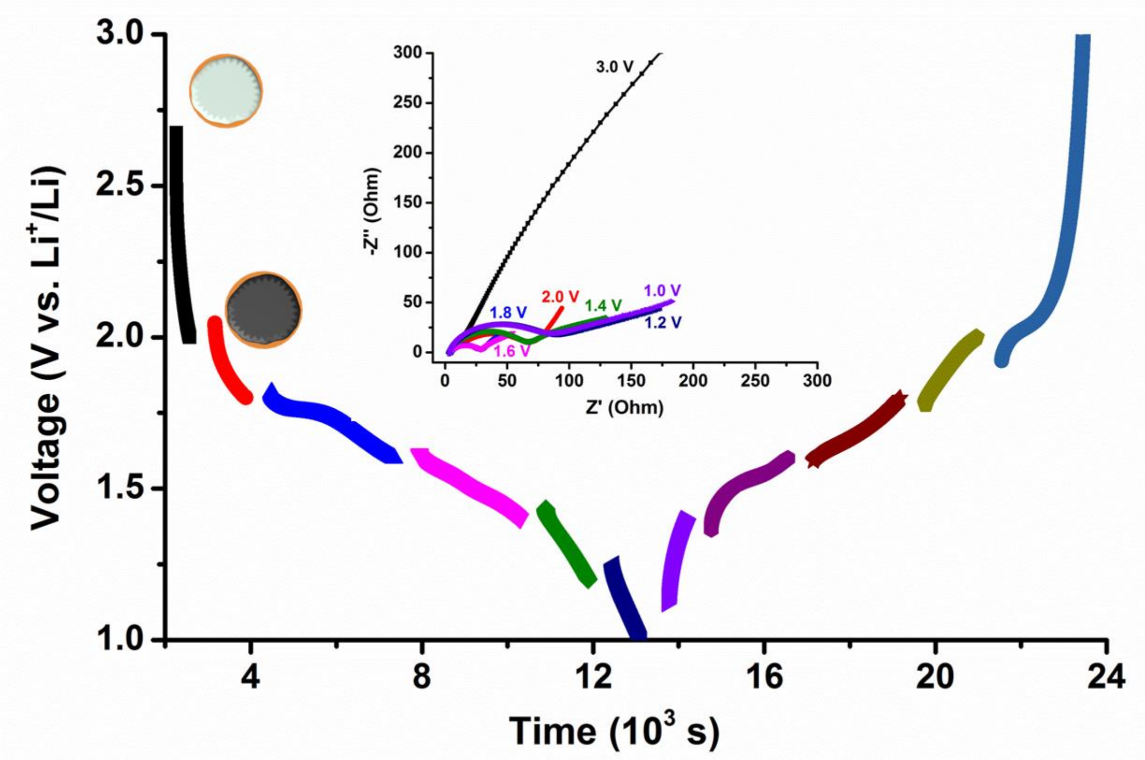

**Figure 5.2** Voltage profile during the *in situ* EIS measurement in the first cycle, inset is Nyquist plot at different discharging voltage. The color changes of the $TiO_2$ materials upon lithiation are schematically shown.

Conventional galvanostatic cycling test involves constant current discharging and charging, while our pre-lithiation method adopts the constant resistance approach for the discharging process, therefore it is necessary to evaluate the voltage and current profile during such process. As shown in Figure 5.3a, during the constant resistance lithiation process, the voltage profile is similar to that of the constant current mode. However, the discharge current reduces as the voltage drops, following Ohm’s law. The largest current density in the beginning is around 90 mA $g^{-1}$, corresponding to 0.3 C (1 C = 335 mA $g^{-1}$), Figure 5.3b shows the variation of cell voltage after pre-lithiation process followed by a rest period of 12 h. Owing to the large internal resistance of the pristine $TiO_2$ electrode, the voltage recovery at early stage of lithiation (2 V) is as large as 0.6 V after 12 h relaxation. Relatively stable voltage can be achieved by further lithiation to a voltage range between 1.8-1.4 V, where the recovery of voltage is within 0.2 V (Figure 5.3c). In particular, the most stable voltage is achieved at the voltage plateau region of anatase phase (~ 1.76 V upon 20 kΩ constant resistance discharging), since a large overpotential of 0.2 V has to be overcome for the lithium extraction process.

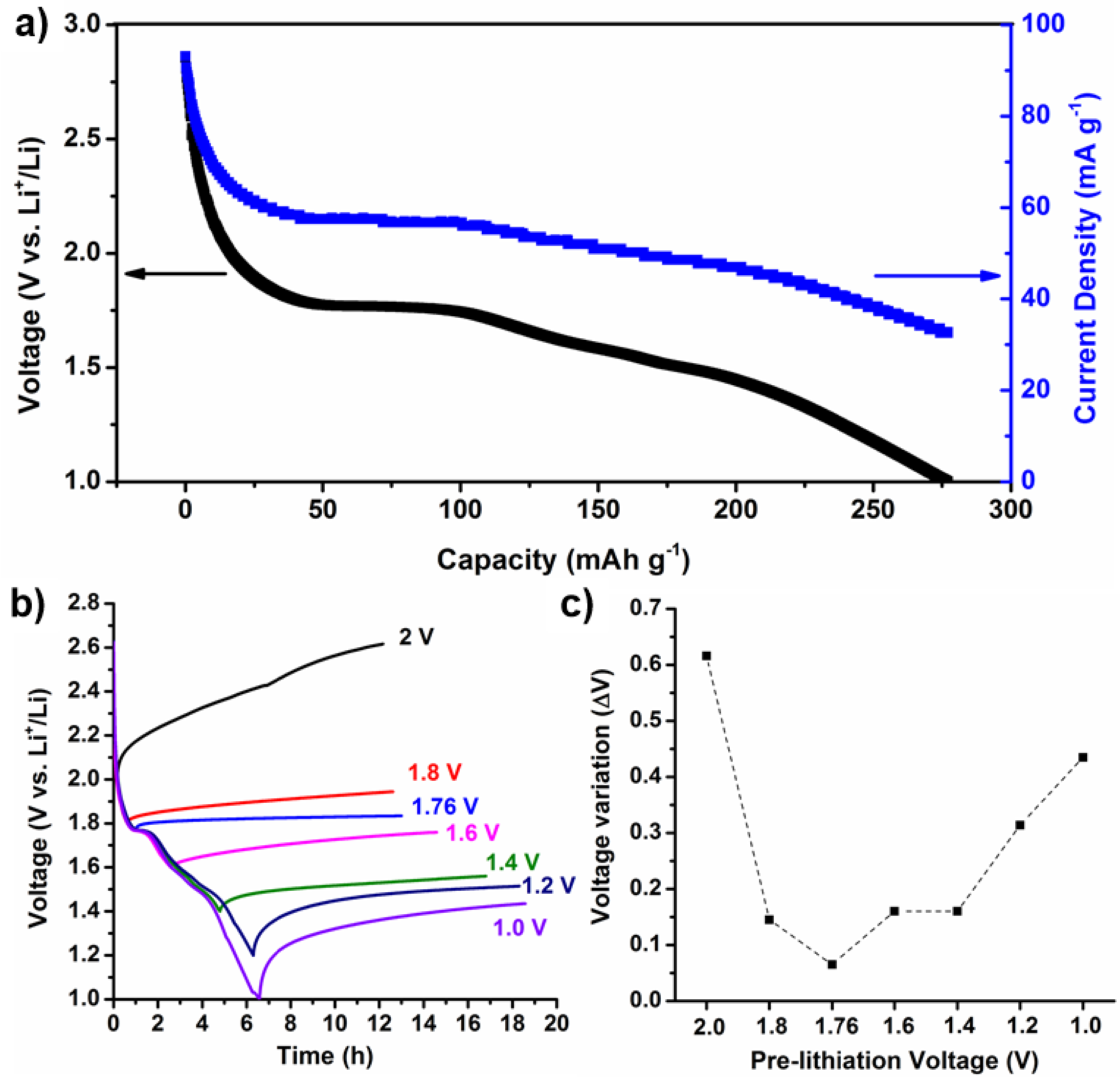

**Figure 5.3** (a) Voltage and current profile during constant resistance (20 kΩ) discharging process; Voltage recovery after the pre-lithiation process with a rest period of 12 h: (b) voltage variation profile during the 12 h period; (c) the change of final voltage compared to the initial value.

After 12 h resting process, the cell is subjected to a constant current discharging process at rate of 1 A $g^{-1}$; the specific capacity and capacitance of the $TiO_2$ materials are summarized in table 5.1. The specific capacity decreases with pre-lithiation process, since some available intercalation sites are already occupied with lithium ions. Of particular interest is the change of specific capacitance of the system. Capacitance is defined as the total amount of electric charges passed through a give voltage range. The specific capacitance can be calculated from the specific capacity by the following equation:[22]

$$C = Q/V \tag{5.1}$$

Where $Q$ is the specific capacity and $V$ is the voltage range (IR drop is excluded in the calculation). As summarized in table 5.1, the specific capacitance of $TiO_2$ increases first with the lithiation process until a voltage around 1.76 V and decreases thereafter. Herein the voltage range plays important roles for the variations of specific capacitance; a large value of 1274.04 F $g^{-1}$ achieved at pre-lithiation voltage 1.76 V indicates the strong ability to store electric changes, which is beneficial for the overall energy of the full cells.

**Table 5.1** Specific capacity and capacitance of $TiO_2$ materials at different pre-lithiation voltages followed by constant current discharging at 1 A $g^{-1}$ to 1.0 V.

| Pre-lithiation voltage (V) | Specific capacity to 1.0 V (mAh $g^{-1}$) | Voltage range (ΔV) | Specific capacitance (F $g^{-1}$) |
|---|---|---|---|
| 2.0 | 334.9 | 1.406 | 857.5 |
| 1.8 | 294.0 | 0.85 | 1245.24 |
| 1.76 | 267.2 | 0.755 | 1274.04 |
| 1.6 | 173.9 | 0.671 | 933.1 |
| 1.4 | 70.9 | 0.489 | 522.04 |
| 1.2 | 40.8 | 0.434 | 324.0 |
| 1.0 | 12.8 | 0.322 | 143.1 |

### 5.3.2 Optimization of the Cathode

In order to maximize the total energy stored in the hybrid LIC, large specific capacitance should be achieved in the cathode materials.[23, 24] In current study, commercial activated carbon (AC) with high surface area ~ 1800 $m^2$ $g^{-1}$ is used as the active materials. Conventional mixing process is to mix with conductive carbon black and PVDF binder, as shown in Figure 5.4b, the specific capacity of such configuration is 38.5 mAh $g^{-1}$ at low current rate of 0.1 A $g^{-1}$ over voltage range of 3.0-4.4 V. However, the value decreases to 9 mAh $g^{-1}$ when the rate increases to 0.4 A $g^{-1,}$ and the cell dies upon further increment of the current rates. Such inferior rate performances can be attributed to poor electrical conductivity of the composites (0.22 S $cm^{-1}$ as shown in Figure 5.4a). To improve the electrical conductivity, single wall carbon nanotubes (CNT) are used to form a composite with AC. The conductivity of AC/CNT composite increases to 21.1 S $cm^{-1}$ with only 10% CNT additives, which are 2 orders of magnitude higher than the AC/CB composite. It should be noted that the CNT (surface area ~ 788 $m^2$ $g^{-1}$) also store charges during the reaction process, although the ability is limited due to smaller surface area. A weight ratio of 8:2 (AC:CNT) delivers highest capacities at both low and high current rates, which can be attributed to the balance between improving electrical conductivity and reducing the ability of charge storage. In such optimized system, the capacity could go to 36 mAh $g^{-1}$ at 1 A $g^{-1}$, corresponding to capacitance of 92.6 F $g^{-1}$.

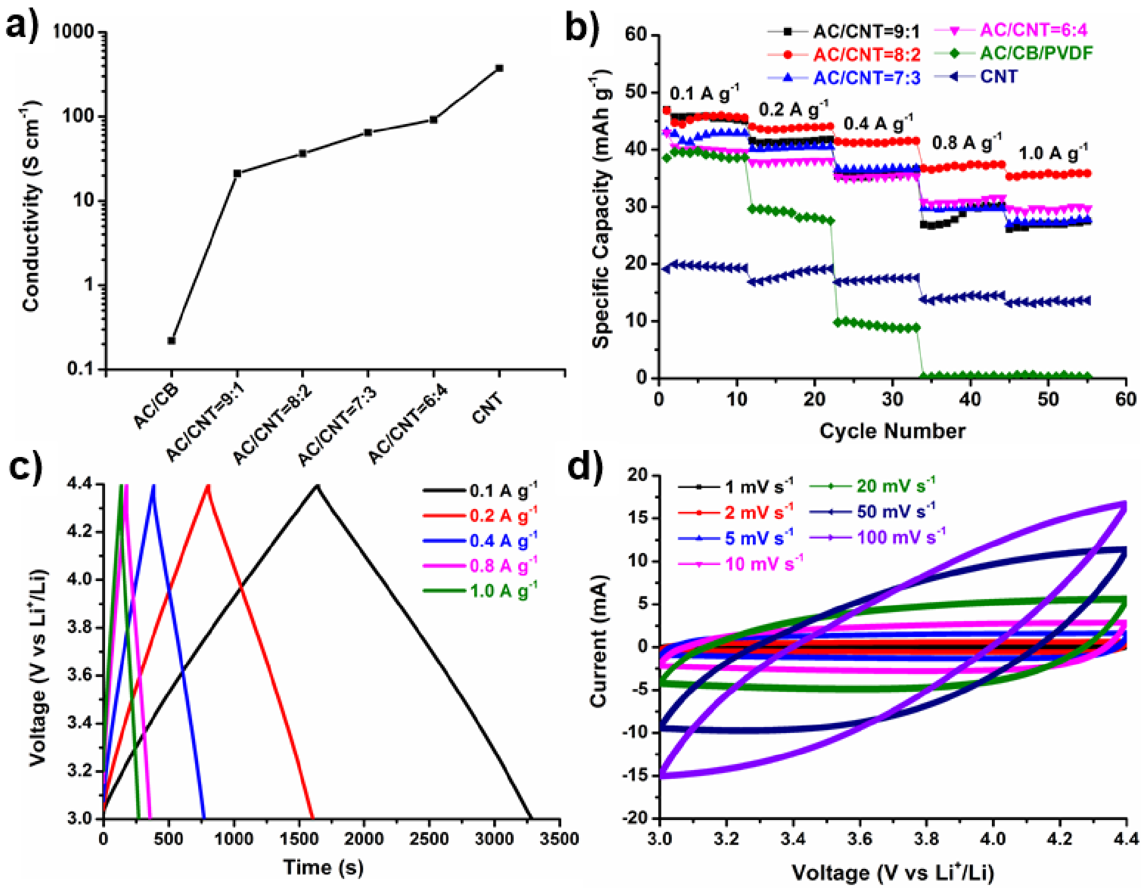

**Figure 5.4** Cathode characterizations for the hybrid LICs: (a-b) DC conductivity and specific capacity of different cathode composites; (c-d) charging/discharging voltage profile and cyclic voltammograms of the AC/CNT (8:2 weight ratio) electrodes.

The SEM images of the AC particles and CNT are shown in Figure 5.5. The AC particles are mesoporous materials with size in micrometer range (Figure 5.5a). The CNT features high aspect-ratio nanotubular structure with high viscosity when dispersed in ethanol. Such property enables fabrication of CNT and AC/CNT membrane via filtration method. As shown in Figure 5.5c&d, in the composites structure, CNT wraps around the AC particles and function as the backbone to provide electrical conductivity to fully utilize the charge storage capacities in the high surface area AC particles.

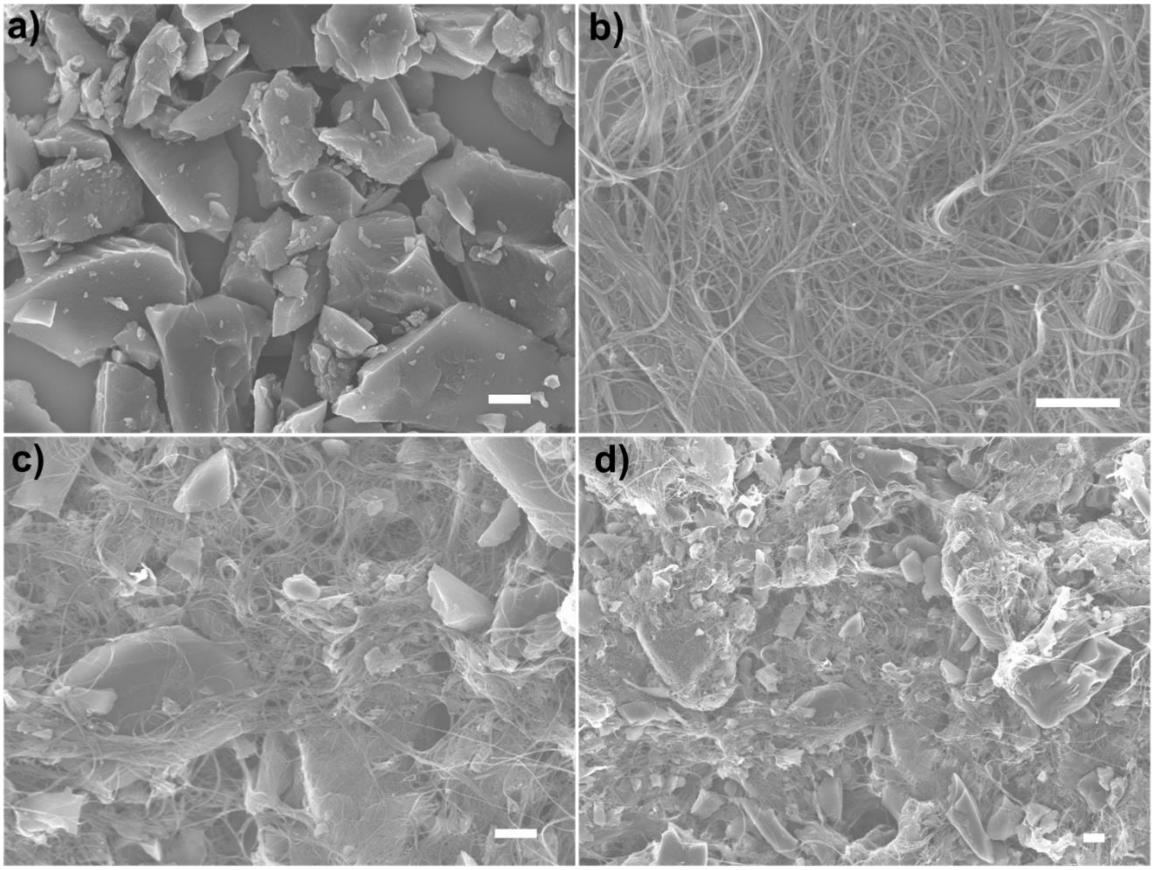

**Figure 5.5** SEM images of (a) activated carbon (b) single wall carbon nanotubes (SWCNT) (c-d) mixture of AC and CNT with mass ratio of 8:2. Scale bar is 1 μm.

### 5.3.3 Effect of Pre-lithiation on the Performance of LICs

With the optimized composite cathode (AC/CNT=8:2) and pre-lithiated $TiO_2$ anode, the performances of the full cell LICs are evaluated. The cathode to anode ratio is fixed at 3:1 in the full cell assembly process. Figure 5.6 shows the discharge/charge curves for the LIC based on pristine and pre-lithiated $TiO_2$ until 1.76 V. Note that the value 1.76 V lies on the voltage plateau of the anatase phase and is achieved by pre-lithiation for 1 h under 20 kΩ. Since the mass of anode materials is the same for different samples and the ratio of cathode to anode is fixed, the total discharging time is an indication of the overall capacity. As the pre-lithiation process proceeds to lower voltages (down to 1.76 V), the total time taken for the discharging increases (~250s for pristine $TiO_2$ and ~350s for the sample pre-lithiated to 1.76V). Given that the voltage profile does not vary significantly, therefore the overall energy of the system dwells, indicating the merits of the pre-lithiation process.

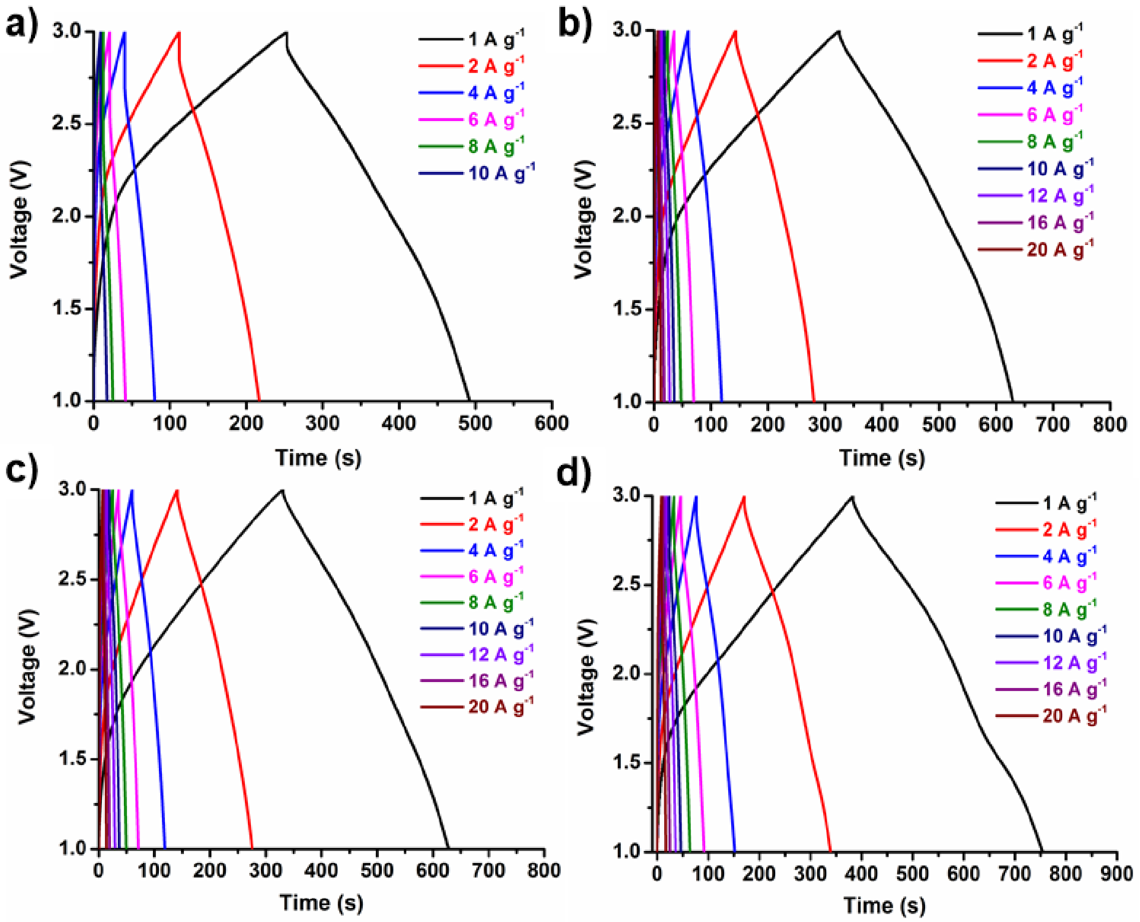

**Figure 5.6** Typical charge/discharge curves of the LIC with AC/CNT cathode and $TiO_2$ nanotube anode with different pre-lithiation condition: (a-d) pristine $TiO_2$, pre-lithiation to 2 V, 1.8 V and 1.76 V, respectively.

Another technique that can reflect the total energy of the LIC cells is cyclic voltammetry (CV) scan, where the energy is directly related to the area under the CV curve. The CV scans at different rates are shown in Figure 5.7. No obvious peaks can be observed in all cases, indicating that the charge storage is mainly capacitive in nature. For the pristine $TiO_2$ electrode, the shift of operation voltage towards smaller voltage value is significant, whereas for the pre-lithiated samples, the shift becomes less pronounced. In particular, the dominating operation voltage of the LIC cells with pre-lithiated $TiO_2$ electrode falls in higher range of 2.0-3.0 V with various CV scan rates. Such high voltage behavior is beneficial for the overall energy of the LIC.

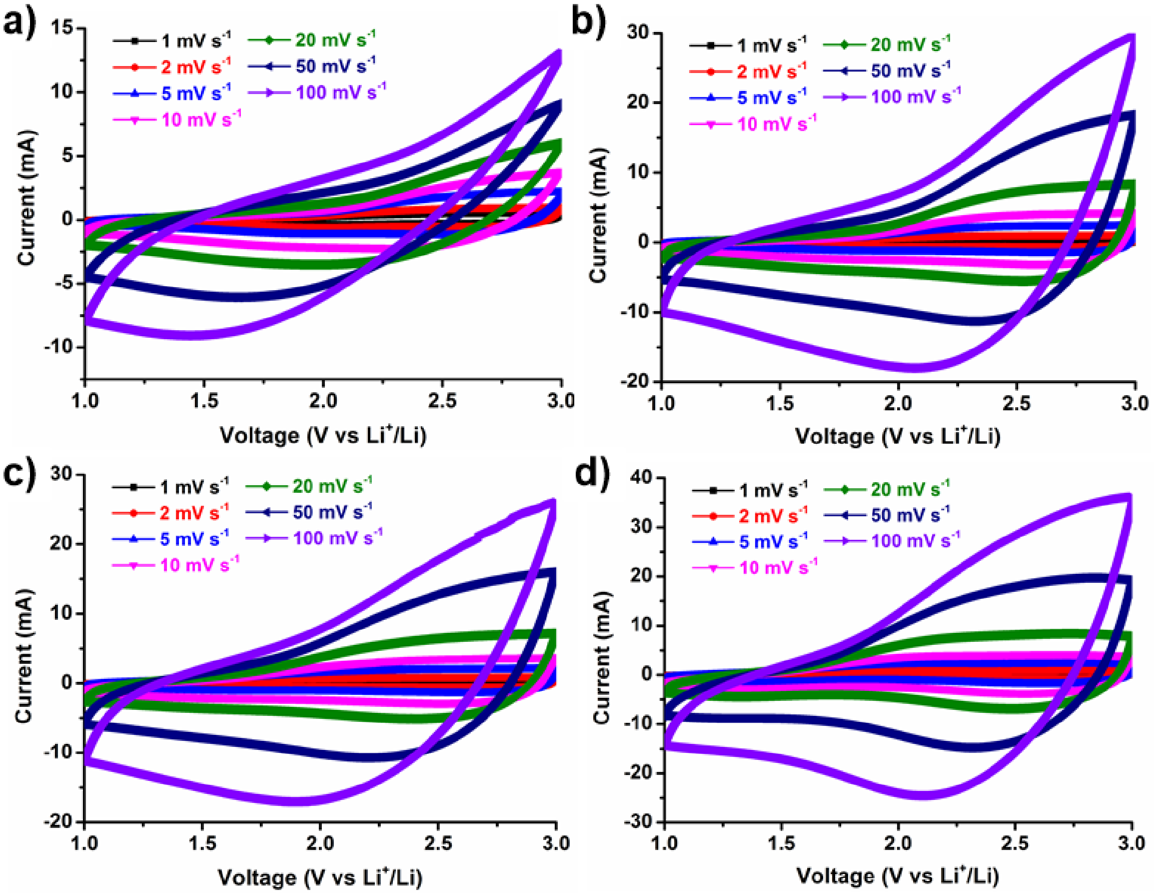

**Figure 5.7** Typical CV curves of the LIC with AC/CNT cathode and $TiO_2$ nanotube anode with different pre-lithiation condition: (a-d) pristine $TiO_2$, pre-lithiation 2 V, 1.8 V and 1.76 V respectively.

As the pre-lithiation process proceeds below 1.6 V, more lithium is intercalated inside the $TiO_2$ nanotube structure, and the available sites for further lithium storage decrease. Such effect becomes prominent especially when the lithiation voltage goes as low as 1.0 V. From the voltage profile shows in Figure 5.8d, during discharge, the voltage quickly drops to below 2.0 V, and the discharging time is also shortened significantly, which results in lower energy density of the LIC cells. It should be noted that the discharge voltage profiles of the LICs with pre-lithiation condition of 1.6 V and 1.4 V are not altered significantly, indicating that additional lithium storage phenomenon might be present in such configurations.

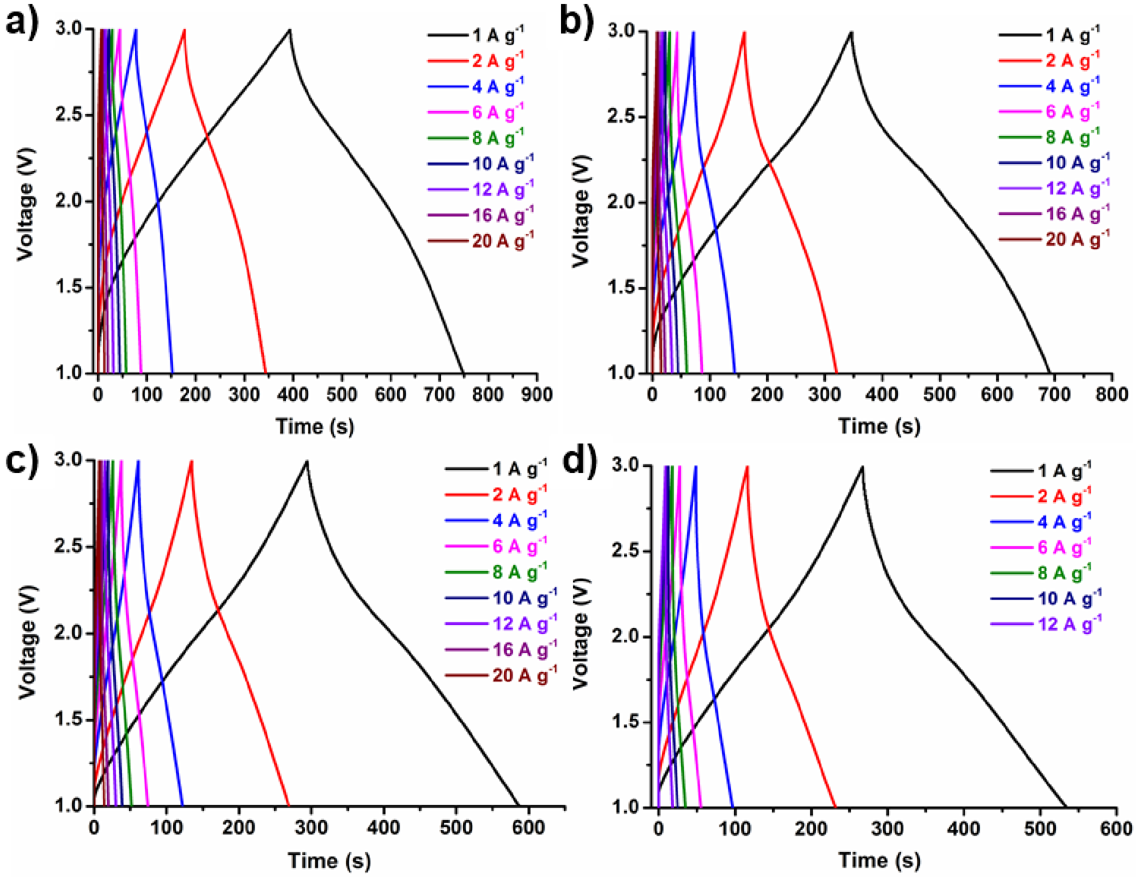

**Figure 5.8** Typical charge/discharge curves of the LIC with AC/CNT cathode and TiO$_2$ nanotube anode with deep pre-lithiation condition: (a-d) Pre-lithiation to 1 6 V, 1.4 V, 1.2 V and 1.0 V respectively.

The lithium storage behavior can be conveniently probed via the CV scan. As shown in Figure 5.9, when the pre-lithiation voltage is 1.6 V, the majority contribution is still from higher voltage range of 2.0-3.0 V. However, as the pre-lithiation goes to 1.4 V and lower, the operation voltage shifts to a lower range of 1.0-2.0 V. Since the total energy is proportional to capacity and voltage, lower operation voltages will lead to less amount of energy, which is undesirable in the LIC cells.

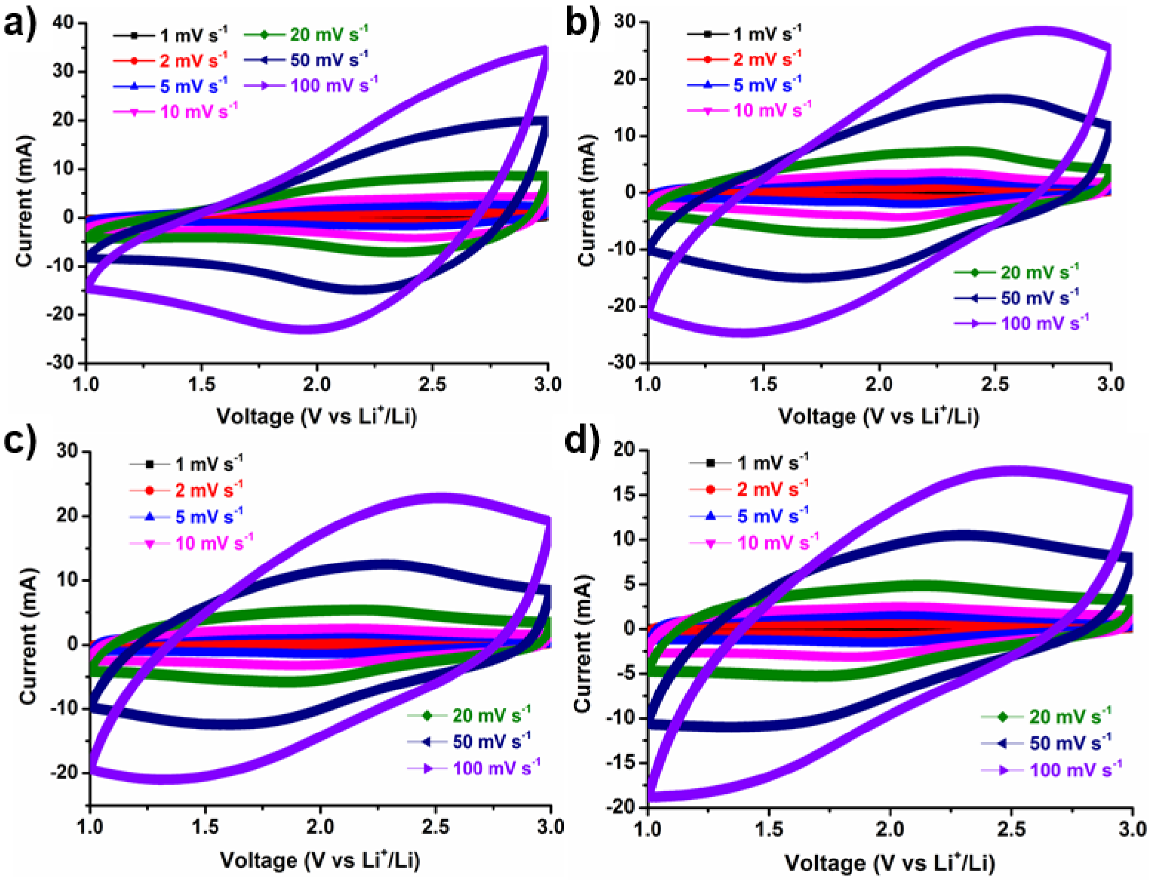

**Figure 5.9** Typical CV curves of the LIC with AC/CNT cathode and $TiO_2$ nanotube anode with deep pre-lithiation condition: (a-d) Pre-lithiation to 1.6 V, 1.4 V, 1.2 V and 1.0 V respectively.

The specific energy in full cell LIC can be calculated via the following equation: [22]

$$E = i\int_{t_1}^{t_2} \mathrm{V(t)dt} \Big/ (3.6 \times m) \tag{5.2}$$

Where E is the specific energy density (Wh $kg^{-1}$), *i* is the discharge current (A), V (t) is the voltage at time *t*, *m* is the total electrode active materials mass ($TiO_2$ and AC/CNT) in gram, and the integration part corresponds to the total area under the discharge voltage curve. The power density is given by:

$$P = E \times 3600 / \Delta t \tag{5.3}$$

Where the unit for power density *P* and time range *Δt* is (W $kg^{-1}$) and (s), respectively. The Ragone plot which summarizes the energy and power density of the LICs with different pre-lithiation condition is shown in Figure 5.10. For the pristine $TiO_2$ nanotube electrode without pre-lithiation, the energy density is 37.3 Wh $kg^{-1}$ at power density of 562 W $kg^{-1}$, while the value decreases to 10.9 Wh $kg^{-1}$ at high power of 4550 W $kg^{-1}$.

Upon pre-lithiation to 2 V, a higher energy density of 45.2 Wh $kg^{-1}$ at similar power density of 532.9 W $kg^{-1}$ can be achieved compared to pristine $TiO_2$. Even at high power of 9.53 kW $kg^{-1}$, an energy density of 16.63 Wh $kg^{-1}$ can be delivered. In fact, the maximum energy can go up to 50.77 Wh $kg^{-1}$ for the samples with pre-lithiation voltage of 1.76 V, and the maximum power density can reach 8.98 kW $kg^{-1}$ at energy density of 20.7 Wh $kg^{-1}$. Upon further lithiation below 1.76 V, the specific energy and power densities of LIC cells decreases gradually, however the effect is more severe when the pre-lithiation voltage goes to 1.0 V, where the energy density reduces to 35 Wh $kg^{-1}$ with low power of 472 W $kg^{-1}$, and the value further drops to 11.8 Wh $kg^{-1}$ at power density of 4.75 kW $kg^{-1}$, which yields no obvious increment compared to pristine $TiO_2$ nanotube electrode. As indicated in Figure 5.8d and 5.9d, the operation voltages drops significantly when the lithiation voltage goes down to 1.0 V, in fact, only limited capacity can be achieved at voltage below 1.0 V for $TiO_2$ materials. Therefore the operation mechanism of such lithiated $TiO_2$ electrode requires further study to unravel.

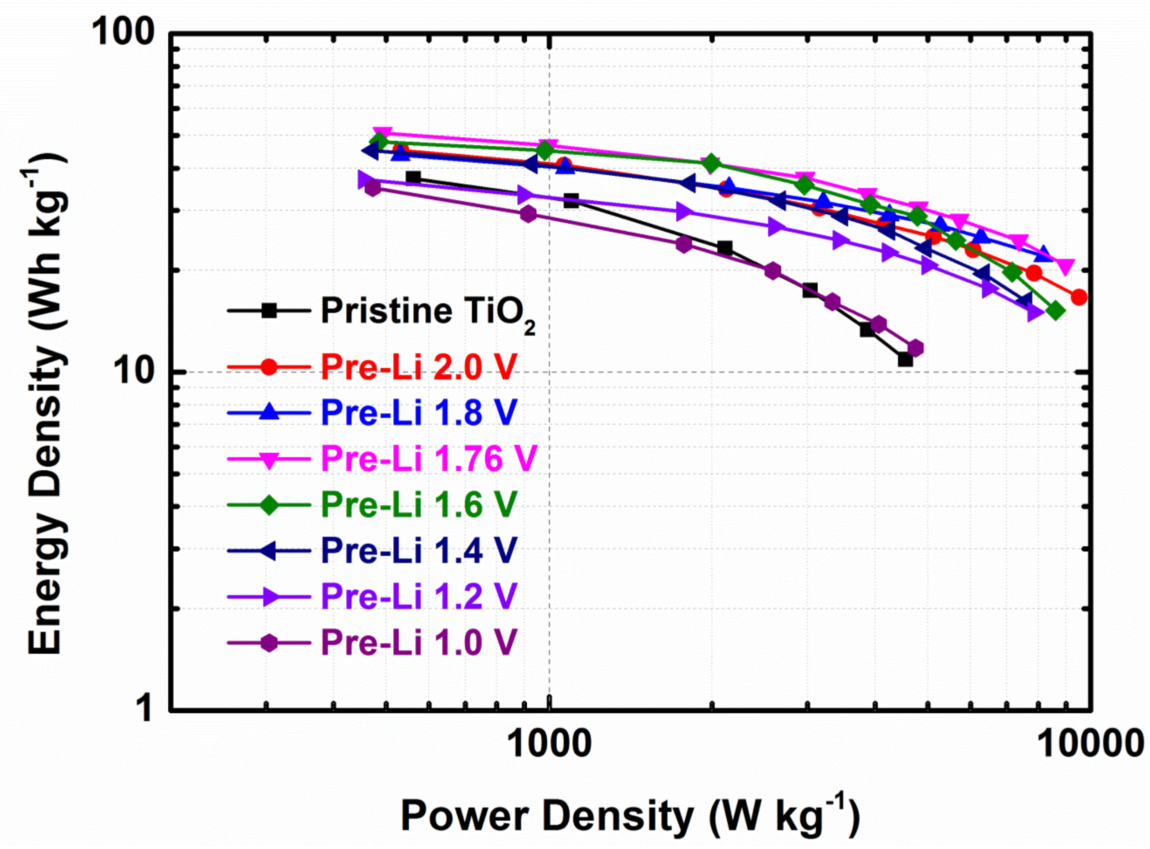

**Figure 5.10** Ragone plot of the LICs with AC/CNT cathode and $TiO_2$ nanotube anode at different lithiation voltage.

### 5.3.4 Operation Mechanism of LICs with Pre-lithiated $TiO_2$ Anode

The pre-lithiation process is expected to improve both electrical conductivity and first cycle Columbic efficiency (CE) of the LIC cells. The *in situ* EIS study (Figure 5.2) verifies that the conductivity indeed increases even upon early lithiation of 2.0 V. To further shed light on the operation mechanism of LIC cells with pre-lithiated $TiO_2$ electrode, the prominent effect of pre-lithiation on CV and CE curves is summarized in Figure 5.11.

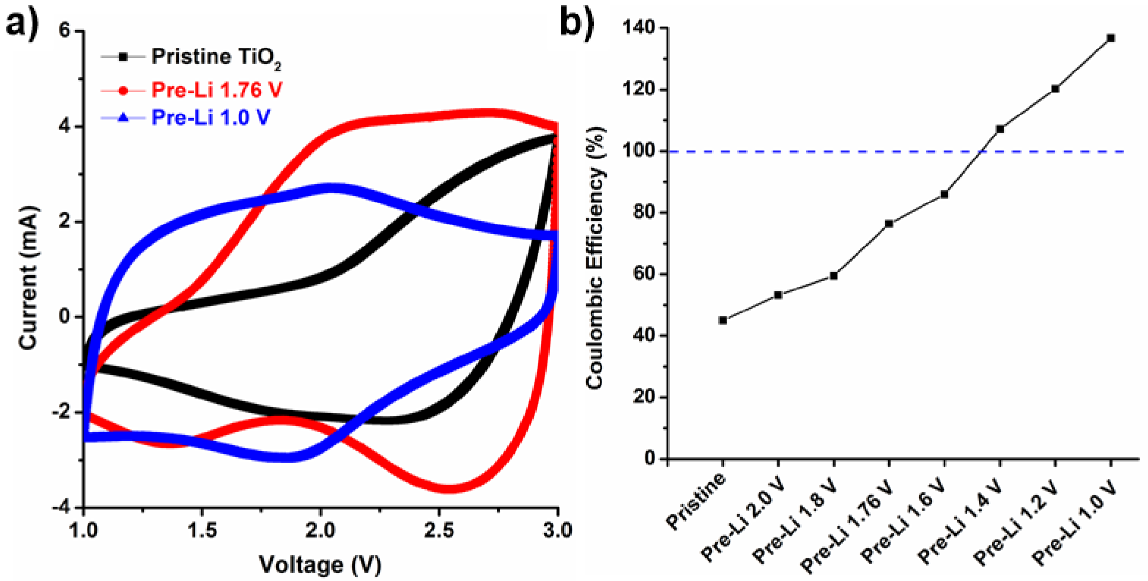

**Figure 5.11** (a) Comparison of the CV curves at scan rate 10 mV $s^{-1}$; (b) Columbic efficiency of the LICs with different lithiation voltage at 1st cycle.

From the CV curve in Figure 5.11a, compared to pristine $TiO_2$ nanotube electrodes, the main reaction takes place at higher voltages (2.0-3.0 V) for the pre-lithiated 1.76 V sample. However, the operation voltages shift to lower range (1.0-2.0 V) when the pre-lithiation process goes down until 1.0 V. Figure 5.11b shows the change of Columbic efficiency (CE) at first cycle. Pristine $TiO_2$ nanotube electrodes suffers from very low CE around 42 %, A gradual increase of the CE value is observed as the pre-lithiation voltage goes lower, which can be rationalize by the fact that certain amount of lithium ions have already been supplied inside the materials during the pre-lithiation process. Of great interest are the samples with pre-lithiation voltage lower than 1.4 V, the first cycle CE has exceeded 100 %, this can only be explained by the fact that the pre-inserted lithium participated in the overall reaction and can be extracted upon lower voltages.[25] In order to prove this hypothesis, the half-cell with AC/CNT cathode and lithium metal anode is fabricated and subjected to galvanic discharge/charge cycles at voltage range of 1.6-3.0 V (The stability window of AC in the EC/DEC electrolyte is 1.0 to 4.4 V).[3] The properties of lithium storage at such voltage range is shown in Figure 5.12, a specific capacity of 41.7, 38.0, 34.2, 28.8 and 26.8 mAh $g^{-1}$ can be delivered at current rate of 0.1, 0.2, 0.4, 0.8 and 1.0 A $g^{-1}$, corresponding to a specific capacitance value of 107.2, 97.7, 87.9, 74.1 and 68.9 F $g^{-1}$, respectively. Although the cation storage capacities in AC/CNT composites are lower than that of the anion storage, the ability to adsorb lithium ions reversibly at voltage lower than 3.0 V opens up new doors for the operation of LICs based on pre-lithiated $TiO_2$ nanotube anode.

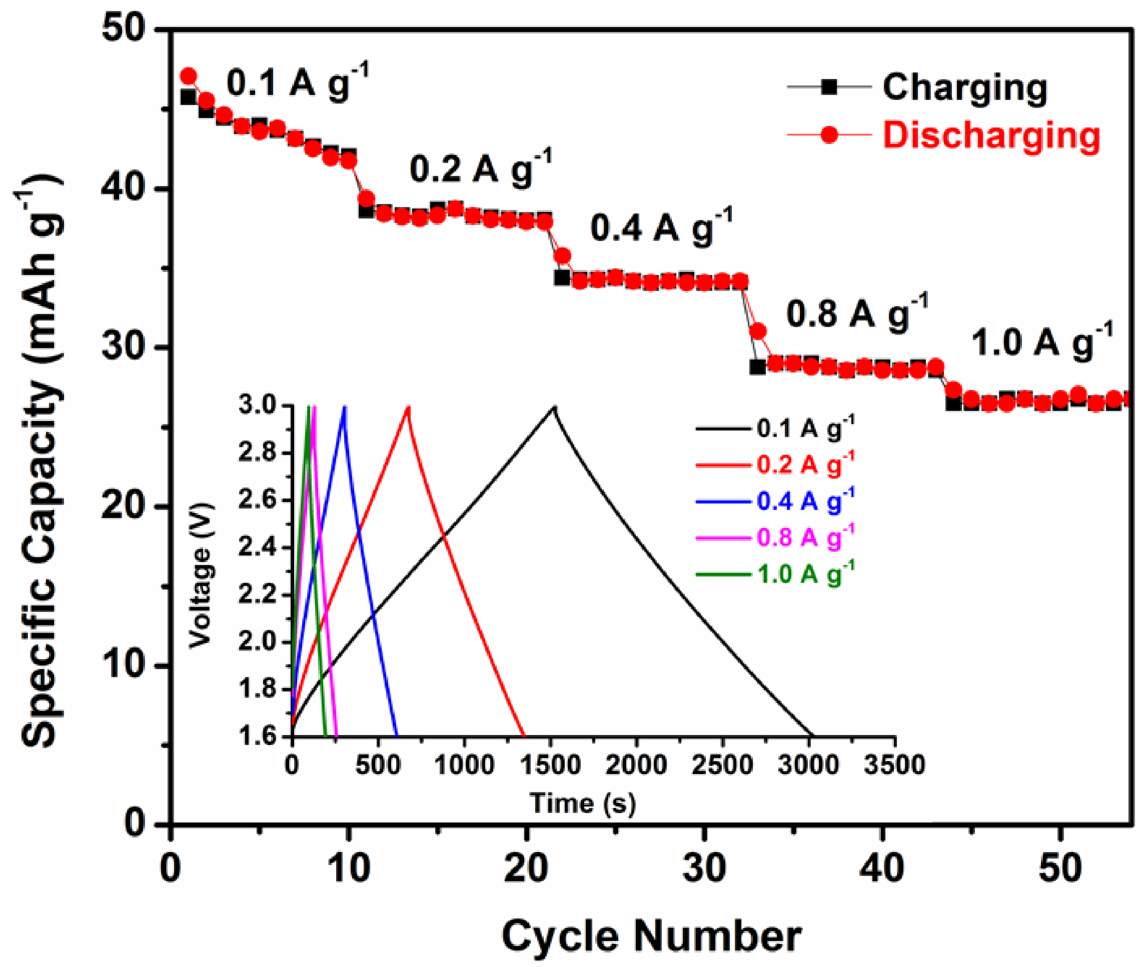

**Figure 5.12** Charge/discharge capacities of the AC/CNT cathode at voltage range of 1.6 to 3 V, inset is the corresponding voltage time profile.

From the above analysis, the operation mechanism of the LIC cells is proposed as shown in Figure 5.13. First of all, certain open-circuit voltage (OCV) of the LIC cells can be built up with the pre-lithiated $TiO_2$ anode; this value depends on the stable voltage of the lithiated $TiO_2$ electrode and the AC/CNT cathode, the OCV of the LIC full cells is around 0.7, 1.12, 1.21, 1.24, 1.36, 1.43 and 1.53 V for the pre-lithiation voltage of 2.0, 1.8, 1.76, 1.6, 1.4, 1.2 and 1.0 V. Upon charging, the lithium ions from the electrolyte will be intercalated into $TiO_2$ structure and the anions will be adsorbed onto the AC/CNT surface until the upper cut-off voltage (3.0 V) is reached. In the discharging process, the inserted lithium ions and adsorbed anions will be removed back to electrolyte, thereafter, the inserted lithium inside $TiO_2$ structure can be shuttled between anode and cathode, which contributes to additional capacity until lower cut-off voltage of 1.0 V. Such dual ion adsorption behavior of AC/CNT cathode improves the overall performances of the LICs.

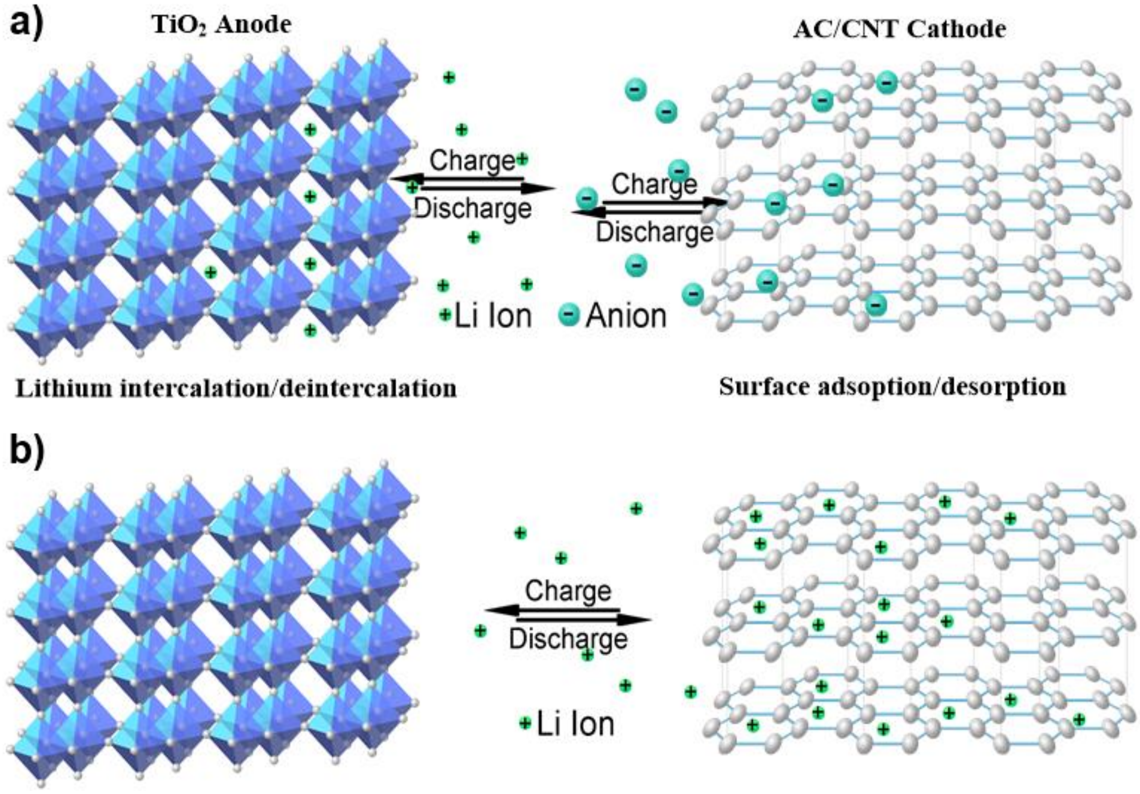

**Figure 5.13** Schematics on the operation mechanism of the LICs with different pre-lithiation voltage: (a) during charging at voltage above OCV, lithium ions from electrolyte are intercalated into the $TiO_2$ structure and anions are adsorbed on the AC/CNT surface; (b) during discharging, when all ions are removed back to electrolyte, the operation only involves pre-inserted lithium ions shuttling between $TiO_2$ anode and AC/CNT cathode.

Finally, the long-term cycling test is carried out for the high power LICs at current rate of 2 A $g^{-1}$ and the results are shown in Figure 5.14. For pristine $TiO_2$ electrode, the capacity drops to below 80% within 100 cycles. In contrary, the LIC with pre-lithiated $TiO_2$ electrodes (1.76 V) could maintain 80% capacity after 3,000 cycles and 73% capacity after 10,000 cycles. Even for the deep pre-lithiated sample (1.0 V), 77% capacity can be retained after 9,600 cycles. These results further prove that the cyclability of LIC with pre-lithiated $TiO_2$ electrode can be improved and the dual ion adsorption mechanism does not deteriorate the cycling performances of the system. Owing to the high voltage and high energy density, one LIC cell can lighten up 40 LEDs (Figure 5.14b).

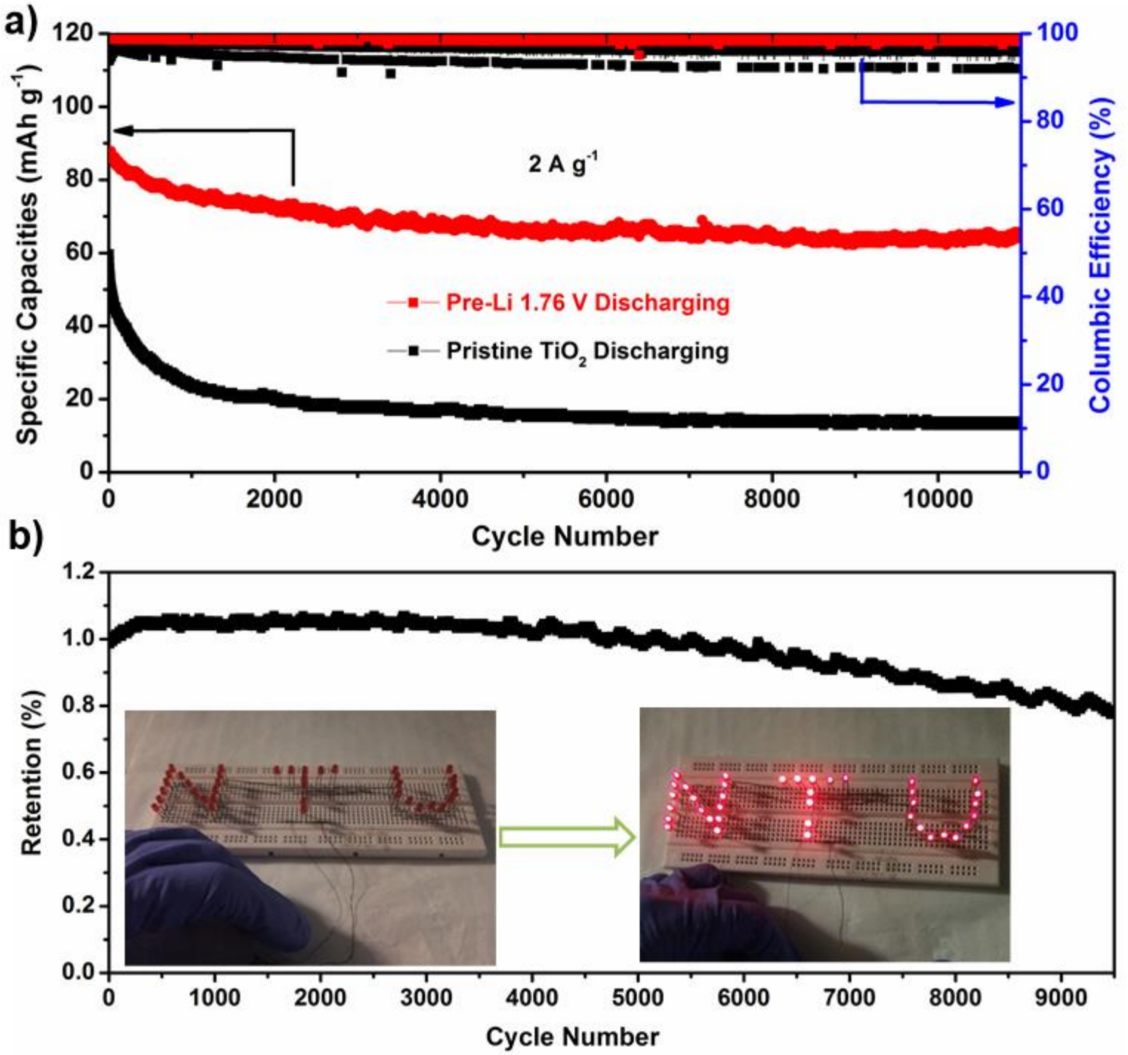

**Figure 5.14** Cycling performances of the LICs with $TiO_2$ nanotube anode at different pre-lithiation voltage: (a) pristine $TiO_2$ and pre-lithiated $TiO_2$ at 1.76 V, (b) pre-lithiated $TiO_2$ at 1.0 V, inset is the digital images of lightening up 40 LEDs with the hybrid capacitor.

## 5.4 Conclusions

In this chapter, high power lithium-ion hybrid capacitors (LIC) are fabricated by AC/CNT cathode coupled with pre-lithiated $TiO_2$ nanotube anode. At optimized condition, a high energy density of 50.77 Wh $kg^{-1}$ can be achieved at power density of 492.6 W $kg^{-1}$ and the maximum power density can reach 8.98 kW $kg^{-1}$ at energy density of 20.7 Wh $kg^{-1}$. The pre-lithiation process improves the electrical conductivity and first cycle Columbic efficiency of the system and enables the dual ion adsorption function of the AC/CNT composite cathode, which not only boosts the overall energy and power density, but also prolongs the cycle life of the LIC cells. As a result, more than 70% of the capacity can be retained after 10,000 cycles at current rate of 2 A $g^{-1}$. The pre-lithiation process is proven to be highly effective to achieve high performance LIC cells based on $TiO_2$ electrode.

## References

[1] I. Plitz, A. DuPasquier, F. Badway, J. Gural, N. Pereira, A. Gmitter, G. G. Amatucci, *Appl. Phys. A* **2006**, *82*, 615.

[2] P. Simon, Y. Gogotsi, *Nat Mater* **2008**, *7*, 845.

[3] K. Naoi, S. Ishimoto, J.-i. Miyamoto, W. Naoi, *Energy Environ. Sci.* **2012**, *5*, 9363.

[4] K. Naoi, W. Naoi, S. Aoyagi, J.-i. Miyamoto, T. Kamino, *Acc. Chem. Res.* **2013**, *46*, 1075.

[5] V. Aravindan, J. Gnanaraj, Y.-S. Lee, S. Madhavi, *Chem. Rev.* **2014**, *114*, 11619.

[6] H. Kim, M.-Y. Cho, M.-H. Kim, K.-Y. Park, H. Gwon, Y. Lee, K. C. Roh, K. Kang, *Adv. Energy Mater.* **2013**, *3*, 1500.

[7] Q. Wang, Z. H. Wen, J. H. Li, *Adv. Funct. Mater.* **2006**, *16*, 2141.

[8] G. Wang, Z. Y. Liu, J. N. Wu, Q. Lu, *Mater. Lett.* **2012**, *71*, 120.

[9] V. Aravindan, N. Shubha, W. C. Ling, S. Madhavi, *J. Mater. Chem. A* **2013**, *1*, 6145.

[10] M. Zukalová, M. Kalbáč, L. Kavan, I. Exnar, M. Graetzel, *Chem. Mater.* **2005**, *17*, 1248.

[11] A. G. Dylla, G. Henkelman, K. J. Stevenson, *Acc. Chem. Res.* **2013**, *46*, 1104.

[12] V. Aravindan, Y.-S. Lee, S. Madhavi, *Adv. Energy Mater.* **2015**, *5*, 1402225.

[13] M. Fehse, E. Ventosa, *ChemPlusChem* **2015**, *80*, 785.

[14] H. Liu, Z. Bi, X. G. Sun, R. R. Unocic, M. P. Paranthaman, S. Dai, G. M. Brown, *Adv. Mater.* **2011**, *23*, 3450.

[15] S. Liu, H. Jia, L. Han, J. Wang, P. Gao, D. Xu, J. Yang, S. Che, *Adv. Mater.* **2012**, *24*, 3201.

[16] Y. Ren, Z. Liu, F. Pourpoint, A. R. Armstrong, C. P. Grey, P. G. Bruce, *Angew. Chem. Int. Ed.* **2012**, *51*, 2164.

[17] S. Liu, Z. Wang, C. Yu, H. B. Wu, G. Wang, Q. Dong, J. Qiu, A. Eychmuller, X. W. David Lou, *Adv. Mater.* **2013**, *25*, 3462.

[18] V. Etacheri, J. E. Yourey, B. M. Bartlett, *ACS Nano* **2014**, *8*, 1491.

[19] C. Jiang, M. Wei, Z. Qi, T. Kudo, I. Honma, H. Zhou, *J. Power Sources* **2007**, *166*, 239.

[20] Y. Ren, L. J. Hardwick, P. G. Bruce, *Angew. Chem. Int. Ed.* **2010**, *122*, 2624.

[21] S. Brutti, V. Gentili, H. Menard, B. Scrosati, P. G. Bruce, *Adv. Energy Mater.* **2012**, *2*, 322.

[22] S. Zhang, N. Pan, *Adv. Energy Mater.* **2015**, *5*, 1401401.

[23] A. Banerjee, K. K. Upadhyay, D. Puthusseri, V. Aravindan, S. Madhavi, S. Ogale, *Nanoscale* **2014**, *6*, 4387.

[24] H. Wang, Y. Zhang, H. Ang, Y. Zhang, H. T. Tan, Y. Zhang, Y. Guo, J. B. Franklin, X. L. Wu, M. Srinivasan, H. J. Fan, Q. Yan, *Adv. Funct. Mater.* **2016**, *26*, 3082.

[25] H. Li, L. Cheng, Y. Xia, *Electrochem. Solid-State Lett.* **2005**, *8*, A433.

# Chapter 6

## Fast Charging High Energy $TiO_2$-based Lithium-ion Batteries Enabled by Water-soluble Sericin Binder

*In this chapter, high energy LIBs based on dual phase* $TiO_2$ *nanotube anode and high voltage* $LiNi_{0.5}Mn_{1.5}O_4$ *(LNMO) cathode was fabricated. A water-soluble sericin binder was utilized on the cathode preparation process and serves as passivation layer to prevent excessive oxidation of the electrolyte. Full cell battery with dual phase* $TiO_2$ *nanotube anode could deliver a high energy density of 687.6 Wh* $kg^{-1}$ *at power density of 957.6 W* $kg^{-1}$*(based on* $TiO_2$ *mass). Furthermore, such battery could maintain 80% of original capacity after 1,000 cycles at 10 C, indicating the excellent stability of the* $TiO_2$ *nanotubes and the sericin binder.*

## 6.1 Introduction

Development of high energy density lithium-ion batteries (LIBs) with high power capabilities is highly desirable for applications in electric vehicles and grid energy storage.[1-3] Although dual phase $TiO_2$ materials feature high power characteristics with long cycle life, the lithiation potential is very high at around 1.5-1.7 V, which leads to low energy density when coupled with normal cathode materials operated at around 4 V.[4, 5] To improve the overall energy density of the $TiO_2$ based LIBs, one effective approach is to increase the operating voltage of batter cells as energy is proportional to both capacity and voltage.[6, 7] In such regards, spinel $LiNi_{0.5}Mn_{1.5}O_4$ (LNMO) has been widely studied as promising cathode candidates owing to its high voltage (~ 4.75 V), low cost and high power characteristics.[8-10] However, the operating voltage falls out of the stability window (~ 4.5 V) of conventional electrolytes based on $LiPF_6$ in alkyl carbonate solvents, leading to oxidation of the electrolyte and formation of the passivating surface films, called solid electrolyte interphase (SEI).[11, 12] Unlike the SEI formed in graphite anode, the cathode SEI is not stable and grows continuously during cycling which leads to high impedance of the cell with inferior rate capabilities. To alleviate such problems and achieve fast charging performances in LNMO, artificial barriers between electrolyte and LNMO needs to be created against electrolyte oxidation, attempts have been made with inorganic oxides such as ZnO,[13] $TiO_2$[14] and $Al_2O_3$[15] for surface coating. Although effective in alleviating the side reactions with electrolyte, these inorganic coating suffer from incomplete surface coverage and lead to poor rate performances due to limited lithium ion conductivity. Even though more uniform coatings can be achieved by atomic layer deposition (ALD) or by conductive polymers,[16] these coatings fail to address the reactivity of carbon black additives in electrode formulation, which tends to cause solvent co-intercalation at high voltages.[17, 18] Thus novel design on the whole electrode level covering both active LNMO materials and conductive carbon additives is required to stabilize the SEI and achieve high rate performances.

In such regards, auxiliary binders become important as they interact closely with active particles and conductive carbons to ensure good electrical and mechanical contact.[19] Conventional polyvinylidene fluoride (PVDF) binder has long chain structure, which functions via weak physical adsorption and often fails to provide sufficient surface interactions, resulting in poor surface coverage with the active materials and conductive carbons.[20] To achieve better surface coverage and excellent electrochemical stability, efforts in searching for alternative binders have shifted attention from weak physical adsorption towards strong chemical binding, where water-soluble binders functionalized with surface active groups such as carboxyl and hydroxyl groups are developing extensively.[21-25] Since lithium ions have to penetrate through the passivation film to reach the active materials surface, amorphous molecules with abundant surface binding sites and porous pathway for lithium ion transfer are highly preferred.[26-29] In such regards, protein macromolecules with hierarchical structures serve as great platform. In particular, sericin protein is expected to be a superior binder candidate due to the following reasons: first of all, sericin is a natural adhesive protein, which holds fibroin filament together forming continuous strands of silk; the intrinsic adhesive property makes it plausible for binder application. Secondly, sericin is composed of 18 amino acids, of which 45.8% contains hydroxyl group.[30] A higher content of hydroxyl group endows the material with a larger number of possible reaction sites with active materials to improve the binding property. Thirdly, as a water soluble protein, sericin exists mainly in amorphous random coil structure with porous pathways for ion transfer.[31] Fourthly, sericin is resistive to oxidation, previous study has demonstrated no oxidation/reduction peaks for sericin film as resistance switching devices;[32] the electrochemical stability renders it applicable to high voltage electrode. Finally, it should be noted that sericin is abundant and widely available, annual production of silk will generate more than 50,000 tons of dry sericin, most of which are discarded in wastewater during raw silk production process.[30] Therefore the cost is minimal and recovery of such waste materials will lead to significant economic and social benefits.

In this work, we demonstrate the application of sericin as effective binder materials for high voltage LNMO cathode. A stable surface passivation layer can be formed with the assistance of the sericin binder, so that the rate performances of the LNMO cathode improve over the PVDF binder. A capacity of 91.2 mAh $g^{-1}$ can be delivered at 5 C with sericin binder, compared to 28.1 mAh $g^{-1}$ delivered by PVDF binder. Full cell LIBs utilizing $TiO_2$ nanotube anode and LNMO cathode passivated by sericin binder also demonstrates good rate performances with high energy density and excellent cyclability. These results verify the feasibility of sericin as effective water soluble binder for fabrication of high energy $TiO_2$-based lithium-ion batteries (LIBs).

## 6.2 Experimental Methods

### 6.2.1 Synthesis

Commercial $LiNi_{0.5}Mn_{1.5}O_4$ micro-particles and acetylene black (AB) (Sigma-Aldrich Inc) were used as the active material and conductive agent for the composite electrode without further treatment. Different binders were investigated in the experiment: silk sericin binder was purchased from Aotesi Biochemicals Co. Ltd (Huzhou, China), which were hydrolyzed sericin peptides with the molecular weight of ~100 kDa. Sericin aqueous solution were obtained through dispersing homogeneously a certain amount of sericin in distilled water with stirring at 60 °C for 1 h. Conventional Poly(vinylidene fluoride) (PVDF) (Sigma-Aldrich Inc ) was used as control binder, and solution was obtained by dissolving a certain amount of PVDF powder in N-methyl-2-pyrrolidone (NMP, Sigma-Aldrich, anhydrous, 99.5%).

### 6.2.2 Characterization

Mechanical tests of these films were conducted in ambient air using a fully automated nanomechanical test system (TI950 Triboindenter; Hysitron Minneapolis, MN). Normal indentation tests were performed by using a conical diamond indenter with a 1 μm tip radius. The maximum load during indentation was 400 μN. Hardness and Young's modulus was calculated from the unloading portions of the load-displacement curves following established process. Eight microstructural domains had been selected for every sample in the experiment. Morphologies of the active materials and the battery electrodes are observed by using field emission Scanning Electron Microscopy (FESEM, Zeiss Supra 55). X-ray diffraction data were obtained by Bruker 6000 X-ray diffractometer using a Cu Kα source.

### 6.2.3 Electrochemical Analysis

For the preparation of working $LiNi_{0.5}Mn_{1.5}O_4$ cathodes, active materials (80 wt %) and conductive agent (10 wt %) were thoroughly mixed with binders (10 wt %). The black slurry thus obtained was cast onto a sheet of aluminum foil. The electrodes were dried at 60 ℃ in vacuum overnight to remove residual solvent. Electrochemical properties were investigated using 2032 type coin cells assembled inside Ar-filled glove box with $O_2$ and $H_2O$ contents typically below 0.6 ppm. The organic electrolyte with 1.0 M $LiPF_6$ dissolved in a mixture of ethylene carbonate and diethyl carbonate (EC: DEC, 1:1 by weight) was used for both half cells and full cells. Galvanic cycling tests of the batteries were performed with NEWARE battery analyzer. Cyclic voltammetry (CV) study and *in situ* EIS measurements during the discharging process were conducted with the Solartron electrochemical workstation. During impedance measurement, a sinusoidal wave with amplitude of 10.0 mV was applied to the cell over the frequency range 100 kHz-0.1 Hz. The loading density of cathode materials is around 1.0 mg $cm^{-2}$.

## 6.3 Principle Outcomes

### 6.3.1 Properties of Sericin Binder

As shown in Figure 6.1a, the sericin molecule is derived from silk cocoon, where it holds together the fibroin filament to form continuous strands of silk. The majority amino acid in sericin is serine, whose structure contains additional sidechain hydroxyl groups. In this study, the properties of sericin with molecular weight of 100 kDa (denoted as S100k) are investigated first with commercial PVDF (molecular weight 534 kDa) as reference. As shown in Figure 6.1c, the viscosity of PVDF and S100k solution are 4.64 cP (centipoise) and 5.01 cP for 1 wt % solution, which increases to 10.63 cP and 11.8 cP for 2 wt % solution. Although with lower molecular weight, the viscosity of the S100k binder exceeds that of PVDF owing to its abundant hydroxyl group and strong interaction with water. In fact, the S100k solution (2 wt %) will form hydrogel when settled in ambient temperature for several hours (Figure 6.1b). A suitable viscosity helps the formation of stable electrode with good adhesion towards active materials, conductive carbon and current collector. In terms of mechanical properties, the Young's modulus and hardness of PVDF and sericin films were probed via nanoindentation technique (Figure 6.1d). In a dry state, the sericin film exhibited better stiffness compared with PVDF film. Elastic modulus and hardness for S100k film are 8.66 and 0.45 Gpa, far exceeding the values for PVDF film, which are only 2.14 and 0.19 GPa. The better rigidity and film formation property of S100k binder is very important for retaining the stability of the SEI layer and the structural integrity of the entire electrode. It should be noted that although the mechanical property is strong, sericin is mainly amorphous in nature, therefore the diffusion of lithium ions will not be hindered significantly.

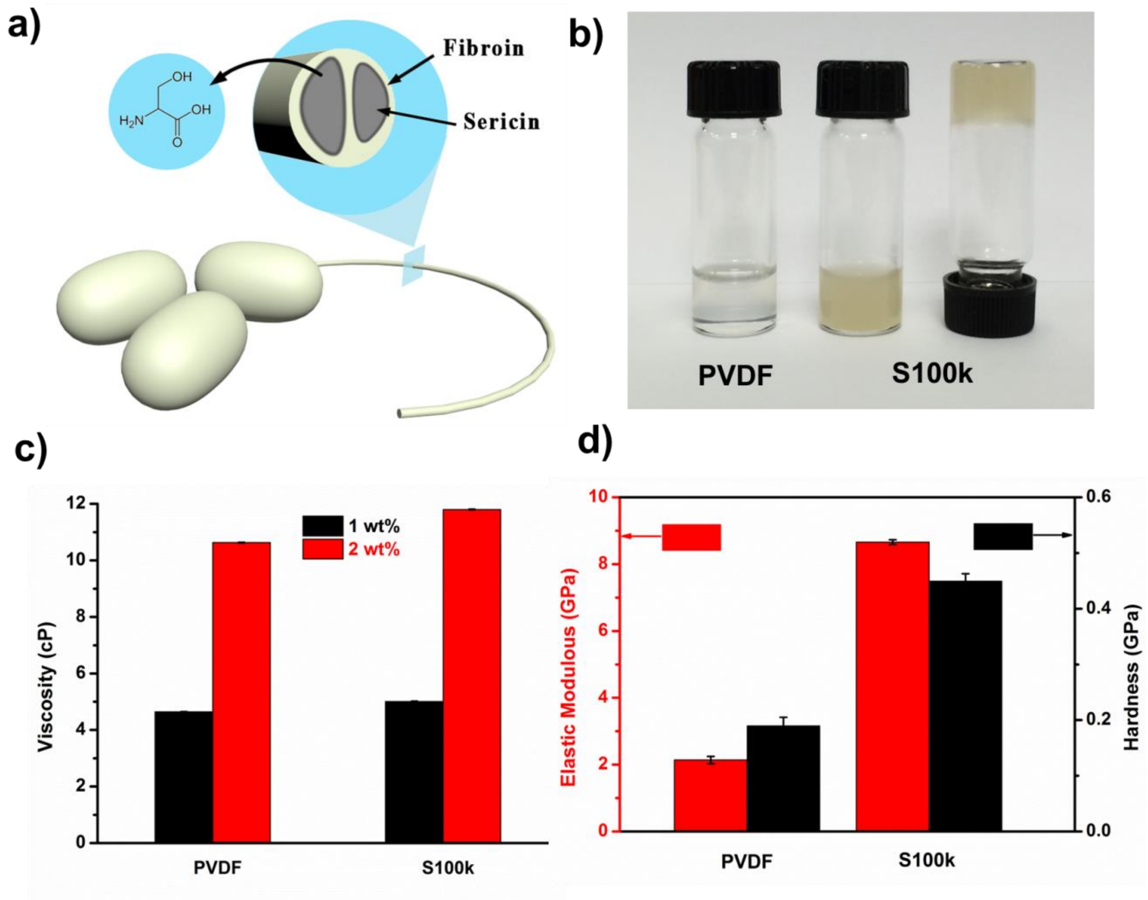

**Figure 6.1** Properties of sericin: (a) Scheme for the production of sericin from cocoon, sericin is wrapped around fibroin and its majority amino acid is serine (b) Digital images of 2 wt% PVDF and sericin solution; (c) Viscosity of PVDF and S100k binder in solution; (d) Elastic modulus and hardness of PVDF and S100k film at dry state.

### 6.3.2 Performances of High Voltage Cathode with Sericin Binder

To verify the feasibility of the sericin as binders in lithium-ion batteries (LIBs), half cell (2032) with metallic lithium as counter and reference electrode is employed to evaluate the electrochemical performances of $LiNi_{0.5}Mn_{1.5}O_4$ (LNMO) materials with PVDF and sericin binder. The water soluble nature of sericin protein is expected to promote interaction of the binder with metal oxide materials and improve the overall surface film stability and enhance battery performances. Indeed, as shown in Figure 6.2a, when LNMO is used as cathode and cycled at current rate of 1 C (140 mA $g^{-1}$), the electrode with PVDF binder only delivers discharge capacity of 90.2 mAh $g^{-1}$ after 100 cycles, with average overall Columbic efficiency of 98.7 %, while electrode with S100k binder delivers much higher capacity of 105.8 mAh $g^{-1}$, and the overall Columbic efficiency is increased to 99.2 %. In addition, the electrodes with S100k binder also exhibit good rate capability at various current densities between 0.5 C to 20 C (Figure 6.2b). A capacity of 128.3, 120.2, 110.3, 91.2, 68.4 and 27.2 mAh $g^{-1}$ is observed for LNMO electrode with S100k binder at current rate of 0.5, 1, 2, 5, 10 and 20 C respectively. Considering that the active materials LNMO is in micro-meter size and is used without any prior treatment, such excellent high rate performances proves the superior property of sericin binder. Compared to S100k binder, electrodes with PVDF binder only delivers capacity of 111.3, 105, 92.6, 28.1 mAh $g^{-1}$ at rate of 0.5, 1, 2 and 5 C. When cycled at higher current rate of 10 and 20 C, the battery dies with virtually no capacity. The charge/discharge voltage profile for at different current rates with S100k binder are shown in Figure 6.2c and the corresponding polarization value is summarized in Figure 6.2d. A linear relationship with the current rates is observed for the polarization value, indicating an ohmic behavior of both electrodes. At all current densities, electrode with S100k binder exhibits low polarization. The voltage polarization for PVDF binder is 0.091, 0.16, 0.26 and 0.52 V at current rate of 0.5, 1, 2 and 5 C. While much smaller value is observed for S100k binder, at rate of 5 C, the polarization is only 0.17 V; even at extremely high rate of 20 C, the polarization is only 0.48 V. Such low polarization renders the electrodes with better rate performances.

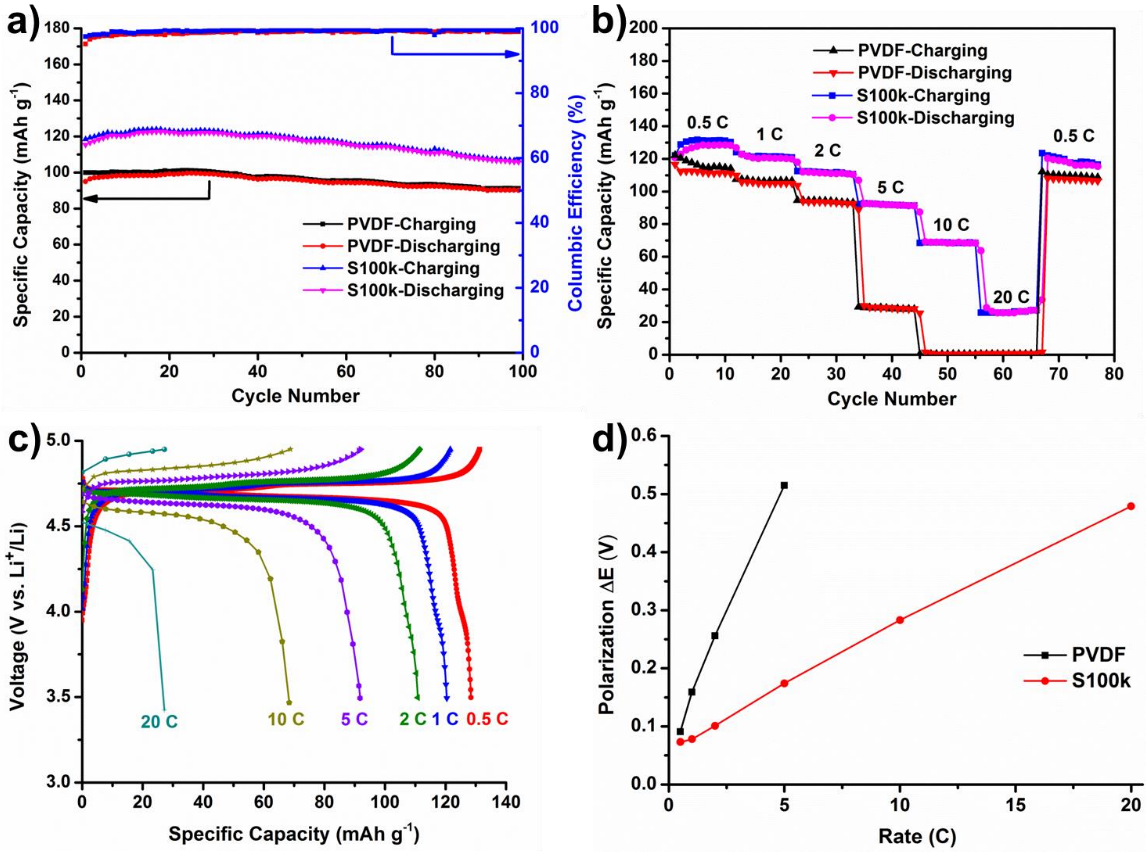

**Figure 6.2** Electrochemical properties of $LiNi_{0.5}Mn_{1.5}O_4$ electrode with PVDF and S100k binder: (a-b) Cycling performances at 1 C and different C-rates, 1 C = 140 mA $g^{-1}$. (c) The corresponding charge-discharge voltage profiles of S100k binder at different current rates. (d) Potential polarization between charge and discharge plateaus at different rates (points are taken at half capacity).

To further probe the stability of the surface passivation layer (SEI), cell impedance was measured at different cycles and the results are compared in Figure 6.3. For PVDF binder, the resistance of the SEI layer (originated from oxidation of the electrolyte) is as large as 242.3 Ω at 5th cycle. Even after 20 cycles, the resistance is still as high as 250.5 Ω; such large resistance of the surface passivation film will hinder the fast lithium reaction and results in poor high rate performances. Whereas for S100k binder, the resistance of the SEI layer is much smaller (65.8 Ω after 5 cycles), and it decreases with cycling and reaches as low as 21.7 Ω after 20 cycles, thus indicating formation of stable surface protection layer. Furthermore, the charge transfer resistance at 5th cycle is 259.2 Ω for PVDF and 242.9 Ω for S100k. after 20 cycles, this value decreases to only 107.3 Ω for

S100k binder, which is much smaller than that of PVDF binder (215.3 Ω), indicating the fast pathways for both electrons and lithium ions.

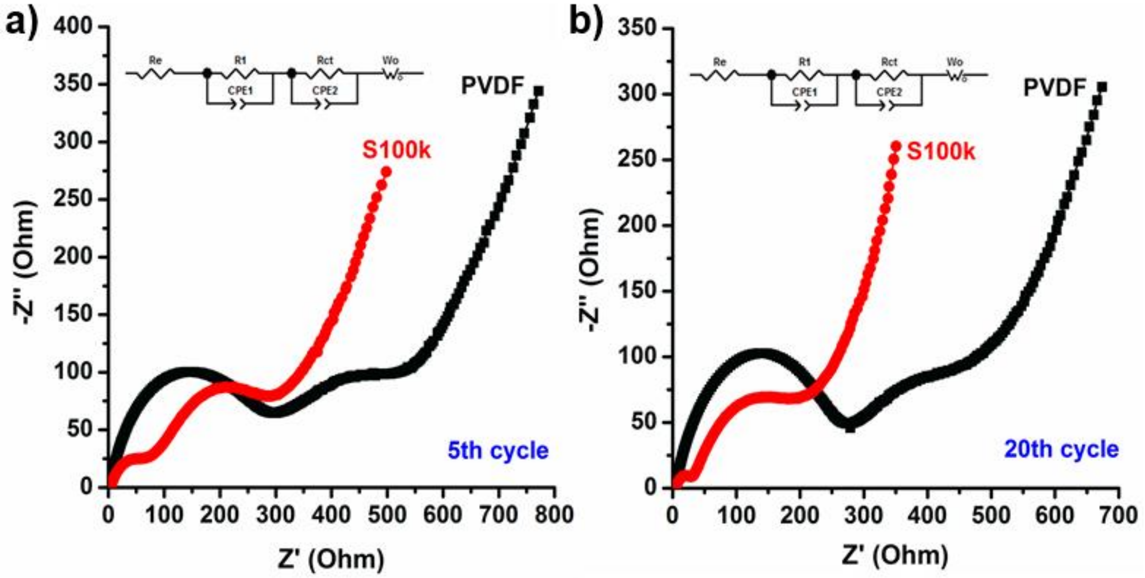

**Figure 6.3** Nyquist plots of the LNMO half-cells with different binders at different cycles: (a) 5th cycle; (b) 20th Cycle. Cycling current rate is 1 C.

To further shed light on the role of sericin binder, the morphologies of the composites electrode before and after cycling are probed; SEM images of the $LiNi_{0.5}Mn_{1.5}O_4$ electrode before and after 100 cycles are shown in Figure 6.4. Figure 6.4a shows the morphologies of the pristine LNMO particles, these particles are not uniform in size, some are in range of several micrometer. Figure 6.4b shows the surface morphologies when mixing with conductive carbon and PVDF binder. Since PVDF binder has linear long chain structure, the interaction with other electrode components are mainly Van der Waals forces, therefore the surface coverage with $LiNi_{0.5}Mn_{1.5}O_4$ is poor, and majority of the particles exposed their surfaces to the electrolyte, which is subjected to electrolyte oxidation during cycling. Therefore, after 100 cycles, although the active materials are covered with a surface layer, the particles are still largely exposed and might subject to further electrolyte oxidation (Figure 6.4c). In contrary, sericin can form porous and less compact film owing to the dominating amorphous random coil structure. Together with abundant surface hydroxyl group to interact with the $LiNi_{0.5}Mn_{1.5}O_4$ materials, the surface coverage with active metal oxide materials is expected to be high. Indeed, the initial coverage for the $LiNi_{0.5}Mn_{1.5}O_4$ cathode is significantly improved before cycling, the particles are more coherent to form smooth film with no large particles exposed (Figure 6.4d). Such protection of S100k film will alleviate the oxidation of the active materials towards electrolyte, thus delivering higher capacity than the PVDF binder. Owing to the better stabilizing effect of the S100k binder, the electrode still maintain its integrity even after 100 cycles, the active materials are emerged with more continuous surface protection SEI layer (Figure 6.4e).

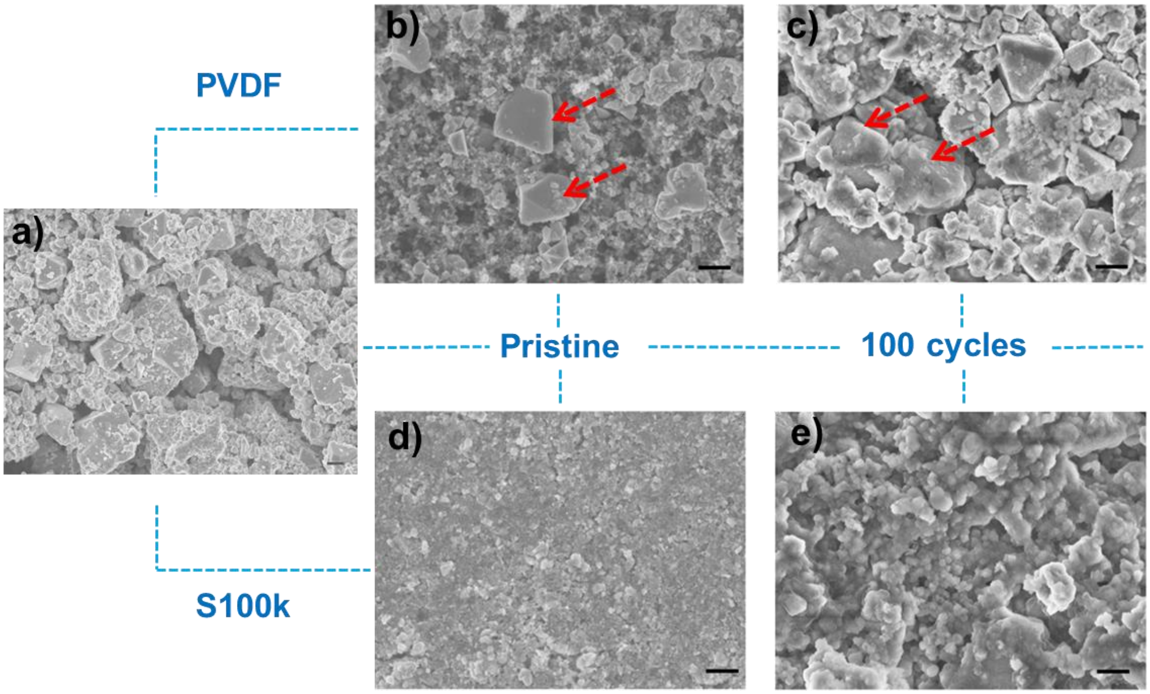

**Figure 6.4** SEM images of the samples: (a) pristine LNMO microparticles; (b) (c) the composite electrode with PVDF binder before cycling and after 100 cycles; (d) (e) the composite electrodes with sericin binder before cycling and after 100 cycles. Scale bar: 1μm.

Based on the above analysis, we propose the working mechanism of the sericin binder as follows. First, owing to the abundant surface hydroxyl groups, the binding strength of sericin binder is strong to maintain good mechanical and electronic integrity of the electrode. Second, the abundant surface binding sites promotes coverage on the surface of active materials to facilitate stable SEI formation for long-term cycling of the battery. Third, the amorphous structure of sericin retain porous pathway for lithium ion transport, which facilitates high rate performances of the active materials. Combining these advantages together, good performances of the high voltage LNMO materials can be achieved with the sericin binder.

### 6.3.3 Performances of Full Cell LIBs Based on $TiO_2$ Anode and LNMO Cathode

With the excellent performances of the LNMO cathode achieved by integration with sericin binder, the full cell LIBs based on dual phase $TiO_2$ anode and LNMO cathode was fabricated and the performances was evaluated. The cyclic voltammetry (CV) of the full cells are shown in Figure 6.5. There are three peak pairs with both PVDF and sericin binder, the peak pair at lower voltage range 2.7/3.0 V corresponds to the reaction in anatase phase, while the peaks pairs at higher voltage range 3.05/3.2 V and 3.2/3.3 V corresponds to the reaction of $TiO_2$ (B) phase. Compared with PVDF binder, electrodes with sericin binder has much lower polarization effect at higher scan rates above 1 mV $s^{-1}$. The charge voltage with sericin binder is still visible and lower than 3.5 V at 2 mV $s^{-1}$, again reflecting the excellent protection function of the stable passivation layer formed with assistance of the sericin binder.

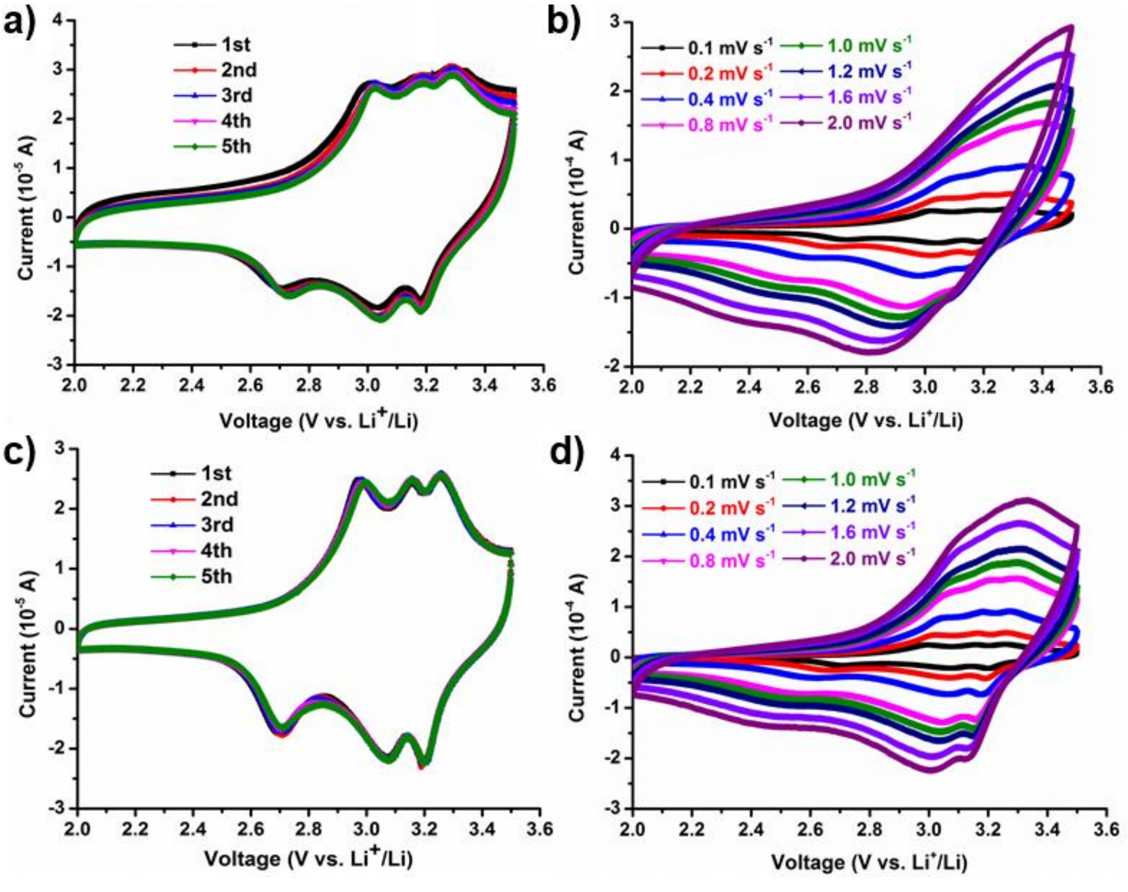

**Figure 6.5** CV curves of full cell batteries with $TiO_2$ anode and LNMO cathode: (a) (b) PVDF binder (c) (d) Sericin binder. Scan rate in (a) and (c) is 0.1 mV $s^{-1}$.

Figure 6.6 shows the discharge capacities of the full cell LIBs based on dual phase $TiO_2$ anode and LNMO cathode. At low current rate of 1 C, the contribution from both anatase (Voltage plateau at ~ 2.7 V) and $TiO_2$ (B) can be observed, as the rate increases, the capacity contribution from the $TiO_2$ (B) phase is dominating since it features pseudocapacitive behavior with fast diffusion kinetics. With PVDF binder, the full cell battery delivers capacity of 205.6, 180.6, 146.8, 76.3 and 37.2 mAh $g^{-1}$ at 1, 2, 4, 10 and 20 C, respectively, whereas for sericin binder, higher capacities of 240.9, 215.4, 183.2, 127.7 and 85.8 mAh $g^{-1}$ are delivered. The highest energy density of the full cell with sericin binder can reach 687.6 Wh $kg^{-1}$ at power density of 957.6 W $kg^{-1}$. At higher power of 18.26 kW $kg^{-1}$, the energy density is still 233.4 Wh $kg^{-1}$, much higher than that of the PVDF binder (89.7 Wh $kg^{-1}$). Such excellent performances further demonstrate the versatility of the sericin binder in high energy LIBs.

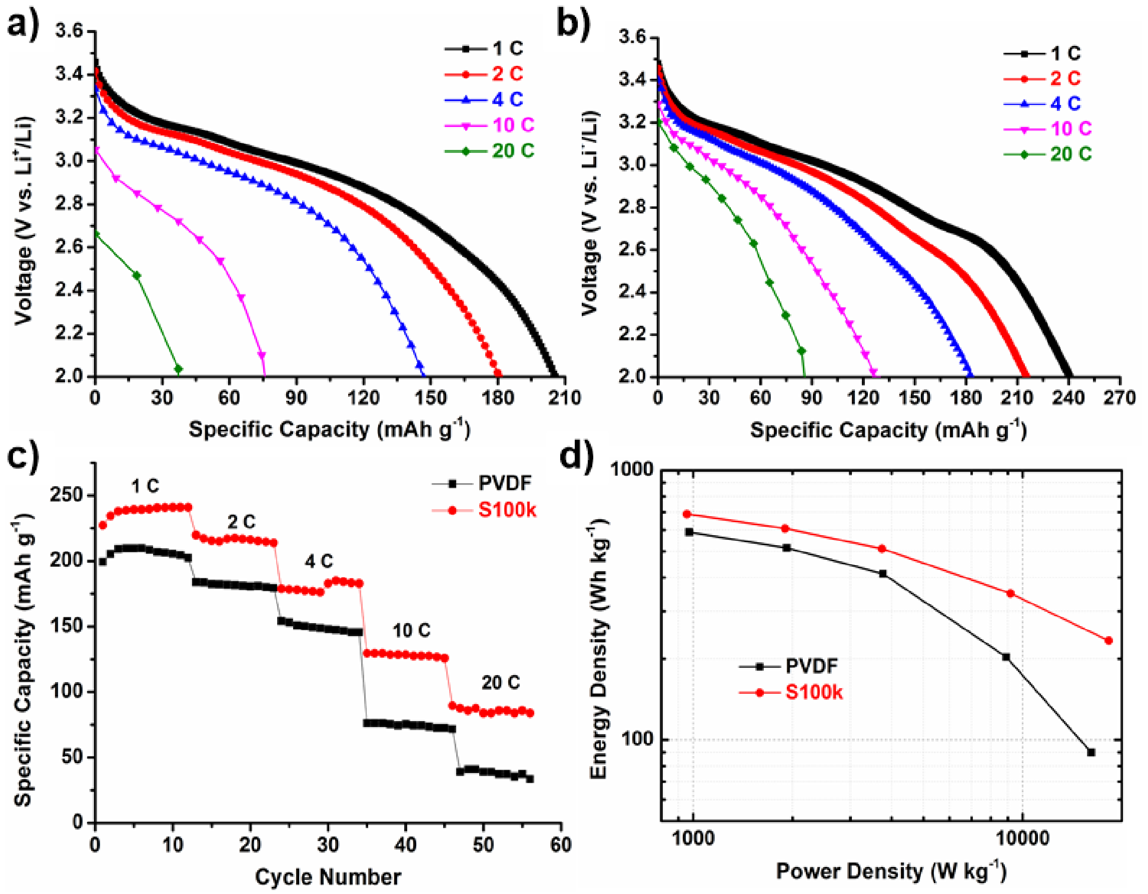

**Figure 6.6** Performance of the full cell LIBs with $TiO_2$ anode and LNMO cathode: Discharge voltage profiles with (a) PVDF binder and (b) sericin binder; (c) Discharge capacities at different current rates (1 C = 335 mA $g^{-1}$); (d) Ragone plot of the full cells (based on $TiO_2$ anode mass).

Finally, the stability of the sericin binder is evaluated by long term cycling of the full cells at high current rate of 10 C (Figure 6.7). After 1,000 cycles, LIB cell with PVDF binder only delivers a capacity of 24.3 mAh $g^{-1}$, with the Columbic efficiency (CE) fluctuating. With sericin binder, higher initial capacity of 128.6 mAh $g^{-1}$ is delivered. Even after 1,000 cycles, the capacity still maintain at 100.6 mAh $g^{-1}$ with more than 80 % retention, proving the long term stability of the sericin binder.

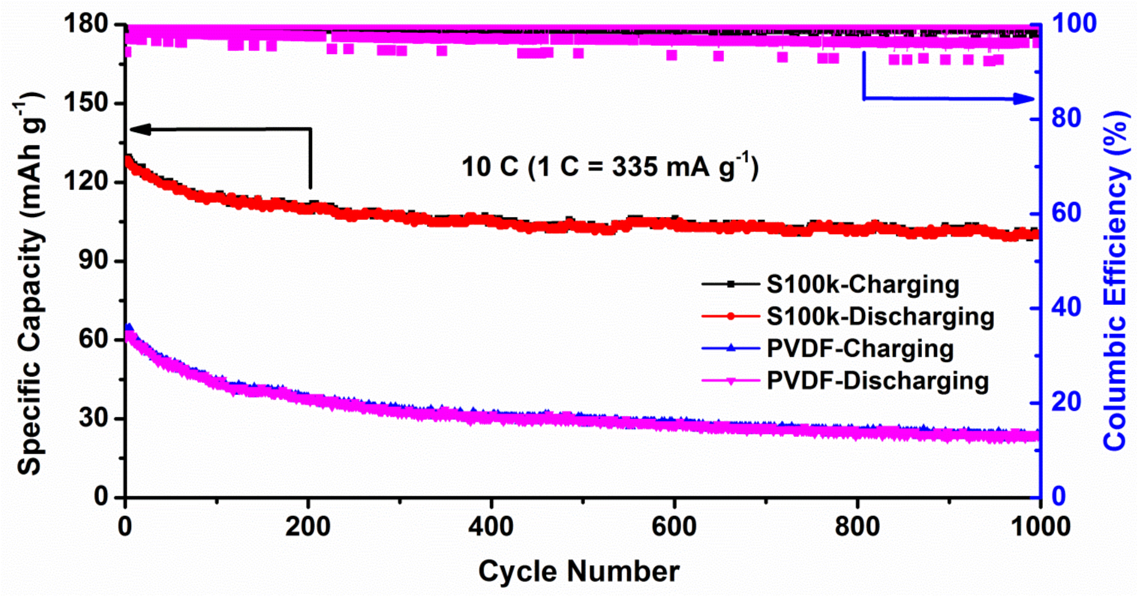

**Figure 6.7** Long-term cycling performance of the full cell LIBs with PVDF and sericin binder.

## 6.4 Conclusions

In this work, we demonstrate the application of sericin as effective binder material for fabrication of high energy LIB cells with $TiO_2$ anode. A stable surface passivation layer can be formed with the assistance of the sericin binder, so that the rate performances of high voltage LNMO cathode improve over the PVDF binder. Full cell LIBs utilizing $TiO_2$ nanotube anode and LNMO cathode demonstrates excellent performances, an energy density of density of 687.6 Wh $kg^{-1}$ at power density of 957.6 W $kg^{-1}$ (based on $TiO_2$ mass) can be achieved. At high power density of 18.26 kW $kg^{-1}$, the energy can still maintain at 233.4 Wh $kg^{-1}$. Furthermore, the full cell could be cycled at 10 C for 1,000 cycles and the capacity of the $TiO_2$ materials still maintain 100.6 mAh $g^{-1}$, indicating the long-term stability of $TiO_2$ nanotubes and sericin binder. The water soluble sericin materials are promising binder candidates for fabrication of high energy LIB cells.

## References

[1] B. Dunn, H. Kamath, J.-M. Tarascon, *Science* **2011**, *334*, 928.

[2] V. Etacheri, R. Marom, R. Elazari, G. Salitra, D. Aurbach, *Energy Environ. Sci.* **2011**, *4*, 3243.

[3] S.-T. Myung, N. Takahashi, S. Komaba, C. S. Yoon, Y.-K. Sun, K. Amine, H. Yashiro, *Adv. Funct. Mater.* **2011**, *21*, 3231.

[4] V. Aravindan, N. Shubha, Y. L. Cheah, R. Prasanth, W. Chuiling, R. R. Prabhakar, S. Madhavi, *J. Mater. Chem. A* **2013**, *1*, 308.

[5] V. Aravindan, Y.-S. Lee, R. Yazami, S. Madhavi, *Mater. Today* **2015**, *18*, 345.

[6] M. Winter, R. J. Brodd, *Chem. Rev.* **2004**, *104*, 4245.

[7] K. Zhang, X. Han, Z. Hu, X. Zhang, Z. Tao, J. Chen, *Chem. Soc. Rev.* **2015**, *44*, 699.

[8] X. Ma, B. Kang, G. Ceder, *J. Electrochem. Soc.* **2010**, *157*, A925.

[9] N. Arun, V. Aravindan, S. Jayaraman, N. Shubha, W. C. Ling, S. Ramakrishna, S. Madhavi, *Nanoscale* **2014**, *6*, 8926.

[10] U. Boesenberg, M. Falk, C. G. Ryan, R. Kirkham, M. Menzel, J. Janek, M. Fröba, G. Falkenberg, U. E. A. Fittschen, *Chem. Mater.* **2015**, *27*, 2525.

[11] J.-H. Kim, N. P. W. Pieczonka, L. Yang, *ChemPhysChem* **2014**, *15*, 1940.

[12] M. Xu, L. Zhou, Y. Dong, Y. Chen, J. Demeaux, A. D. MacIntosh, A. Garsuch, B. L. Lucht, *Energy Environ. Sci.* **2016**, *9*, 1308.

[13] H. Sclar, O. Haik, T. Menachem, J. Grinblat, N. Leifer, A. Meitav, S. Luski, D. Aurbach, *J. Electrochem. Soc.* **2012**, *159*, A228.

[14] X. Hao, B. M. Bartlett, *J. Electrochem. Soc.* **2013**, *160*, A3162.

[15] J. Liu, A. Manthiram, *Chem. Mater.* **2009**, *21*, 1695.

[16] X.-W. Gao, Y.-F. Deng, D. Wexler, G.-H. Chen, S.-L. Chou, H.-K. Liu, Z.-C. Shi, J.-Z. Wang, *J. Mater. Chem. A* **2015**, *3*, 404.

[17] N. P. W. Pieczonka, V. Borgel, B. Ziv, N. Leifer, V. Dargel, D. Aurbach, J.-H. Kim, Z. Liu, X. Huang, S. A. Krachkovskiy, G. R. Goward, I. Halalay, B. R. Powell, A. Manthiram, *Adv. Energy Mater.* **2015**, *5*, 1501008.

[18] K. Xu, *Chem. Rev.* **2014**, *114*, 11503.

[19] H. Zhao, W. Yuan, G. Liu, *Nano Today* **2015**, *10*, 193.

[20] M. Ling, J. Qiu, S. Li, H. Zhao, G. Liu, S. Zhang, *J. Mater. Chem. A* **2013**, *1*, 11543.

[21] A. Magasinski, B. Zdyrko, I. Kovalenko, B. Hertzberg, R. Burtovyy, C. F. Huebner, T. F. Fuller, I. Luzinov, G. Yushin, *ACS Appl. Mater. Interfaces* **2010**, *2*, 3004.

[22] I. Kovalenko, B. Zdyrko, A. Magasinski, B. Hertzberg, Z. Milicev, R. Burtovyy, I. Luzinov, G. Yushin, *Science* **2011**, *334*, 75.

[23] E. Pohjalainen, S. Räsänen, M. Jokinen, K. Yliniemi, D. A. Worsley, J. Kuusivaara, J. Juurikivi, R. Ekqvist, T. Kallio, M. Karppinen, *J. Power Sources* **2013**, *226*, 134.

[24] M. H. Ryou, J. Kim, I. Lee, S. Kim, Y. K. Jeong, S. Hong, J. H. Ryu, T. S. Kim, J. K. Park, H. Lee, J. W. Choi, *Adv. Mater.* **2013**, *25*, 1571.

[25] M. Ling, Y. Xu, H. Zhao, X. Gu, J. Qiu, S. Li, M. Wu, X. Song, C. Yan, G. Liu, S. Zhang, *Nano Energy* **2015**, *12*, 178.

[26] B.-R. Lee, E.-S. Oh, *J. Phys. Chem. C* **2013**, *117*, 4404.

[27] J. Xu, S.-L. Chou, Q.-f. Gu, H.-K. Liu, S.-X. Dou, *J. Power Sources* **2013**, *225*, 172.

[28] S. Lee, E.-Y. Kim, H. Lee, E.-S. Oh, *J. Power Sources* **2014**, *269*, 418.

[29] J. Ming, H. Ming, W.-J. Kwak, C. Shin, J. Zheng, Y.-K. Sun, *Chem. Commun.* **2014**, *50*, 13307.

[30] Y.-Q. Zhang, *Biotechnol. Adv.* **2002**, *20*, 91.

[31] M. N. Padamwar, A. P. Pawar, *J. Sci & Ind Res.* **2004**, 63, 323.

[32] H. Wang, F. Meng, Y. Cai, L. Zheng, Y. Li, Y. Liu, Y. Jiang, X. Wang, X. Chen, *Adv. Mater.* **2013**, *25*, 5498.

# Chapter 7

# Conclusion and Future Work

*This chapter draws together the threads of each chapter and concludes about the thesis. Firstly, the implications and impacts of the research outcomes will be presented, followed by the discussion on the outcomes of each hypothesis. In particular, the extent to which the original hypothesis was proved and the design target is achieved will be discussed in detail. Then the reconnaissance work regarding the pseudocapacitance of* $TiO_2$ *(B) is briefly illustrated. Finally, outstanding questions and future research strategies towards the practical application of dual phase* $TiO_2$ *materials in electrochemical energy storage (EES) devices are presented.*

## 7.1 Implications and Impact of Findings

This thesis aims at improving the high rate performances of the $TiO_2$ materials towards practical application in high power, long life electrochemical energy storage (EES) devices. With the additive-free nanotube electrode as the platform, the lithiation-induced conductivity was systematically investigated with different integration extent of anatase into the $TiO_2$ (B) structure. The results show that dual phase $TiO_2$ nanotubes feature higher conductivity during the lithiation process and exhibit excellent high power performances than the single phase $TiO_2$ (B) counterpart. With this dual phase materials, we further fabricate high power, long life lithium-ion hybrid capacitors (LICs) via the pre-lithiation treatment, followed by the assembly of high energy lithium-ion batteries (LIBs) with the high voltage cathode passivated by the auxiliary sericin binder. These devices with full cell configuration further verify the excellent rate performances of the dual phase $TiO_2$ nanotubes and paves way for the practical adoption of such materials in real applications. The outcomes of each hypothesis are presented below.

### 7.1.1 Outcome of Hypothesis 1: Dual Phase $TiO_2$ Materials Feature High Rate Performances Compared to Pure Phase $TiO_2$ (B)

The high rate performances of $TiO_2$ (B) materials are mainly hindered by its poor electrical conductivity. It is proposed in Chapter 1 that by integration of anatase phase into the $TiO_2$ (B) structure, the electrical conductivity during the lithiation process will increase at very early stage before the main reaction of $TiO_2$ (B), thus achieving high rate performances. This hypothesis was systematically studied in Chapter 4. With the hydrogen titanate nanotubes as the precursor, $TiO_2$ nanotubes with different phase contents were successfully synthesized by different annealing temperature. Utilizing the additive-free $TiO_2$ nanotubes as the platform, the *in situ* electrochemical impedance spectroscopy (EIS) was performed during the discharging process (lithiation). The results show that lithiation-induced conductivity gradually increases in $TiO_2$ (B), while in anatase phase, such conductivity increases at very early stage of reaction and then decreases after the two phase lithiation owing to the structural changes. Dual phase materials combine the advantages of both and exhibits high conductivity at early stage of lithiation and maintain it during subsequent reaction which has pronounced effect on the improvement of conductivity. As result, dual phase nanotubes delivers feature superior rate performances: a capacity of 112.1 mAh $g^{-1}$ can be delivered at 24 A $g^{-1}$ (~72 C), and even higher capacity of 131.1 mAh $g^{-1}$ can be achieved after 10,000 cycles at 30 C. while for the pure phase $TiO_2$ (B), only 25.1 mAh $g^{-1}$ and 13.7 mAh $g^{-1}$ and delivered at 30 C and 24 A $g^{-1}$, respectively.

The original hypothesis that high lithiation-induced conductivity can be achieved by integration of anatase phase in $TiO_2$ (B) to achieve high rate performances in dual phase $TiO_2$ is proven to be true.

### 7.1.2 Outcome of Hypothesis 2: Pre-lithiation Process Can Improve the Performances of $TiO_2$ Nanotubes for High Power LIC

The successful integration of $TiO_2$ materials in full cell EES devices requires not only high conductivity but also high Columbic efficiency. Therefore it is hypothesized in Chapter 1 that the pre-lithiation process in $TiO_2$ materials can improve both factors. This hypothesis is studied in Chapter 5, where the electrochemical process is used to achieve different degree of lithiation at pre-determined voltage. It is found that early lithiation increases the conductivity and Columbic efficiency effectively and the resultant LICs demonstrates high power densities with high energy. For the optimized sample with pre-lithiation voltage of 1.76 V, high energy density of 50.8 Wh $kg^{-1}$ can be achieved at power density of 493 W $kg^{-1}$ and high power density of 8.98 kW $kg^{-1}$ is delivered at energy density of 20.7 Wh $kg^{-1}$, which is much better than the pristine $TiO_2$ materials (10.9 Wh $kg^{-}$1@ 4.55 kW $kg^{-1}$). Furthermore, such lithiation process also improves the cycling behavior of the $TiO_2$ materials; the full cell LIC with pre-lithiated $TiO_2$ could maintain more than 70 % of original capacity after 10,000 cycles, whereas for pristine $TiO_2$ electrode, the capacity fades to 70% within 100 cycles.

The original hypothesis that pre-lithiation process can improve the performances of $TiO_2$ nanotubes for high power and high energy LICs is proven to be true.

### 7.1.3 Outcome of hypothesis 3: It is Plausible to Fabricate High Energy LIB Based on $TiO_2$ Anode and High Voltage Cathode Formulated by Water Soluble Sericin Binder

Although dual phase $TiO_2$ materials feature fast charging capability and long cycle life, the lithiation voltage is relatively high (1.4-1.8 V), resulting in low energy density of the full cell. One effective approach to increase the energy density is to increase the operating voltage of batter cells as energy is proportional to both capacity and voltage. In such regards, spinel $LiNi_{0.5}Mn_{1.5}O_4$ (LNMO) with high lithiation voltage (~ 4.75 V) is promising cathode. However, the operating voltage falls out of the stability window of conventional electrolytes based on $LiPF_6$ in alkyl carbonate solvents. It was proposed in chapter 1 that the auxiliary water-soluble sericin binder will help to build up stable passivation layer and improve the high rate performances in LNMO. This hypothesis is tested in Chapter 6 where the cathode LNMO was formulated by sericin binder. The electrode with sericin binder delivers both high capacity and high rate capacity: at rate of 1 C and 5 C, a capacity of 105.8 and 91.2 mAh $g^{-1}$ is delivered for sericin binder, compared to 90.2 and 28.1 mAh $g^{-1}$ for PVDF binder. EIS and surface morphology study indicates that a stable passivation film is formed with the sericin binder, and the passivation is stable after 100 cycles. As such, the full cell based on $TiO_2$ could deliver high energy density of 687.6 Wh $kg^{-1}$ (based on $TiO_2$ mass) at power density of 957.6 W $kg^{-1}$, and high power density of 18.26 Wh $kg^{-1}$ at 233.4 Wh $kg^{-1}$. In addition, such full cell could deliver a capacity of 100.6 mAh $g^{-1}$ after 1,000 cycles at high rate of 10 C, further proves the long term stability of $TiO_2$ materials and sericin binder.

The above results show that high energy LIB based on $TiO_2$ anode and high voltage cathode passivated by water soluble sericin binder could be achieved. The original hypothesis is proven to be true.

## 7.2 Reconnaissance Work of Intercalation Pseudocapacitance in $TiO_2$ (B)

The excellent rate performances of $TiO_2$ (B) are resulting from its open structure with pseudocapacitive diffusion behavior, where the rate is not limited by the diffusion of lithium-ions inside the crystal structure. The pseudocapacitive charge storage behavior in $TiO_2$ (B) was first studied by Zukalova and co-workers,[1] by cyclic voltammetry (CV) test of the $TiO_2$ (B) electrode at different rate sweep rates, they discovered that the peak current density is directly proportional to the sweep rates and concluded that insertion of lithium into the $TiO_2$ (B) phase is not subjected to diffusion controlled mechanism, instead, a facile capacitive behavior is dominant. Later, based on the extensive study on mesoporous T-$Nb_2O_5$ materials, Bruce Dunn first proposed the concept of intercalation pseudocapacitance[2, 3] with the following distinctive characteristics: first of all, no phase separation occurs for the reaction and both anodic and cathodic peaks should be broad; second, the peak separation should be small, where no obvious peak separation shall be observed at low scan rate. Third, peak current is proportional to the sweep rate, similar to that of supercapacitors. Fourth, the capacity should not vary much with current rate. From the above guidelines, they later clarify that $TiO_2$ (B) belongs to intrinsic intercalation pseudocapacitors, i.e., even the bulk form of $TiO_2$ (B) exhibits pseudocapacitive properties with ultrafast charging capability.[4] However, the rate capability of $TiO_2$ (B) at time scale within 1 minute (> 60 C) requires further optimization of the electrode system to meet the basic requirement for pseudocapacitor metrics: a specific capacitance larger than 300 F $g^{-1}$ need to be achieved at high rate of 60 C with mass loading at least 1 mg $cm^{-2}$. The specific capacitance ($C$) is given by:

$$C = Q / V \tag{7.1}$$

Where $Q$ is the specific capacity and $V$ is the voltage range. Since the unit for specific capacity is usually mAh $g^{-1}$, therefore a factor of 3.6 is required to convert to Columb. Based on such calculation, a specific capacitance of 300 F $g^{-1}$ corresponds to a specific capacity of 125 mAh $g^{-1}$ with voltage window of 1.0-2.5 V.

For $TiO_2$ (B) to achieve such pseudocapacitive charge storage properties, the electrical conductivity of the $TiO_2$ (B) should be improved to reduce the polarization effect and maximize the delivered capacities.[5] In previous study, we have identified that the prominent function of anatase phase integrated in $TiO_2$ (B) structure is to enhance the electrical conductivity and reduce polarization of the electrode. To further increases the electrical conductivity and improve the high rate performances, the highly conductive single wall CNT (373 S cm$^{-1}$) is added to the dual phase $TiO_2$ electrode. The weight percentage of CNT is 10 wt% and the loading density is around 1 mg cm$^{-2}$. As shown in Figure 7.1, at high rate of 60 C, a stable capacity of 125 mAh g$^{-1}$ could be delivered for 1,000 cycles. Such excellent rate performances verify that $TiO_2$ (B) complies with the pseudocapacitor performance metrics and is a very promising candidate for ultrafast ion storage.

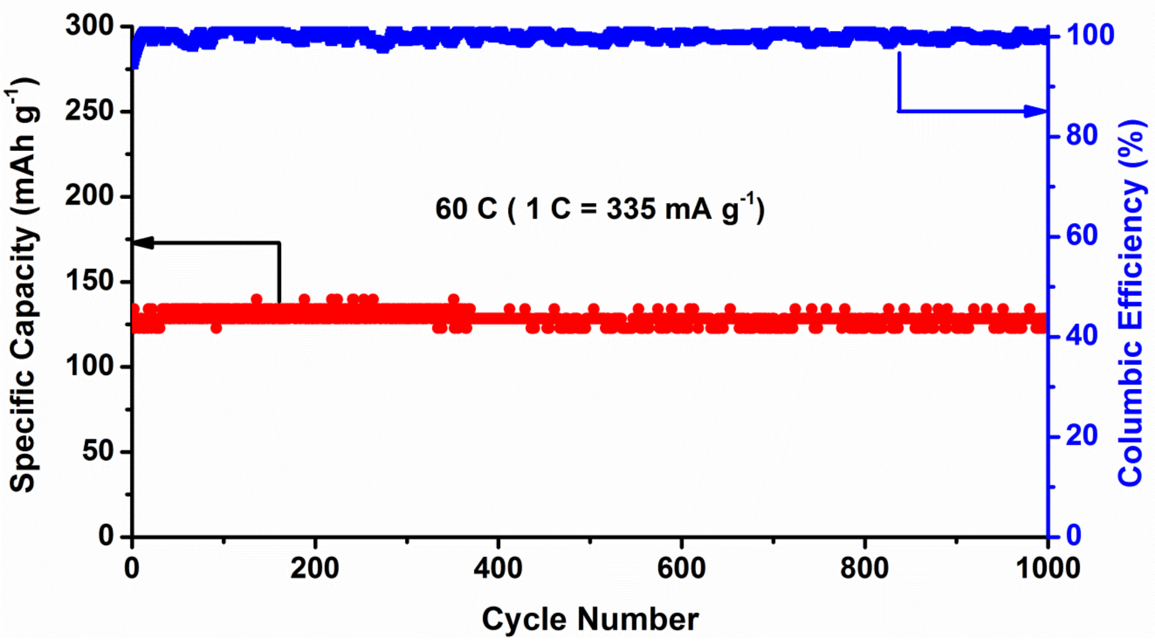

**Figure 7.1** Long-term cycling performances of the dual phase $TiO_2$ electrode with 10 wt% CNT as conductive additives at a rate of 60 C.

## 7.3 Outstanding Questions

This dissertation aims at improving the high rate performances of the $TiO_2$ based electrode in both high power, lone life LICs and high energy LIBs. Excellent performances at high current rates have been achieved by integrating anatase phase with $TiO_2$ (B) nanotubes. However, the specific capacity of the dual phase materials is still limited, even at low rate of 0.2 A g$^{-1}$, a capacity of only 250 mAh g$^{-1}$ is delivered, which is below the value of graphite (350-370 mAh g$^{-1}$). Thus, improving the specific capacity of $TiO_2$-based electrode is important to achieve high energy LIB and LIC cells. In addition, for the pre-lithiation process, metallic lithium is used in current study, which requires inert environment and possess safety hazard due to the reactivity of lithium metal.

Optimization of the lithiation method is another problem to tackle for the commercial adoption of the $TiO_2$ materials for high power LIC. Approaches to address these problems will be proposed in the section below.

### 7.3.1 Improving the Specific Capacity of $TiO_2$ Materials

The $TiO_2$ nanotubes are synthesized from the hydrogen titanate precursors, a layered structured material with interlayer spacing around 0.7-0.8 nm, where the cation between the space regions could be substituted easily.[6] This unique cation exchange property enables the fabrication of a variety of composite materials to further improve the overall capacity and energy density of the batteries based on $TiO_2$ materials.

Recent studies have shown that metallic silver can react reversibly with lithium; a high capacity of 1158 mAh $g^{-1}$ during first discharge has been achieved.[7, 8] Therefore the addition of silver can potentially improve the capacity of $TiO_2$. In addition, the electrical conductivity of silver is highest among all metals; therefore the decoration of silver is expected to enhance the overall conductivity and interfacial charge transport efficiency of $TiO_2$. The silver decorated $TiO_2$ material is synthesized via ion exchange followed by post annealing. Briefly, the hydrogen titanate solution is immersed in $AgNO_3$ (0.1 M) solution for 24 h for complete of ion exchange. Then the material is subjected to thermal treatment at 400 ℃ to convert the silver ions to metallic silver. Figure 7.2 below shows the preliminary results for the integration of silver nanoparticles in the $TiO_2$ structure: SEM images clearly demonstrate the precipitation of the silver nanoparticles. Element mapping was carried out to investigate the distribution of silver nanoparticles in the $TiO_2$ nanotube structure; the silver nanoparticles are spatially dispersed onto the nanotube network with no significant aggregation. Further element analysis indicates that the mass loading of silver is around 24 wt%.

To evaluate the electrochemical properties of the Ag-$TiO_2$ composite, cyclic voltammetry (CV) test at scan rate of 0.05 mV $s^{-1}$ were performed first. As shown in Figure 7.2c, the composites contain mainly $TiO_2$ (B) phase, as manifested by two prominent reduction peaks around 1.5 V. A small quantity of anatase phase is present evidenced from the peak pair of 1.75/1.9 V. Additional reduction peaks (below 1.0 V) are observed at 0.04 and

0.02 V, corresponding to the alloying reaction of silver with lithium.[8] During the charging process, the oxidation peaks appears at 0.1 V and 0.3 V, which matches well with the de-alloying reaction of silver lithium alloys. Such peaks remain obvious after five cycles, indicating the good reversibility of the alloying/de-alloying reaction of silver nanoparticles. The battery performances are shown in Figure 7.2d, at voltage window of 0.01-3 V, a capacity of 315 mAh $g^{-1}$ is achieved with Ag-$TiO_2$ electrode, which is 20 % higher than that of pure $TiO_2$ electrode (269 mAh $g^{-1}$). In the discharge voltage profile, the long flat tail region at low potential corresponds to the alloying reaction with lithium, while the two small plateaus present in the charging profile is also in agreement with the peaks in CV curves. It is therefore concluded that the alloying reaction of silver with lithium is accountable for the improved capacity.

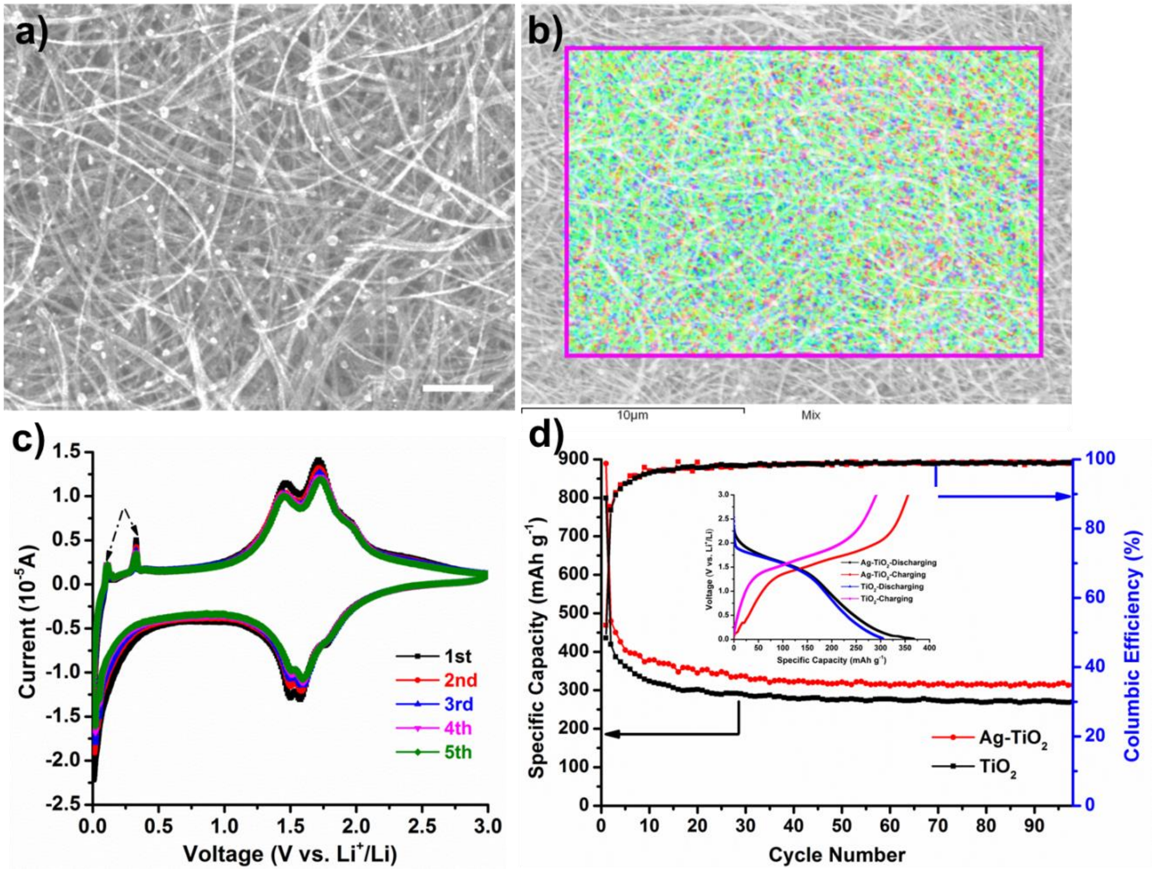

**Figure 7.2** (a) SEM image of Ag-$TiO_2$. Scale bar is 1 μm; b) Element mapping of Ag-$TiO_2$ composite, Ag, Ti and O element is represented with blue, green and red color, respectively; c) CV scan of Ag-$TiO_2$ electrode at rate of 0.05 mV $s^{-1}$; d) battery performances of Ag-$TiO_2$ and pure $TiO_2$ electrode at current rate of 0.1 A $g^{-1}$. Inset shows typical charge/discharge curve.

The alloying reaction of silver with lithium occurs in voltage window below 1.0 V, which is not compatible with the main reaction window of $TiO_2$ materials (1-3 V). Many transition metal sulfides are active towards lithium storage in similar voltage window as $TiO_2$ with higher theoretical capacity.[9, 10] For example, Goodenough has shown that the capacity of ion sulfides (FeS) can reach 600 mAh $g^{-1}$ in range of 1-2.5 V with a voltage plateau around 1.33 V.[9] Similarly, a capacity of 550 and 580 mAh $g^{-1}$ could be delivered by $Co_{1-x}S$ and NiS with voltage plateau of 1.40 V and 1.47 V,[11] respectively. These voltages are quite similar to that of the $TiO_2$, which could be utilized to improve its specific capacity. However, the cyclability of transition metal sulfide is poor with microparticles. By using $TiO_2$ nanotubes as the backbone followed by ion exchange and heat treatment, nanosized transition metal sulfides can be grown onto the $TiO_2$ nanotube surface to improve specific capacity without sacrificing the long term cyclability. For example, to prepare nanosized FeS/$TiO_2$ composites, after ion exchange with the solution contains $Fe^{2+}$, the sample can subjected to $H_2S$ gaseous environment followed by thermal annealing. By carefully control the process, the optimized structure can be fabricated.

### 7.3.2 Chemical Lithiation of $TiO_2$ Materials

In chapter 5, the pre-lithiation of $TiO_2$ nanotubes is achieved by electrochemical method with metallic lithium as the counter electrodes. In fact, the lithiation reaction of $TiO_2$ occurs at high voltage window of 1-3 V, therefore the pre-lithiation process can be achieved by treatment with materials whose lithiation window is lower than that of $TiO_2$. For example, the n-butyllithium has a reaction potential of 1.0 V versus lithium, therefore by mixing it with $TiO_2$ structures, spontaneous chemical reaction will occur to lithiated the $TiO_2$ materials.[12] In fact, Wagemaker et al. demonstrated chemical lithiation of anatase by subjecting the powder to n-butyllithium (1.6 M in hexane) with stirring.[13-15] The reaction is vigorous and the white anatase powder quickly transformed into blue color indicating successful lithium intercalation. Apart from n-butyllithium, other organic lithium sources can also be used for the chemical lithiation process. For instance, lithium ethoxide ($C_2H_5OLi$)[16] was used to treat $TiO_2$ (B) nanotubes which could improve the first cycle Columbic efficiency and reduce the irreversible capacity loss. In addition, recently Michael Graetzel demonstrated lithium doping of anatase $TiO_2$ with lithium bis (trifluoromethane sulfonyl) imide (LiTFSI) as the lithium source followed by heat treatment.[17] These results indicate that dual phase $TiO_2$ nanotubes could be chemically lithiated by organic lithium compounds in large quantities for the large-scale fabrication of commercial LIC cells.

Apart from the organic lithium compounds, inorganic lithium hydroxide (LiOH) also serves as another promising candidate for the chemical lithiation of $TiO_2$ materials. Previous study shows that by blending LiOH with conductive carbon additives, it will react with lithium reversibly between 0.05-0.8 V,[18] such voltage window is much smaller than that of the $TiO_2$, therefore, it could be used potentially to lithiated $TiO_2$ materials. Martin et. al studied the effect of LiOH treatment on anatase particles and found that such treatment could improve the first cycle Columbic efficiency from 77% to around 90%,[19] while still maintaining the cycling stability. It is expected that LiOH could also be used to treat dual phase $TiO_2$ nanotubes to migrate the irreversible capacity loss and improve the Columbic efficiency.

The current thesis shows the superiority of dual phase $TiO_2$ nanotubes as promising material candidates for fast charging EES devices with ultralong cycle life. These pre-lithiation approaches will further fasten the commercialization process of dual phase $TiO_2$-based materials. In fact, large size pouch cells and 18650 cells with capacity more than 1 Ah have been fabricated in our group to verify the scale-up performances. It is anticipated that EES devices based on dual phase $TiO_2$ materials that charge faster, last longer and work safer will transform the community towards sustainable electricity generation and smart energy distribution.

## References

[1] M. Zukalová, M. Kalbáč, L. Kavan, I. Exnar, M. Graetzel, *Chem. Mater.* **2005**, *17*, 1248.

[2] V. Augustyn, J. Come, M. A. Lowe, J. W. Kim, P.-L. Taberna, S. H. Tolbert, H. D. Abruña, P. Simon, B. Dunn, *Nat Mater* **2013**, *12*, 518.

[3] J. C. Aguirre, A. Ferreira, H. Ding, S. A. Jenekhe, N. Kopidakis, M. Asta, L. Pilon, Y. Rubin, S. H. Tolbert, B. J. Schwartz, B. Dunn, V. Ozolins, *J. Phys. Chem. C* **2014**, *118*, 19505.

[4] V. Augustyn, P. Simon, B. Dunn, *Energy Environ. Sci.* **2014**, *7*, 1597.

[5] C. Chen, Y. Wen, X. Hu, X. Ji, M. Yan, L. Mai, P. Hu, B. Shan, Y. Huang, *Nat. Commun.* **2015**, *6*, 6629.

[6] D. V. Bavykin, J. M. Friedrich, F. C. Walsh, *Adv. Mater.* **2006**, *18*, 2807.

[7] B.-L. He, B. Dong, H.-L. Li, *Electrochem. Commun.* **2007**, *9*, 425.

[8] C.-M. Park, H. Jung, H.-J. Sohn, *Electrochem. Solid-State Lett.* **2009**, *12*, A171.

[9] Y. Kim, J. B. Goodenough, *J. Phys. Chem. C* **2008**, *112*, 15060.

[10] X. Xu, W. Liu, Y. Kim, J. Cho, *Nano Today* **2014**, *9*, 604.

[11] S.-C. Han, H.-S. Kim, M.-S. Song, P. S. Lee, J.-Y. Lee, H.-J. Ahn, *J. Alloys Compd.* **2003**, *349*, 290.

[12] M. S. Whittingham, M. B. Dines, *J. Electrochem. Soc.* **1977**, *124*, 1387.

[13] M. Wagemaker, R. van de Krol, A. P. M. Kentgens, A. A. van Well, F. M. Mulder, *J. Am. Chem. Soc.* **2001**, *123*, 11454.

[14] C. Jiang, M. Wei, Z. Qi, T. Kudo, I. Honma, H. Zhou, *J. Power Sources* **2007**, *166*, 239.

[15] M. Wagemaker, W. J. H. Borghols, F. M. Mulder, *J. Am. Chem. Soc.* **2007**, *129*, 4323.

[16] S. Brutti, V. Gentili, H. Menard, B. Scrosati, P. G. Bruce, *Adv. Energy Mater.* **2012**, *2*, 322.

[17] F. Giordano, A. Abate, J. P. Correa Baena, M. Saliba, T. Matsui, S. H. Im, S. M. Zakeeruddin, M. K. Nazeeruddin, A. Hagfeldt, M. Graetzel, *Nat Commun* **2016**, *7*, 10379.

[18] Y.-Y. Hu, Z. Liu, K.-W. Nam, O. J. Borkiewicz, J. Cheng, X. Hua, M. T. Dunstan, X. Yu, K. M. Wiaderek, L.-S. Du, K. W. Chapman, P. J. Chupas, X.-Q. Yang, C. P. Grey, *Nat Mater* **2013**, *12*, 1130.

[19] M. Søndergaard, Y. Shen, A. Mamakhel, M. Marinaro, M. Wohlfahrt-Mehrens, K. Wonsyld, S. Dahl, B. B. Iversen, *Chem. Mater.* **2015**, *27*, 119.